Adam Mickiewicz University in Poznań

Faculty of Physics and Astronomy

STRUCTURAL AND OPTICAL STUDIES OF LOW-DIMENSIONAL PEROVSKITE MATERIALS UNDER HIGH PRESSURE

Ph.D. thesis prepared in

Department of Experimental Physics of Condensed Phase,
Institute of Physics

Author:

Viktoriia Drushliak, M.Sc.

Thesis Supervisor:

Prof. dr hab. Marek Szafrański

Poznań, 2025

A mind that is stretched by a new experience can never go back to its old dimensions.

Oliver Wendell Holmes, Jr.

I want to express my deepest gratitude to the many individuals who supported me throughout my PhD journey. My time at the University of Adam Mickiewicz in Poznan has been one of immense personal and professional growth, and this would not have been possible without their help.

First and foremost, I am profoundly grateful to my supervisor, ***Prof. dr hab. Marek Szafrański****. Your demanding and rigorous approach pushed me to become a more resilient and self-dependent researcher. The high standards you set for scientific writing and presentations taught me the value of rigor and excellence. Your respect for my work and personal decisions, along with your unwavering support during the full-scale war in Ukraine, were invaluable. I will always appreciate the opportunities you provided for me to attend scientific conferences and publish in peer-reviewed journals, which were pivotal moments in my career.*

I am also deeply thankful for the personal support I received. My boyfriend, ***Yaroslav Harkavyi****, and best friend,* ***Bassam Jameel Mufeed****, were a constant source of emotional support. Our lunch breaks together provided a vital space for encouragement and resilience during the most challenging times. My gratitude also goes to my colleague,* ***Darko Stojkovsky****, for his support throughout my studies. I am also indebted to* ***my family*** *for their unwavering emotional support, even as they faced their own hardships.*

Finally, I want to acknowledge ***myself*** *for not giving up during these challenging times. This dissertation is a testament to my strong will and determination.*

This research was made possible by the financial support of the Polish National Science Centre,
Grant Opus 16 No. 2018/31/B/ST3/02188.

Contents

Abstract

Metal halide perovskites have rapidly advanced over the past decade, with diverse compositions, dimensionalities, and morphologies enabling high-performance photovoltaic and optoelectronic applications. Despite the progress, challenges concerning their stability and the precise understanding of structure–property relationships persist. High-pressure research, using techniques such as diamond anvil cells (DACs) combined with single-crystal X-ray diffraction (SCXRD) and complementary optical methods, provides a powerful means to investigate these relationships by changing interatomic interactions without chemical modification.

This thesis focuses on core findings from three publications, in particular, on the structural and optical responses of selected low-dimensional perovskites under variable pressure and temperature conditions. External stimuli such as pressure and temperature induce octahedral distortions, phase transitions, and electronic band structure modifications, thereby directly influencing optical behaviour. Pressure can even activate or enhance photoluminescence in materials that are weakly emissive under ambient conditions. Four materials were examined: two-dimensional (2D) perovskite-like $CsPb_2Br_5$, zero-dimensional (0D) Cs_4PbBr_6, and 2D layered guanidinium lead iodides, $[C(NH_2)_3]_2PbI_4$ and $CsC(NH_2)_3PbI_4$.

For $CsPb_2Br_5$, the layered framework remains stable up to at least 6 GPa. Its ultraviolet absorption edge at approximately 350 nm continuously red-shifts with increasing pressure, which corresponds to a narrowing of the band gap. This work also clarifies that previously reported visible-range photoluminescence and absorption are not intrinsic properties of the pure material but rather originate from the presence of three-dimensional (3D) $CsPbBr_3$ impurities, underscoring the critical importance of sample purity. In the study on Cs_4PbBr_6, a sequence of two first-order pressure-induced phase transitions at 2.6 and 3.2 GPa was revealed. These phase transitions drive a jumpwise band-gap reduction. A unique pseudo-Jahn–Teller distortion leads to an anomalous expansion of $PbBr_6$ octahedra in the tetragonal phase, directly responsible for pressure-induced broad band white-light emission. In guanidinium-based 2D perovskites, both compression and heating narrow the bandgap, through Pb–I bond contraction and Pb–I–Pb angle straightening. A highly anisotropic mechanical response is observed, with the direction perpendicular to the inorganic layers being surprisingly stiffer than the in-plane directions. Furthermore, a rare phenomenon of negative linear compressibility along one axis is identified in the high-pressure phase of $CsC(NH_2)_3PbI_4$, attributed to the suppression of iodine atom vibrations.

Streszczenie

Halogenkowe perowskity metaliczne w ostatniej dekadzie uległy szybkiemu rozwojowi, a ich zróżnicowane składy, wymiarowość i morfologie umożliwiły zastosowania w wysokowydajnych urządzeniach fotowoltaicznych i optoelektronicznych. Pomimo tego postępu nadal istnieją wyzwania związane z ich stabilnością oraz dokładnym zrozumieniem zależności pomiędzy strukturą a właściwościami. Badania wysokociśnieniowe, wykorzystujące techniki takie jak komórki diamentowe (DAC) w połączeniu z dyfrakcją rentgenowską na pojedynczych kryształach (SCXRD) oraz uzupełniającymi metodami optycznymi, stanowią potężne narzędzie do badania tych zależności poprzez zmianę oddziaływań międzyatomowych bez modyfikacji chemicznej.

Niniejsza rozprawa koncentruje się na kluczowych wynikach trzech publikacji, w szczególności na strukturalnych i optycznych odpowiedziach wybranych niskowymiarowych perowskitów pod zmiennym ciśnieniem i temperaturą. Czynniki zewnętrzne, takie jak ciśnienie i temperatura, wywołują deformacje oktaedrów, przejścia fazowe oraz modyfikacje struktury pasm elektronowych, a tym samym bezpośrednio wpływają na zachowanie optyczne. Ciśnienie może nawet aktywować lub wzmacniać fotoluminescencję w materiałach, które w warunkach otoczenia wykazują słabą emisję. Zbadano cztery materiały: dwuwymiarowy (2D) perowskitopodobny $CsPb_2Br_5$, zerowymiarowy (0D) Cs_4PbBr_6 oraz 2D warstwowe perowskity guanidyniowe $[C(NH_2)_3]_2PbI_4$ i $CsC(NH_2)_3PbI_4$.

W przypadku $CsPb_2Br_5$ wykazano, że warstwowy szkielet pozostaje stabilny co najmniej do 6 GPa. Jego krawędź absorpcji w ultrafiolecie, zlokalizowana przy około 350 nm, ulega ciągłemu przesunięciu w stronę dłuższych fal wraz ze wzrostem ciśnienia, co odpowiada zwężaniu przerwy energetycznej. Praca ta wykazała również, że wcześniej raportowana fotoluminescencja i absorpcja w zakresie widzialnym nie są właściwościami intrinsicznymi czystego materiału, lecz pochodzą z obecności domieszek trójwymiarowego $CsPbBr_3$, co podkreśla kluczowe znaczenie czystości próbki. W badaniu nad Cs_4PbBr_6 ujawniono sekwencję dwóch pierwszorzędowych przejść fazowych indukowanych ciśnieniem przy 2.6 i 3.2 GPa. Przejściom tym towarzyszy skokowe zmniejszenie przerwy energetycznej. Unikalne zniekształcenie typu pseudo-Jahna–Tellera prowadzi do anormalnej ekspansji oktaedrów $PbBr_6$ w fazie tetragonalnej, co bezpośrednio odpowiada za ciśnieniowo indukowaną szerokopasmową emisję białego światła. W perowskitach guanidyniowych 2D zarówno kompresja, jak i ogrzewanie powodują zawężenie przerwy energetycznej, wynikające ze skracania wiązań Pb–I oraz prostowania kątów Pb–I–Pb. Zaobserwowano wysoce anizotropową odpowiedź mechaniczną, przy czym kierunek prostopadły do warstw nieorganicznych jest zaskakująco sztywniejszy niż kierunki w płaszczyźnie. Ponadto w fazie wysokociśnieniowej $CsC(NH_2)_3PbI_4$ zidentyfikowano rzadkie zjawisko ujemnej kompresji liniowej wzdłuż jednej osi, przypisane tłumieniu drgań atomów jodu.

List of publications

The thesis is based on the three following research articles:

1. *Thermodynamic stability, structure, and optical properties of perovskite-related $CsPb_2Br_5$ single crystals under pressure*
   Viktoriia Drushliak, Marek Szafrański
   Inorg. Chem., **2022** *61* (36), 14389-14396 (Open Access)
   https://doi.org/10.1021/acs.inorgchem.2c02253

2. *White-light emission triggered by pseudo Jahn–Teller distortion at the pressure-induced phase transition in Cs_4PbBr_6*
   Viktoriia Drushliak, Konrad J. Kapcia, Marek Szafrański
   J. Mater. Chem. C, **2024**, 12, 4360-4368
   https://doi.org/10.1039/D4TC00036F

3. *Effect of pressure and temperature on the structure and optical properties of two-dimensional lead iodide perovskites*
   Viktoriia Drushliak, Marek Szafrański
   Chem. Commun., **2025**, 61, 8019-8022
   https://doi.org/10.1039/D5CC01232E

I. Introduction

1. Metal-halide perovskite materials

1.1 General properties

Metal-halide perovskites refer to a broad class of materials with the general formula ABX_3, where A represents a larger monovalent inorganic or organic cation (e.g., Cs^+, $C(NH_2)_3$ (G), $CH_3NH_3^+$ (MA), $HC(NH_2)_2^+$ (FA)), B is a smaller divalent metal cation (e.g., Pb^{2+}, Sn^{2+}, Mn^{2+}), and X is a halide anion (Br^-, I^-, Cl^-). While oxide perovskites have been studied for decades for their ferroelectric and relaxor properties, halide perovskites have only recently gained popularity due to their excellent electronic and optical properties, along with their easy and low-cost fabrication [1–7]. Kojima and co-workers first demonstrated in 2009 that $MAPbI_3$ could serve as an efficient light absorber in a solar cell (yielding ~3.8% power conversion efficiency) [8]. Since then, interest in perovskites has grown exponentially due to their potential applications in optoelectronics, photovoltaics, and quantum materials field [9–20].

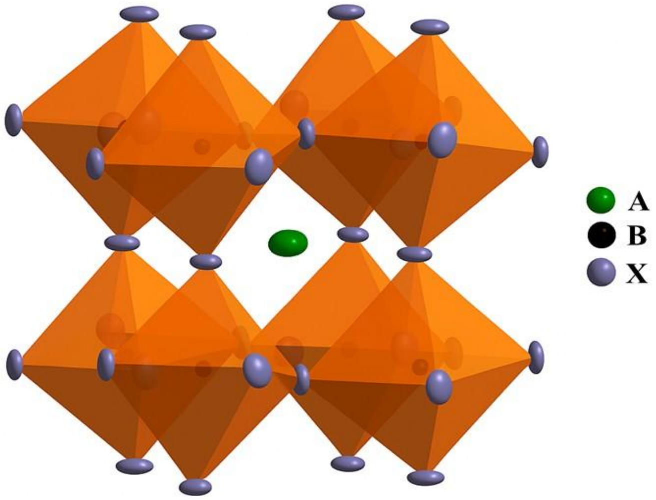

Figure 1. Crystal structure of classical perovskite with ABX_3 formula.

In the classical perovskite structure (see example in Figure 1), the main characteristic is the corner-sharing network of BX_6 octahedra. The B-site cations are surrounded by six X-site anions positioned at the corners of an octahedron. Each anion is shared by two neighboring octahedra, connecting them to form a continuous three-dimensional framework. This connectivity is essential as it directly influences critical material properties such as light absorption efficiency, charge carrier transport dynamics within the crystal lattice, and the responsiveness to external environmental conditions. The A-site cations occupy the voids formed between the interconnected BX_6 octahedra. The geometric relationship between the A, B, and X ions dictates the overall symmetry and tolerance of the structure. The most common crystal structures are cubic, tetragonal, or orthorhombic, depending on composition and thermodynamic conditions.

Structural stability in perovskites is influenced by numerous variables, including temperature, pressure, the size of the A-site cation, and the presence of crystal lattice defects. A widely employed method for predicting the structural stability is the Goldschmidt tolerance factor (t), calculated using the ionic radii (r) of the A, B, and X ions:

$$t = \frac{r_A + r_X}{\sqrt{2}(r_B + r_X)} \,. \tag{1}$$

The material is likely to form a stable cubic perovskite structure if t is between 0.9 and 1.0. Deviations from this range, specifically t values between 0.71 and 0.9, typically result in structural distortions, often characterized by tilted octahedra and the formation of lower-symmetry phases such as tetragonal or orthorhombic [21]. If the tolerance factor lies outside this range, either too high or too low, the material tends to form non-perovskite phases.

In perovskite materials, distortions of the BX_6 octahedral network are common and often crucial to determining the structure and physical properties of the material. One of the most common distortion mechanisms is octahedral tilting, which occurs when stiff BX_6 units rotate slightly to compensate size differences among ions or relieve external stresses [22]. Another is lattice strain, which is the stretching or compression of the crystal lattice in reaction to applied external forces. A particularly significant distortion mechanism, especially in perovskites containing transition metal ions at the B-site, is the Jahn–Teller effect. This phenomenon arises when a crystal structure possesses a symmetric atomic arrangement but an electronically degenerate ground state, meaning electrons can occupy multiple orbitals of the same energy. According to the Jahn–Teller theorem, such a configuration is unstable and the system will distort in order to remove electronic degeneracy [23]. The d-electron energy levels of an ideal octahedron are divided into two groups: an upper doubly degenerate pair (e_g) and a lower triply degenerate pair (t_{2g}) (see Figure 2). Transition metal ions with an odd number of electrons in the upper pair of orbitals, like Mn^{3+} (d^4, t_{2g}^3, e_g^1), Cu^{2+} (d^9, t_{2g}^6, e_g^3), and Ni^{3+} (d^7, t_{2g}^6, e_g^1), have a degenerate ground state due to two possible choices of electron configurations. To resolve this instability, the octahedron distorts, often by elongating or compressing along one of its axes, leading to altered B–X bond lengths (e.g., four shorter and two longer bonds or vice versa). The distortion splits the energy levels of the degenerate orbitals, stabilizing the electronic configuration and breaking the original symmetry, often reducing it from cubic to tetragonal or orthorhombic. Closely related is the pseudo-Jahn–Teller effect, which can occur even when the ground state of the system is not degenerate. In this scenario, distortion results from the mixing of the ground state with an excited electronic state that lies close in energy. This interaction can destabilize the symmetric configuration and again lead to a reduction in symmetry through structural distortion. While the classical Jahn–Teller effect is mostly associated with certain *d*-electron configurations, the pseudo-Jahn–Teller effect is more broadly applicable and is especially relevant in systems with soft lattices and strong electron-phonon coupling, characteristics commonly found in hybrid perovskites. Understanding these distortion mechanisms is therefore essential for designing perovskite-based devices for applications in photovoltaics, light emission and sensor technologies.

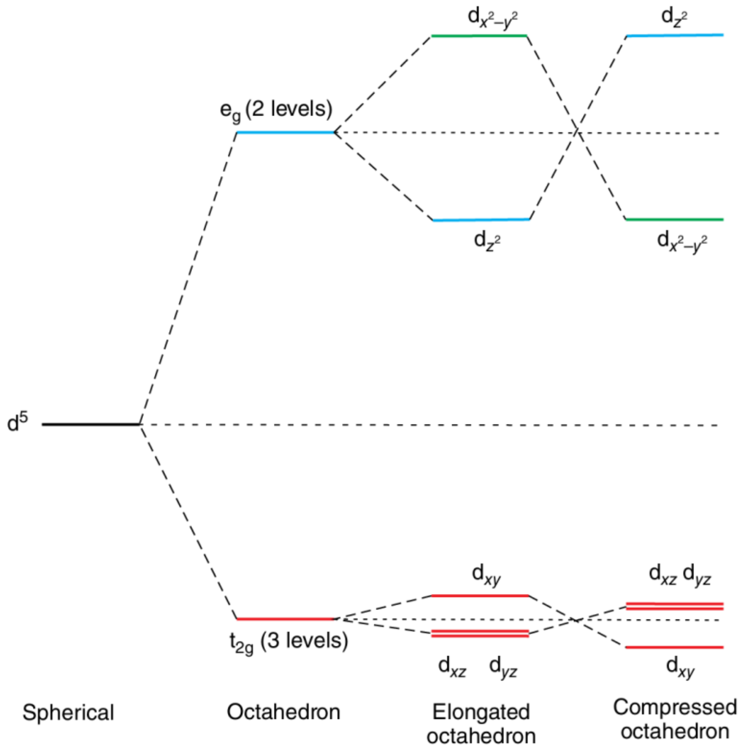

Figure 2. Jahn–Teller distortion effects on the *d*-electron energy levels of a B-site cation [23].

Another important aspect of distortion mechanisms in perovskites involves phase transitions induced by external conditions such as pressure and temperature. These stimuli can have a profound effect on the crystal structure by modifying the arrangement and connectivity of the BX_6 octahedra, frequently leading to symmetry breaking and significant changes in the physical properties of the material. When pressure is applied, the atoms are forced closer together, triggering structural rearrangements. This can involve changes in the tilting angles of the octahedra, a reduction in lattice volume, or even a complete reconstruction of the crystal structure. Such pressure-induced distortions can lead to phase transitions from a high-symmetry to a low-symmetry structure (or vice versa), often accompanied by notable changes in optical and electronic parameters, such as bandgap narrowing or widening, modification of charge-carrier mobility, or luminescence activation. Hybrid halide perovskites, with their soft lattices and ionic nature, are particularly sensitive to pressure, allowing for a wide range of tunable optical responses [24–26].

Temperature can similarly cause phase transitions in perovskite materials. Thermal vibrations and entropy contributions become more significant with increasing temperature, which often leads to more symmetric phases. Many perovskites exhibit phase transitions upon heating, for example, transforming from low-temperature orthorhombic or tetragonal structures to a high-temperature cubic phase [27–29]. Usually, transitions are accompanied by changes in octahedral tilting and bond lengths. Techniques like differential scanning calorimetry (DSC) are used to primarily detect these transitions by measuring the heat flow associated with the phase change. Optical and electronic properties are usually monitored to indirectly observe the effects of a transition, such as changes in the bandgap, in the photoluminescence (PL) peaks, or dielectric properties [30–32].

Based on the nature of the A-site cation in the ABX_3 perovskite structure, materials can be generally classified as hybrid organic–inorganic perovskites (HOIPs) and all-inorganic perovskites. In HOIPs, the A-site is typically occupied by an organic cation such as MA^+, FA^+ or $CH_3NH_2NH_2^+$ (MHy^+). A key advantage of these materials is their exceptional adjustment, which comes from the possibility of modifying both the organic A-site cation and the halide X-site anion. The organic cations introduce additional versatility, as their size, polarity, and dynamic nature influence the lattice and, in turn, the optical characteristics of the material. Although fundamental characteristics such as high optical absorption are determined by the inorganic framework, the organic component can fine-tune the absorption spectrum by changing the lattice structure and band gap [33–35]. However, HOIPs have a significant disadvantage, they are environmentally unstable, susceptible to degradation when exposed to ultraviolet (UV) radiation, moisture, oxygen, or extreme conditions. In all-inorganic perovskites the A-site position is filled by a monovalent inorganic cation (e.g., Cs), and in contrast, their entirely inorganic framework provides improved thermal and chemical stability. Cesium-based perovskites can preserve their structural and functional integrity under more extreme conditions. This makes them highly promising for technologies where long-term reliability is important, including outdoor solar modules and high-power light-emitting diodes (LEDs).

The performance and durability of perovskite materials are significantly influenced by the presence and behaviour of defects within their crystal structure. The defects, which can arise during synthesis or develop over time during device operation, are critical determinants of device efficiency and stability. Intrinsic defects commonly found in perovskites include vacancies (missing atoms), interstitials (extra atoms at non-lattice sites), and antisite defects (atoms occupying incorrect lattice positions). Among them, halide vacancies are particularly prevalent in halide perovskites and have a major impact on the dynamics of charge transport and recombination. While some perovskites exhibit relatively high defect tolerance, meaning that their electronic properties are not severely compromised by certain types of defects, others are susceptible to trap-assisted recombination. In such cases, defect sites act as recombination centers that reduce charge-carrier lifetimes and hinder photovoltaic or luminescent performance. Moreover, mobile ionic defects can migrate under electric fields, causing hysteresis effects in current-voltage measurements and long-term instability in device performance. Beyond intrinsic point defects, environmental exposure is a major cause of perovskite degradation. Water molecules can easily interact with organic cations or halide ions, initiating hydrolysis and leading to the decomposition of the perovskite into non-functional by-products such as PbI_2. Oxygen, especially under illumination, can promote oxidative degradation processes, breaking down both organic and inorganic components. Thermal stress can induce structural phase transitions or accelerate chemical decomposition, while UV exposure may generate free radicals that degrade the perovskite framework or surrounding transport layers. To address these challenges and enhance the stability of perovskite materials, various strategies have been developed. One approach is chemical doping, where small amounts of foreign atoms are introduced to modulate the electronic structure or stabilize specific crystal phases. Doping can effectively reduce the density of deep-level traps, enhance carrier mobility, or suppress ion migration. Another effective method is surface passivation, which involves coating the perovskite layer with materials that neutralize surface defects and prevent environmental influences. Common passivation agents include small organic molecules, halide salts, or wide-bandgap semiconductors. Lastly, encapsulation has proven essential for protecting perovskite devices from ambient conditions. Using barrier layers made of polymers, glass, or metal oxides, the perovskite is sealed from moisture and oxygen, greatly enhancing its operational lifetime.

1.2 Low-dimensional perovskites

Perovskites are often classified by their dimensionality. In addition to the extensively studied three-dimensional (3D) ABX_3 perovskite structures, a wide variety of low-dimensional perovskite materials with distinct properties have been discovered. These include two-dimensional (2D), one-dimensional (1D), and zero-dimensional (0D) architectures, distinguished by a progressive reduction in the connectivity of their BX_6 octahedra. The change in dimensionality significantly affects the structural, electronic, and optical features of these materials.

Among these, 2D perovskites, typically represented by the formula A_2BX_4, have attracted particular attention. In this framework, the metal halide octahedra (BX_6) form layers that are separated by bulky organic cations (A), which effectively confine charge carriers to move within the plane of the layers. The restriction of electron motion to two dimensions results in strong quantum confinement effects. As a consequence, 2D perovskites exhibit large exciton (electron-hole pair) binding energies, intense PL, and tunable emission spectra, making them highly promising for applications in light-emitting devices and photodetectors [36–38]. 1D perovskites are characterized by chains of corner-sharing, edge-sharing or face-sharing octahedra. [39–42]. 0D perovskites, in contrast, are composed of isolated BX_6 units that are fully disconnected from each other and surrounded by organic or inorganic cations [41,43–45]. The reduced connectivity in 1D and 0D structures alters the behaviour of charge carriers and excitons within the crystal, often leading to sharp emission peaks and unique absorption features. The low-dimensional structures generally demonstrate higher structural and environmental stability compared to their 3D counterparts. In 2014, Smith et al. [46] introduced a solar cell design using a layered hybrid perovskite as the light-absorbing material. This configuration demonstrated improved moisture resistance and provided the advantage of fabrication under ambient conditions. The enhanced stability is due to the protective role of the surrounding organic or inorganic units, which effectively shield the perovskite framework from moisture and oxygen [47]. Overall, low-dimensional perovskites expand the design possibilities beyond traditional 3D networks. For example, Zhang et al. emphasize that converting perovskites to 2D “allows multiple functionalities of light generation, emission, transmission, and detection in one material” [48]. Likewise, Hong et al. highlight that low-dimensional halide perovskites display unique optical and charge-transport properties not seen in bulk materials [49]. Their customized structures, rich photophysical properties, and higher resistance to degradation make them an exciting area of study in both fundamental materials science and in the development of next-generation optoelectronic devices.

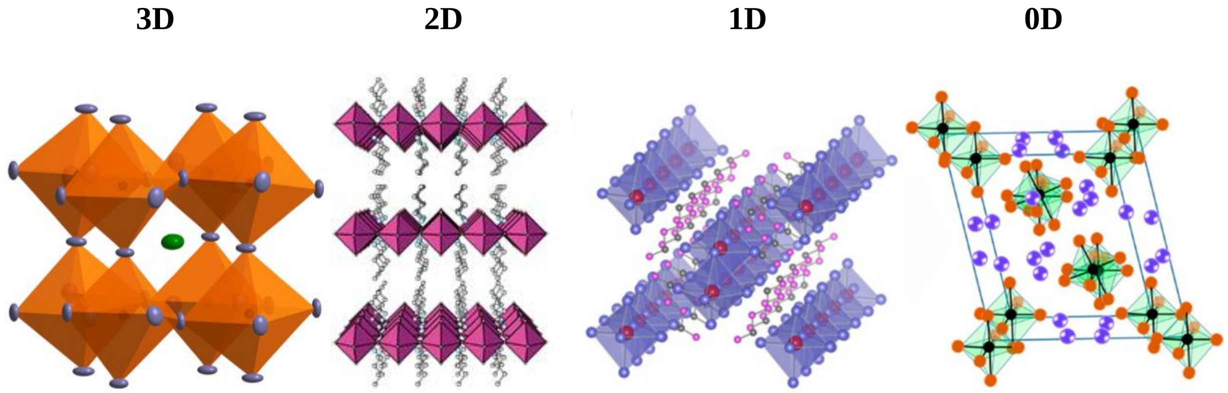

Figure 3. Examples of crystal structures of the metal halide perovskites, categorized by their dimensionality (3D, 2D [50], 1D [51], and 0D [52]).

1.3 Optical properties of halide perovskites

The remarkable optical properties of halide perovskite materials originate from their unique crystal structure, especially from the corner-sharing network of BX_6 octahedra. The electronic band structure is principally determined by the degree of orbital overlap between the B-site metal cation and the X-site halide anion. In lead halide perovskites, which are among the most extensively studied systems, the conduction band minimum (CBM) is formed from the Pb^{2+} 6p orbitals, while the valence band maximum (VBM) from both Pb^{2+} 6s and halide p orbitals [53]. Therefore, the bandgap and optical transitions are directly affected by the geometric arrangement and distortion of the octahedra. Density functional theory (DFT) calculations reveal that the VBM and CBM are strongly influenced by the B–X bond length and B–X–B angle. Increased B–X orbital overlap, achieved through structural compression (either by pressure or chemical substitution), tends to lower the bandgap [54] (see Figure 4a). Conversely, lattice distortions or octahedral tilting, which reduce orbital overlap, often increase the bandgap [54,55] (see Figure 4b). Tunability can be accomplished by several methods, including compositional engineering (e.g., substitution of anions or cations) [56–59], decrease of dimensionality, or the use of external stimuli such as pressure and temperature. This allows a precise control of optical absorption and emission, enabling perovskites to be modified for specific purposes, from blue to near-infrared light emitters and absorbers. For example, substituting bromide with iodide shifts the absorption edge to longer wavelengths (red-shift) [56], while substitution with chloride results in a wider bandgap and blue-shifted emission [60].

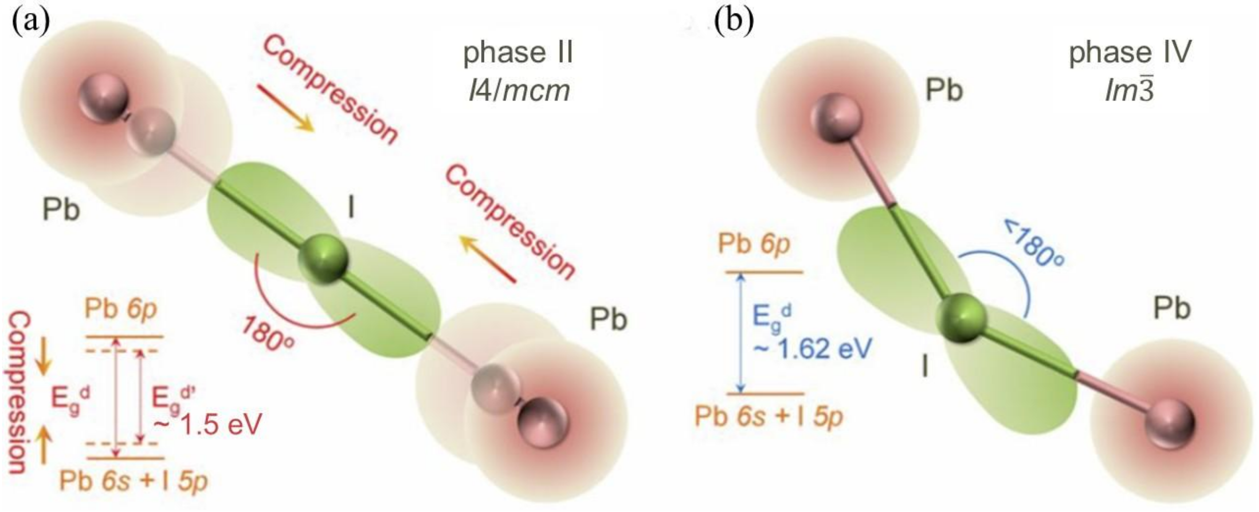

Figure 4. Scheme of (a) band gap narrowing due to bond length shortening in phase II of $MAPbI_3$ and (b) band gap widening due to bond angle decrease at the pressure-induced transition to phase IV, after ref. [54]. The original symmetry of phase IV (*Imm*2) was corrected according to ref. [61].

Quantum confinement plays a particularly important role in nanoscale or layered perovskite structures. In bulk materials, electronic states are continuous, but when confined to nanoscale dimensions, these states become quantized, forming discrete energy levels similar to those observed in atoms [62,63]. As the crystal thickness decreases, the energy difference between the valence and conduction bands widens, causing the material to absorb and emit photons of higher energy, corresponding to shorter wavelengths. Confined structures increase the Coulomb interaction between the electrons and holes facilitating stable excitons with large binding energies even at room temperature [64–66]. In addition, the photoluminescence quantum yield (PLQY), which quantifies the efficiency of photon emission, can also be substantially improved in such structures due to a reduction in non-radiative recombination pathways [67].

2. High-pressure studies of photovoltaic perovskites

Pressure offers a "clean" method to tune the properties of the perovskite material without introducing chemical modifications, providing insight into the intrinsic response of the material to mechanical stress and studying its structure-property relationships [68,69]. At the atomic level, external pressure reduces interatomic distances inside the lattice and directly changes the bond angles and lengths of the BX_6 octahedra. These distortions, including octahedral tilting and rotation, frequently drive structural phase transitions and can fundamentally alter lattice symmetry, the electronic band structure, and optical properties. As the B–X orbitals overlap increases under compression, the edges of the valence and conduction band shift (usually narrowing the bandgap) [70], with consequent changes to exciton binding energies, carrier mobilities, and recombination dynamics; compressive strain can also reduce trap densities and thereby enhance radiative recombination and PL efficiency. In some cases, pressure can even induce phenomena such as ferroelectricity [71,72] or pressure-induced light emission [73,74].

In 3D metal-halide perovskites, pressure often triggers structural rearrangements and electronic reconfigurations that induce changes in optical absorption and emission. For example, in methylammonium lead iodide ($MAPbI_3$), compression initially causes a red shift of the absorption edge at very low pressures, but further structural changes under pressure cause abrupt blue shifts and a significant increase in the optical gap as the structure becomes increasingly frustrated and eventually amorphizes [61]. These electronic changes have been correlated with pressure-induced deformation of the inorganic framework and the constrained, disordered orientations of the methylammonium cations. In cesium lead bromide ($CsPbBr_3$), the pressure response is strongly time- and stress-dependent: applied stress can provoke reversible transitions, irreversible chemical transformations that reduce the connectivity of the Pb–Br framework, or amorphization, and the particular route taken depends on the type of stress and on kinetic factors [75]. The observed bandgap narrowing or widening under pressure in these systems has been linked to changes of Pb–X bond lengths and octahedral tilts.

Low-dimensional perovskites exhibit inherent quantum and dielectric confinement effects, which make their electronic and optical properties highly sensitive to structural changes. Pressure can affect these confinement effects by altering interlayer spacing, bond lengths, and the conformations of organic cations, resulting in distinct changes in optoelectronic properties compared to their 3D counterparts. The soft lattice and ionic nature characteristic of hybrid perovskites, which are particularly common in low-dimensional systems, make them extremely sensitive to pressure, allowing a wide range of tunable optical responses [74,76]. For example, pressure can significantly enhance circularly polarized photoluminescence (CPL) in chiral 2D perovskites, a property that is typically weak under ambient conditions. For (S- and R-MBA)$_2$PbI$_4$ (where MBA stands for methylbenzylammonium), the pressure increased the degree of CPL from nearly zero at ambient pressure to as high as 10% at 8.5 GPa [77]. In the case of the 2D perovskite $(C_4H_9NH_3)_2PbI_4$, applying pressure induces a series of phase transitions that significantly alter its optoelectronic properties [78]. For instance, an initial slight pressure causes a phase transition that leads to an abrupt blue shift in the excitonic bandgap due to a decrease in the Pb–I–Pb bond angle. As pressure increases, subsequent phase transitions cause a significant red shift of the bandgap and make the material a more efficient solar absorber. These pressure-induced structural changes also have an effect on carrier lifetime, which can increase or decrease depending on the specific phase transition, directly impacting the luminescent properties of the material. Under hydrostatic pressure, the zero-dimensional material Cs_4PbCl_6 undergoes a series of complex phase transitions that are dependent on the sample's pressure history [79]. While the $PbCl_6^{4-}$ octahedra are relatively resistant to stress, the distances between octahedra contract significantly. The absorption edge initially red-shifts with increasing pressure, whereas at the two successive phase transitions, it undergoes a jump-wise red shift followed by a blue shift. The broad emission band of this material is quenched with increasing pressure. In contrast, $CsPb_2Cl_5$, a perovskite-like layered material, exhibits remarkable structural stability, remaining stable up to at least 4.2 GPa without observed phase transitions [79]. The crystal is highly compressible, but anisotropically, with pressure primarily affecting the Cs^+ layers and only slightly reducing the lengths of the Pb–Cl bonds. The optical absorption edge shows only a slight red-shift, which correlates with the low compressibility of the Pb–Cl layers. The above examples of low-dimensional perovskites under pressure demonstrate a wide range of responses, from CPL enhancement in chiral 2D perovskites to complex phase transitions in 0D perovskites and to remarkable stability in other 2D systems. The manner in which pressure is distributed and absorbed within these different architectures, whether in organic layers, between inorganic chains, or within interstitial spaces, dictates the specific structural distortions.

II. Aims

The main objective of this thesis is to provide fundamental knowledge and comprehensive understanding of the effects of high pressure on perovskite materials, particularly those related to photovoltaic and optoelectronic devices. Perovskite absorbers have attracted widespread attention in materials science and solid-state physics, making them a huge research field favorable to revolutionary discoveries in new technologies. Over the past decade, they have been successfully integrated into high-efficiency photovoltaic devices and hold significant promise for light-emitting applications such as LEDs, multi-colour displays, and lasers, as well as in high-energy radiation detectors [41,79]. This thesis is devoted to the structural and optical behaviour of low-dimensional perovskite materials under hydrostatic compression. High-pressure studies serve as a unique and powerful tool for exploring the limits of stability and tunability of materials, revealing crystalline phases of superior properties that may be thermodynamically unstable under ambient conditions, but can be kinetically trapped or engineered using advanced synthesis techniques. Understanding how this external stimulus affects the perovskite structure and the associated distortions is essential for designing materials with the desired properties for next-generation optoelectronic and photovoltaic devices. Thus, this work makes a fundamental contribution to the future discovery and optimization of perovskites for practical applications, especially in the fields of sustainable energy and advanced optoelectronics.

The specific research objectives of this thesis are:

- Systematic investigation of the pressure-induced structural changes in $CsPb_2Br_5$, Cs_4PbBr_6, $[C(NH_2)_3]_2PbI_4$, and $CsC(NH_2)_3PbI_4$, and determination of their phase stability limits.
- Characterization of the electronic band structure and optical properties evolution, including fundamental absorption edge and photoluminescence, under high pressure.
- Search for correlations between the crystal lattice dimensionality and the observed changes in material properties under high pressure.
- A contribution to better understanding of structure-property relationships in low-dimensional perovskites under extreme conditions.

III. Methodology

1. Synthesis of low-dimensional perovskites

The synthesis of low-dimensional perovskite materials mainly relies on solution-phase crystallization techniques. This method provides control over the chemical environment, which is essential for obtaining high-quality single crystals. The integrity and purity of these crystals are important for accurate material characterization and for determining their intrinsic physical and chemical properties. The general methodology involves dissolving metal halide and organic halide precursors in a suitable solvent system, followed by a controlled cooling process to induce the growth of crystalline structures. All materials discussed herein ($CsPb_2Br_5$, Cs_4PbBr_6, $[C(NH_2)_3]_2PbI_4$, and $CsC(NH_2)_3PbI_4$) were synthesized using this technique. Solution-phase synthesis allows mixing of precursors at the molecular level, which facilitates precise stoichiometric control, although achieving perfect control can be challenging, as observed in certain cases. Furthermore, crystal growth from a supersaturated solution usually yields larger and higher-quality single crystals. Growth processes can be influenced by manipulating solvent properties such as acidity, polarity and temperature, allowing the formation of specific low-dimensional perovskite structures.

The synthesis of the low-dimensional perovskite compounds described in this thesis used high-purity chemicals and reagents without further purification to ensure reproducibility and minimize impurities in the final products. Key common chemicals included cesium carbonate (Cs_2CO_3, Aldrich, 99%), lead(II) acetate trihydrate ($Pb(CH_3COO)_2 \cdot 3H_2O$, Aldrich, 99.999%), hydrobromic acid (HBr, Acros Organics, 48% solution in water), guanidinium carbonate ($[C(NH_2)_3]_2CO_3$, Sigma-Aldrich, 99%), lead(II) iodide (PbI_2, Acros Organics, 99%), and hydroiodic acid (HI, Alfa Aestar, 57% in water, stabilized with 1.5% hypophosphorous acid). Water used in the syntheses was purified by double distillation. A general approach to preparing precursors involved the reaction of carbonate or acetate salts with the corresponding hydrohalic acids. For example, cesium bromide (CsBr) and guanidinium iodide ($C(NH_2)_3I$) were typically obtained by reacting cesium carbonate and guanidinium carbonate, respectively, with hydrobromic acid or hydroiodic acid in aqueous solutions. Similarly, lead(II) bromide ($PbBr_2$) was prepared from lead(II) acetate trihydrate and hydrobromic acid. Such method of in situ formation of the halide precursor ensures high reactivity and solubility, facilitating subsequent crystallization steps. Careful selection and preparation of these precursors are critical, as their purity and precise stoichiometry directly influence the phase purity and crystal quality of the resulting perovskite materials.

The synthesis of $CsPb_2Br_5$ single crystals was carried out with the following starting materials: cesium carbonate (Aldrich, 99%), hydrobromic acid (Acros Organics, 48% solution in water), and lead(II) acetate trihydrate (Aldrich, 99.999%). Before the perovskite formation, cesium bromide (CsBr) and lead(II) bromide ($PbBr_2$) were prepared by reacting hydrobromic acid with cesium carbonate and lead(II) acetate trihydrate, respectively. Stoichiometric amounts of the pre-formed CsBr and $PbBr_2$ were dissolved in hot, double-distilled water that had been acidified with hydrobromic acid. The acidification of the solution with HBr is a critical step that affects the solubility of the precursors and the stability of the desired perovskite phase during crystallization. The hot solution was then allowed to cool slowly to room temperature for the controlled crystallization of thin $CsPb_2Br_5$ plates. After crystallization, the precipitated crystals were isolated by filtration, washed with hexane to remove any residual solvent or unreacted precursors, and then dried. To ensure the high-quality, pure crystals, a systematic series of crystallizations was performed. These experiments included modification of parameters such as the amount of HBr acid in the solution and/or the CsBr:$PbBr_2$ stoichiometric ratio. This optimization process highlights the sensitivity of perovskite crystallization to subtle changes in solution chemistry and stoichiometry, where precise control of these factors is essential for achieving the desired phase purity and crystal morphology.

For the formation of Cs_4PbBr_6, cesium bromide (CsBr) was prepared by reacting cesium carbonate (Cs_2CO_3, Aldrich, 99%) with hydrobromic acid (HBr, Acros Organics, 48% water solution) in an aqueous medium. Stoichiometric quantities of CsBr, dissolved in water, and $PbBr_2$, dissolved in HBr, were combined. Usually, a precipitate formed when these solutions were mixed. To achieve a completely transparent solution necessary for controlled crystallization, N,N-dimethylformamide (DMF, Eurochem, grade for analysis) was gradually added to the mixture while it was heated to a temperature range of 70–100°C with constant stirring. The addition of DMF helped to increase the solubility of the precursors, ensuring a homogeneous solution from which crystallization could proceed. After complete dissolution, the solution was left to cool slowly, allowing for crystal formation. Despite the efforts to control the synthesis, achieving complete control over the crystallization conditions for Cs_4PbBr_6 proved challenging. This was mainly due to the different evaporation rates of the mixed solvents (HBr, H_2O, and DMF) and the lengthy dissolution process, which typically lasted 2–3 hours. The dynamic changes in solvent composition due to differential evaporation can significantly alter the solubility and supersaturation levels, making it difficult to maintain consistent conditions throughout the crystallization period. Although the composition of the solution significantly influences the outcome, the crystallization rate was identified as a potentially more critical factor. Crystallization could occur spontaneously at room temperature or upon cooling, both of which affected the type and colour of the obtained crystals. Furthermore, limiting the evaporation of the solution also impacted the crystallization conditions, indicating the delicate balance required for precise control. The inherent variability of the process was evident, as repeated crystallization procedures yielded Cs_4PbBr_6 crystals of various colours, including colourless, green, and yellow. Notably, different crystal types, such as green and colourless, were even observed simultaneously from the same reaction beaker.

The syntheses of the iodide-based low-dimensional perovskites, $[C(NH_2)_3]_2PbI_4$ and $CsC(NH_2)_3PbI_4$, were carried out using a similar solution-phase methods, with emphasis on the role of an acidic medium for precursor dissolution and controlled cooling for crystallization. Common chemicals and reagents used for these syntheses, without further purification, included guanidinium carbonate (99%, Sigma-Aldrich), caesium carbonate (99%, Sigma-Aldrich), lead(II) iodide (99%, Acros Organics), and hydroiodic acid (57% in water, stabilized with 1.5% hypophosphorous acid, Alfa Aestar). Analogous to the bromide systems, caesium iodide (CsI) and guanidinium iodide ($C(NH_2)_3I$) were obtained by the reaction of their respective carbonates with hydroiodic acid and subsequently used as substrates for the perovskite syntheses. $[C(NH_2)_3]_2PbI_4$ was synthesized in a non-stoichiometric solution, specifically one containing an excess of $C(NH_2)_3I$. 10 mmol of $C(NH_2)_3I$ was dissolved in hot water (80°C) acidified with HI, and then the hot solution of 3 mmol of PbI_2 dissolved in 10 ml of HI was added dropwise with constant stirring. The dropwise addition and continuous stirring are crucial for maintaining homogeneity and preventing localized supersaturation, which could lead to uncontrolled precipitation. Slow cooling of the resulting solution to room temperature facilitated the crystallization of yellow plates. The precipitated crystals were then collected, washed with diethyl ether to remove impurities and residual solvent, and dried. The yield obtained for $[C(NH_2)_3]_2PbI_4$, determined relative to PbI_2, was approximately 60%.

$CsC(NH_2)_3PbI_4$ was prepared from a hot acid solution following a procedure previously described by Nazarenko et al [80]. The synthesis involved dissolving 2 mmol of PbI_2, 2 mmol of CsI, and 8 mmol of $C(NH_2)_3I$ in 13 ml of hydroiodic acid. The solution was heated and stirred until all substrates were completely dissolved, ensuring a homogeneous reaction mixture. Following complete dissolution, the solution was allowed to cool slowly from 80°C to room temperature over several hours. This long cooling period is critical for promoting the growth of large, well-defined red crystals, indicative of the mixed-cation perovskite phase. The resulting red crystals were harvested, washed with diethyl ether, and dried. The estimated yield for $CsC(NH_2)_3PbI_4$ was approximately 65% in relation to PbI_2.

2. Calorimetric and thermogravimetric analysis

Thermal analysis techniques are indispensable tools in materials science, providing a deep understanding of the fundamental behaviour of novel compounds under varying thermal conditions. Among these, DSC and thermogravimetric analysis (TGA) stand out as complementary methods for comprehensively characterizing material stability, decomposition pathways, and structural transformations as a function of temperature or time. For perovskite materials, with their sensitivity to temperature, thermal analysis is particularly important [81]. Measurements in nitrogen atmosphere aim to isolate and study the inherent thermal behaviour of the materials. Perovskites frequently exhibit complex phase transitions and are prone to thermal degradation in high temperatures, phenomena that significantly impact their functionality in advanced devices [82].

DSC is a thermal analytical technique that precisely measures the heat flow into or out of a sample as a function of temperature or time, relative to an inert reference material. Although the measurement principle varies depending on the instrument design (e.g., in the case of systems with heat flux or power compensation), the basic function remains the same: the instrument determines the difference in heat flow between a sample and a reference material when they are subjected to an identical, controlled temperature program. When a thermal event occurs in a sample, such as a phase transition or chemical reaction, the sample either absorbs heat (an endothermic process) or releases heat (an exothermic process). This differential heat flow is accurately measured, resulting in a thermogram that displays peaks corresponding to these thermal events. From these peaks, quantitative thermodynamic information can be determined, including heat flow rate, enthalpy change (ΔH), and changes in heat capacity (ΔC_p).

The DSC experiments in this study were performed using a TA Instruments Q2000 calorimeter. This device operates on the principle of a heat-flux DSC, measuring the temperature difference between the sample and reference pans. This difference is directly proportional to the heat flow. The instrument is equipped with a highly sensitive thermocouple located symmetrically between the sample and reference crucibles. The main components of the Q2000 also include a precisely controlled furnace, a sample holder, a reference holder, a 50 position autosampler, an autolid, dual digital mass flow controllers for precise control of purge gases (such as nitrogen) to ensure a stable, inert atmosphere, and a data acquisition system for recording the thermal signals. The Q2000 model has broad temperature range capabilities (-180 to 725 ˚C) and high resolution (±0.01 ˚C), enabling the detection of even minor thermal events. For DSC measurements, careful sample preparation and precise control over experimental parameters are paramount to obtaining reliable data. The selection of crucible material is a critical factor, determined by the expected temperature range, potential reactivity of the sample, and the thermal conductivity requirement. Aluminum crucibles are the standard for DSC due to their excellent thermal conductivity and suitability for temperatures below 660 °C. Samples of the mass ranging from 5 to 10 mg ensured optimal heat transfer. The accurately weighed sample was carefully loaded into the crucible to ensure complete coverage of the bottom, thereby maximizing thermal contact and promoting uniform heating. Gloves and tweezers were used to handle the samples to avoid any contamination of the sample and the furnace. For $CsPb_2Br_5$, measurements were performed on as-grown crystals, while for Cs_4PbBr_6, $[C(NH_2)_3]_2PbI_4$, and $CsC(NH_2)_3PbI_4$, powdered samples were used. All DSC experiments in this study were carried out with a consistent temperature change rate of 10 K min^{-1}.

TGA is a quantitative thermal analysis technique that measures the change in mass of a sample as a function of temperature or time. The fundamental principle of TGA is that any physical or chemical process involving a change in mass, such as thermal decomposition, desorption, evaporation, or oxidation, will be detected as the sample is heated or cooled. However, physical changes like melting or crystallization, that are not associated with mass loss will not be directly observed in a TGA curve. The instrument continuously records the mass of the sample, generating a thermogravimetric curve, which plots the mass or percentage of initial mass as a function temperature or time. TGA is extensively applied for evaluating thermal stability, determining decomposition temperatures, or quantifying moisture and volatile content.

TGA in this study was performed using a TA Instruments TGA Q50 apparatus. This model comprises a highly sensitive analytical balance, a furnace, a sample holder (crucible), and a purge gas system designed to maintain a controlled atmosphere around the sample. The TGA Q50 has high sensitivity (0.1 µg) and precision (±0.01% mass precision), enabling the detection of even small changes in mass. The furnace is capable of heating samples up to 1000 °C. For TGA measurements, careful sample preparation and precise control of experimental parameters are essential for obtaining accurate results. All TGA runs for the studied perovskite materials were performed on powdered samples. Powdered samples are generally preferred for TGA because they facilitate complete and uniform decomposition, which ensures a more representative mass-loss profile. Samples were accurately weighed ranging from 10-20 mg and placed in a crucible made of platinum, which was selected for its ability to withstand high temperatures and prevent undesirable reactions with the sample. Maintaining sample purity and using careful handling techniques are also crucial to avoid contamination that could disturb the analysis. A constant heating rate of 10 K min^{-1} was applied in all TGA experiments.

3. Structural and optical measurements at room temperature and as a function of temperature

This section describes the experimental procedures and setups used for characterizing the structural and optical properties of low-dimensional perovskite materials under ambient conditions and in a range of different temperatures. Single-crystal X-ray diffraction (SCXRD) is a non-destructive analytical technique that provides highly detailed information about the internal lattice of crystalline substances. Its fundamental principle is based on the interaction between an incident X-ray beam and the regularly arranged atoms in a crystal lattice. When X-rays strike a crystal, they are diffracted in specific directions, creating a unique diffraction pattern. This pattern is a direct consequence of the three-dimensional arrangement of atoms in the compound, including lattice parameters, symmetry, atomic positions, bond lengths, and bond angles. To collect complex diffraction data, the crystal is systematically rotated during the experiment, allowing the capture of diffraction from various orientations. The choice of X-ray source is critical, Mo light sources are particularly advantageous for studying structures that contain heavy atoms, such as lead and cesium. The accuracy of SCXRD results is fundamentally dependent on the quality of the crystal samples. Optimal crystals for SCXRD should be free of defects and large, ranging from 50 to 300 microns in size. All SCXRD experiments, including those at different temperatures and high pressures, were performed using an Oxford Diffraction Gemini A Ultra diffractometer (Figure 5). This instrument operated with graphite-monochromated Mo Kα radiation, with a characteristic wavelength (λ) of 0.71073 Å. Data collection and initial processing were carried out using

CrysAlisPro software [83]. Subsequent structure solution and refinement were performed using SHELX programs [84] and Olex2 software [85]. These software packages enable the transformation of raw diffraction data into precise atomic models. Crystallographic information files (CIFs) for the structures determined were deposited in the Inorganic Crystal Structure Database or in the Cambridge Crystallographic Data Centre. Structural changes as a function of temperature provide crucial insights into phase transitions, thermal expansion, and molecular dynamics within materials. A Cryostream Plus cooler (Oxford Cryosystems) was used for temperature-dependent SCXRD measurements of $CsC(NH_2)_3PbI_4$. This system offers a broad temperature range capability, and for our study, it was used to provide precise temperature control of the sample in a range from 200 K to 380 K, with an accuracy of ±0.1 K. This high level of temperature accuracy is essential for identifying and characterizing subtle structural changes, such as phase transitions or continuous changes in lattice parameters, that occur in response to thermal stimuli.

Figure 5. Oxford Diffraction Gemini A Ultra diffractometer.

Ultraviolet-visible (UV-Vis) absorption spectroscopy is based on the principle that chemical compounds absorb ultraviolet or visible light, resulting in the appearance of different absorption spectra. This process involves the interaction between light and matter, where the absorption of photons causes electrons within the material to transition from a ground state to an excited state with a higher energy. The energy difference between these states is exactly equal to the energy of the absorbed radiation. For semiconductor materials like the studied perovskites, the onset of strong absorption, known as the absorption edge, is directly correlated with the energy of the electronic band gap. A UV-Vis spectrophotometer operates by measuring the intensity of light transmitted through a sample (I) and comparing it to the initial intensity of the light source (I_0). Measurement involves a baseline measurement to establish a reference, followed by a sample measurement. The absorbance, $A = -\log(T)$, where T is transmittance (I/I_0), is then plotted as a function of wavelength. UV-Vis absorption spectra were collected using a Jasco MSV-5100 microscopic spectrophotometer. This instrument is equipped with dual light sources, deuterium and tungsten lamps, allowing spectral measurements in the 230–900 nm range. This unique spectrophotometer allows one to select an area in the sample with a small diameter of up to 10 μm, which is advantageous for measuring the defect-free area of individual crystals. In our case, a sample area of 30 μm, a continuous scan speed of 200 nm min^{-1}, and a spectral bandwidth of 5 nm were applied for all measurements. For the bandgap determination, the absorption edges were analyzed using Tauc plots [86] by plotting the squared product of the absorption coefficient (α) and the photon energy ($h\nu$), i.e., $(\alpha h\nu)^2$ against $h\nu$. The optical properties of $[C(NH_2)_3]_2PbI_4$ and $CsC(NH_2)_3PbI_4$ were investigated as a function of temperature. To change and control the temperature of the sample, a Linkam THMSE600 stage was integrated into the spectrophotometer, allowing for measurements over a broad temperature range from 79 K to 458 K.

The thickness of the crystal studied is a critical parameter in optical absorption measurements, especially in the transmission mode. If the sample is too thick, it can lead to saturation or complete absorption of the incident light. Under such conditions, it is only possible to determine the absorption edge of the material, but not its full absorption spectrum. Conversely, very thin samples allow for detection of inherent spectra of the materials. Optical microscopy was used to determine sample thicknesses; however, for thin plates below 5 μm, the optical interference method was employed. When light interacts with a thin film, partial reflections occur on its top and bottom surfaces. Reflected beams travel different optical path lengths and interfere with each other, producing an interference pattern characterized by oscillations in the recorded absorption spectrum. This pattern is directly dependent on the film thickness, its refractive index (n), and the wavelength of light (λ). By analyzing the number and position of interference fringes and applying models that incorporate the known refractive index of the material across the measured wavelength range, the film thickness can be accurately estimated. However, the accuracy of this method may be affected by factors such as surface roughness and uncertainties in the optical constants used for the calculations.

The fundamental principle of PL involves the emission of light from a material after it absorbs photons. When a photon is absorbed, it excites an electron to a higher electronic state. Then the excited electron rapidly nonradiatively relaxes to the lowest excited state. As it returns to a lower energy state, it releases energy in the form of a photon, and this emitted light is referred to as PL. The combined use of UV-Vis absorption and PL spectroscopy provides a comprehensive understanding of both the absorption characteristics and the emission properties of the perovskite materials. PL signals were measured using a homemade attachment integrated with the Jasco MSV-5100 spectrophotometer. The customized setup allowed us to adjust excitation source using a xenon lamp in combination with optical filters. An aperture of 100–400 μm was used to control the excitation light reaching the sample. In semiconductors, the PL emission peak is often observed close to the absorption edge. Therefore, to effectively excite PL, the excitation light must have a higher energy than the bandgap of the material. Based on this requirement, excitation wavelengths in the range of 250–320 nm and 320–500 nm were used primarily. The light emitted by the sample was subsequently analyzed by a Spectra Academy SV2100 spectrometer.

4. Structural and optical measurements under high pressure

High-pressure experiments are essential for understanding how external mechanical stress influences the crystal structures and phase stability of materials. The diamond anvil cell (DAC), a schematic of which is shown in Figure 6, is a widely used tool for generating high pressure, which can be used for both structural and optical measurements. The principle of DAC operation is based on compressing a sample between two opposing diamond anvils. Pressure is applied by using a clamping mechanism with screws, allowing for precise, gradual increase in force. The sample can be viewed through diamonds and illuminated with optical beams or X-rays. For high-pressure SCXRD experiments, a Merrill-Bassett DAC [87] equipped with symmetrical type Ia diamond anvils (0.8 mm culet diameter) supported on steel discs with conical windows was used. The pressure chamber in the DAC was created by spark-eroding a hole in a metal gasket, which is placed between diamond anvils. Tungsten gaskets (for $CsPb_2Br_5$) and steel gaskets (for Cs_4PbBr_6, $[C(NH_2)_3]_2PbI_4$, and $CsC(NH_2)_3PbI_4$) with initial thickness of 250 μm and holes of 350–380 μm diameter were used. A selected single crystal of the perovskite material, along with a small ruby chip for pressure calibration, was carefully loaded into the high-pressure cell and glued to one of the diamond culets. The pressure chamber was then filled with a hydrostatic pressure-transmitting medium, isopropanol or Daphne Oil 7575, ensuring hydrostatic conditions to about 4 GPa [88–90]. Consistent results in different hydrostatic media confirm that the polarity of the solvent did not significantly affect the measured properties within the studied pressure range. The pressure was monitored using the ruby fluorescence method, based on the wavelength shift of the R_1 ruby ($Al_2O_3:Cr^{3+}$) luminescence line, and calculated using a standard calibration equation [91,92]. To obtain precise pressure values, the ruby peak was fitted using a Gaussian function. Under pressure, the characteristic ruby fluorescence peak shifts to longer wavelengths, as illustrated in Figure 7. Readings were taken both before and after each measurement. The pressure calibration accuracy was below 0.03 GPa, which was important for the analysis and interpretation of the results. The DAC was mounted on the Oxford Diffraction Gemini A Ultra diffractometer. Before data collection, the DAC was centered using the gasket-shadowing method [93]. The alignment ensures that the X-ray beam passes optimally through the sample within the pressure chamber, minimizing scattering from the gasket or diamond anvils to enhance data quality.

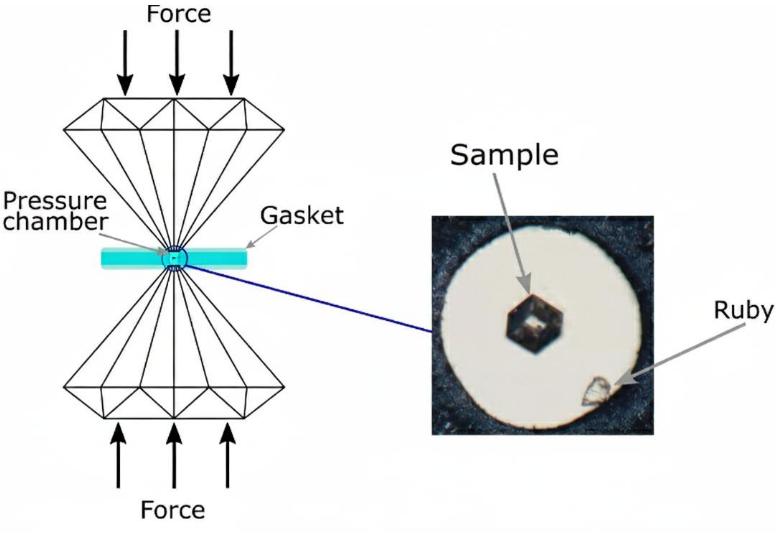

Figure 6. Scheme of the diamond anvil cell.

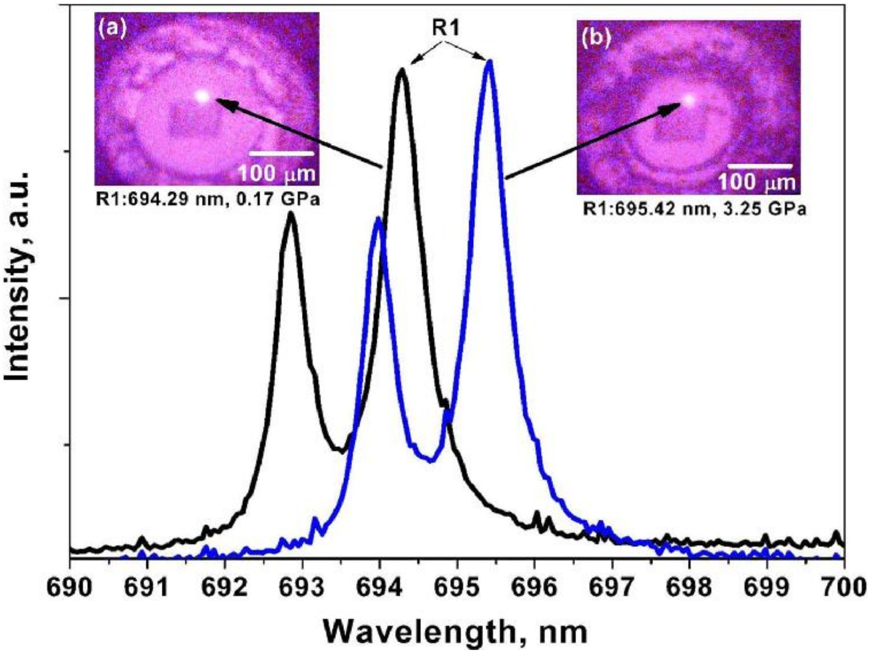

Figure 7. Fluorescent spectra of the ruby crystal in the DAC at 0.17 and 3.35 GPa [94].

In parallel with structural investigations, optical properties under high pressure were studied to understand the impact of compression on the electronic band structure and light-matter interactions. For high-pressure optical spectroscopic measurements, DAC equipped with type IIa diamond anvils was used. Type IIa diamonds have a significantly lower nitrogen content compared to type Ia diamonds, which substantially reduces their intrinsic fluorescence and minimizes absorption across wide spectral range, making them well-suited for optical experiments. High-pressure absorption spectra were recorded using the Jasco MSV-5100 microscopic spectrophotometer. The hydrostatic liquid and other experimental details, such as sample loading and gasket preparation, were analogous to those used in the high-pressure diffraction experiments. PL measurements under high pressure were carried out using the homemade attachment to the Jasco spectrophotometer, as described in Section III.3. All high-pressure measurements were performed at room temperature.

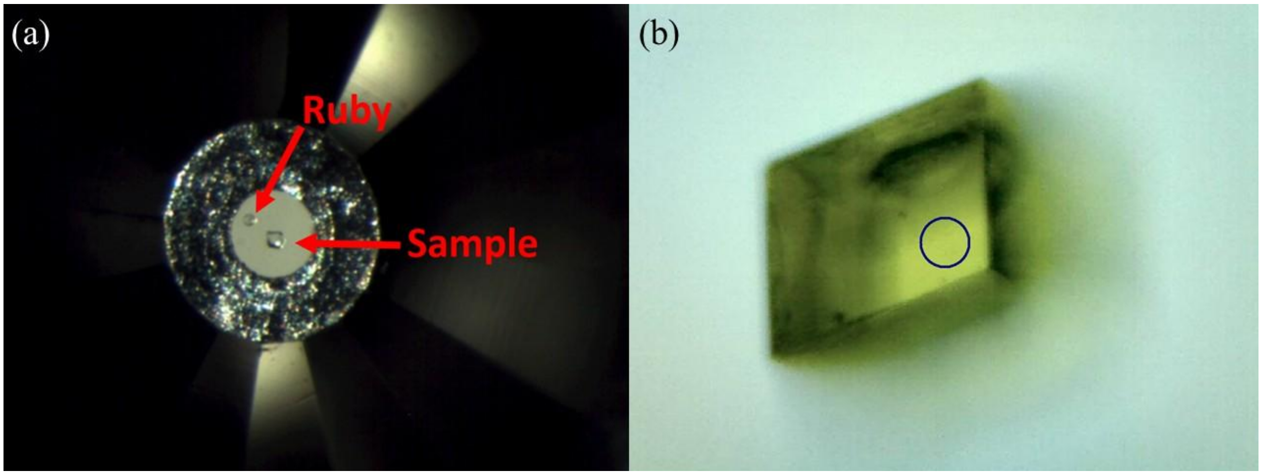

Figure 8. (a) Ruby and sample loaded in DAC, (b) sample in DAC studied within selected 10 µm diameter area by Jasco MSV-5100 microscopic spectrophotometer.

IV. Summary of publications

1. *Thermodynamic stability, structure, and optical properties of perovskite-related $CsPb_2Br_5$ single crystals under pressure* [95]

The $CsPb_2Br_5$ crystals belong to a class of quasi-two-dimensional inorganic perovskite-like materials and have become a popular topic of studies. However, numerous articles on the physical properties of $CsPb_2Br_5$ contain contradictory data. Previous studies have often reported misleading information regarding, for example, the band gap value, the presence of absorption and luminescence in the visible range, and the phase stability of the material [96–99]. In this paper we present an in-depth thermodynamic structural and optical characterization of pure $CsPb_2Br_5$ single crystals under hydrostatic pressure. Our comprehensive approach aimed not only to provide new experimental data, but also to clarify the fundamental understanding of the material properties.

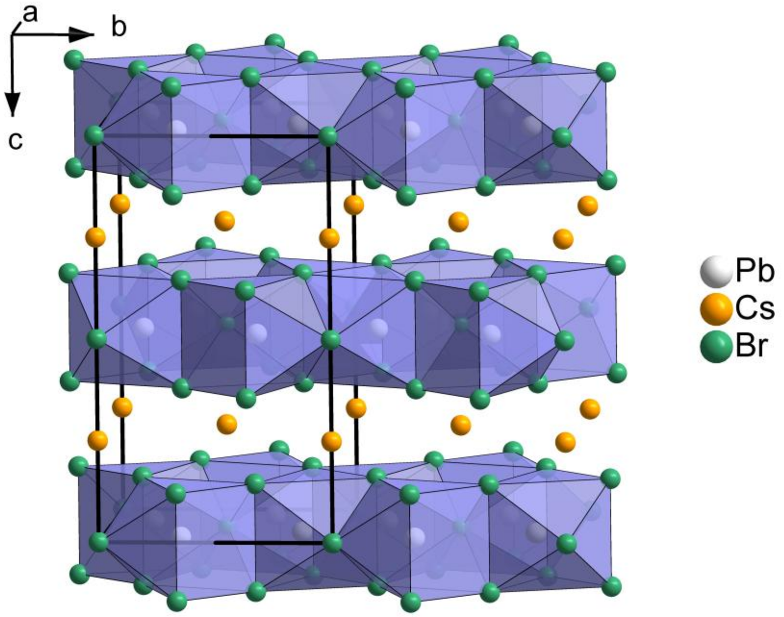

Figure 9. Crystal structure of $CsPb_2Br_5$ [95].

DSC and TGA studies showed that the material is stable over a wide temperature range, from 95 K to 625 K. The only DSC anomaly was observed at 625 K, which corresponds to the melting point of the crystal. This result definitively contradicts the previously observed thermal anomaly at

341.5 K [100], which may originate from impurities. Detailed structural studies were performed using SCXRD in the pressure range up to 4.2 GPa. The results showed that the lattice parameters were shortened and the unit cell volume decreased under hydrostatic compression. The symmetry of the space group *I*4/*mcm* was preserved throughout the studied pressure range. It contradicts previously published data on an isostructural phase transition at approximately 1.6 GPa [99], where the observations could result from the contaminated samples and non-hydrostatic conditions of experiments. The lattice parameters and unit cell volume data were described by the third-order Birch-Murnaghan equation of state. The determined volumetric compressibility modulus B_0 = 11.5(3) GPa and its derivative B_0' = 9.3(6). These values indicate that $CsPb_2Br_5$ is relatively soft as for an inorganic material, but the high value of B_0' is justified by the layered structure. The compressibility of $CsPb_2Br_5$ is strongly anisotropic, significantly higher along the *c* direction (perpendicular to the layers) than in the *a*−*b* plane. Within the structure, layers composed of Cs^+ cations are more susceptible to external hydrostatic pressure than Pb−Br layers. The Pb−Br layers, which consist of face-sharing bicapped $PbBr_8$ trigonal prisms, are characterized by eight Pb–Br bonds with three distinct bond lengths. With increasing pressure, the six longest Pb−Br bonds contract, while the two shortest bonds slightly lengthen.

Furthermore, the optical properties of pure $CsPb_2Br_5$ under pressure have been studied. The absorption edge of the pure material was observed in the ultraviolet, around 350 nm. This edge continuously red-shifted with increasing pressure. A narrowing of the energy gap was well correlated with pressure-induced structural changes. The energy gap decreases monotonically with increasing pressure, exhibiting a linear behaviour up to about 4 GPa. The overall reduction in the energy gap over the studied pressure range up to 6 GPa is about 0.1 eV. The energy gap is determined mainly by the structure of the Pb−Br layers and their modifications under pressure. The shortening of the six longest Pb−Br bonds under compression increases the overlap of the atomic orbitals, which leads to an upward shift of the valence band maximum and, consequently, a redshift of the energy gap. In this work, a thin $CsPb_2Br_5$ plate, only 30 nm thick, was crystallized directly on the surface of the diamond culet. The thickness of the plate was precisely determined using atomic force microscopy (AFM). Absorption spectral measurements for this thin layer revealed a clearly visible excitonic band structure in the 320-330 nm range, allowing for the precise determination of the absorption edge. Comparison of optical results for samples of different thicknesses, including a 3.9 μm-thick microplate and the previously mentioned 30 nm nanoplate, showed that the nature of pressure-induced changes is the same, regardless of sample thickness. The only noticeable difference was that the energy gap obtained for the thicker sample was significantly lower, which is expected for samples with significantly different thicknesses. At atmospheric pressure the band gap was determined to be around 3.58 eV for 3.9 μm thick crystal and 3.73 eV for 30 nm thick sample.

A key insight that resolved many previous controversies was understanding the role of sample purity. Our study clearly demonstrated that optical absorption in the visible range and green PL, which had been wrongly attributed to $CsPb_2Br_5$ in the past, are not intrinsic properties of the pure material. Instead, these observed features result from the presence of microcrystallites of the 3D perovskite $CsPbBr_3$, which are deposited on the surface of $CsPb_2Br_5$ plates (as shown in Figure 10c), rather than being embedded inclusions. Therefore, the methodology for the preparation and purification of $CsPb_2Br_5$ is crucial, as even a small amount of $CsPbBr_3$ can significantly affect the optical properties, leading to misleading information and misinterpretation of data. Thus, our results obtained for pure single crystals differ significantly from previously published data using samples with $CsPbBr_3$ impurities. In addition, we demonstrated that the diffuse reflectance method, commonly used to determine absorption edges and band gaps, yields optical parameters that are significantly different from those obtained from optical absorption measurements. Such difference indicates a significant discrepancy between the energies of the surface and bulk electronic states of $CsPb_2Br_5$, and may also be characteristic for other similar materials.

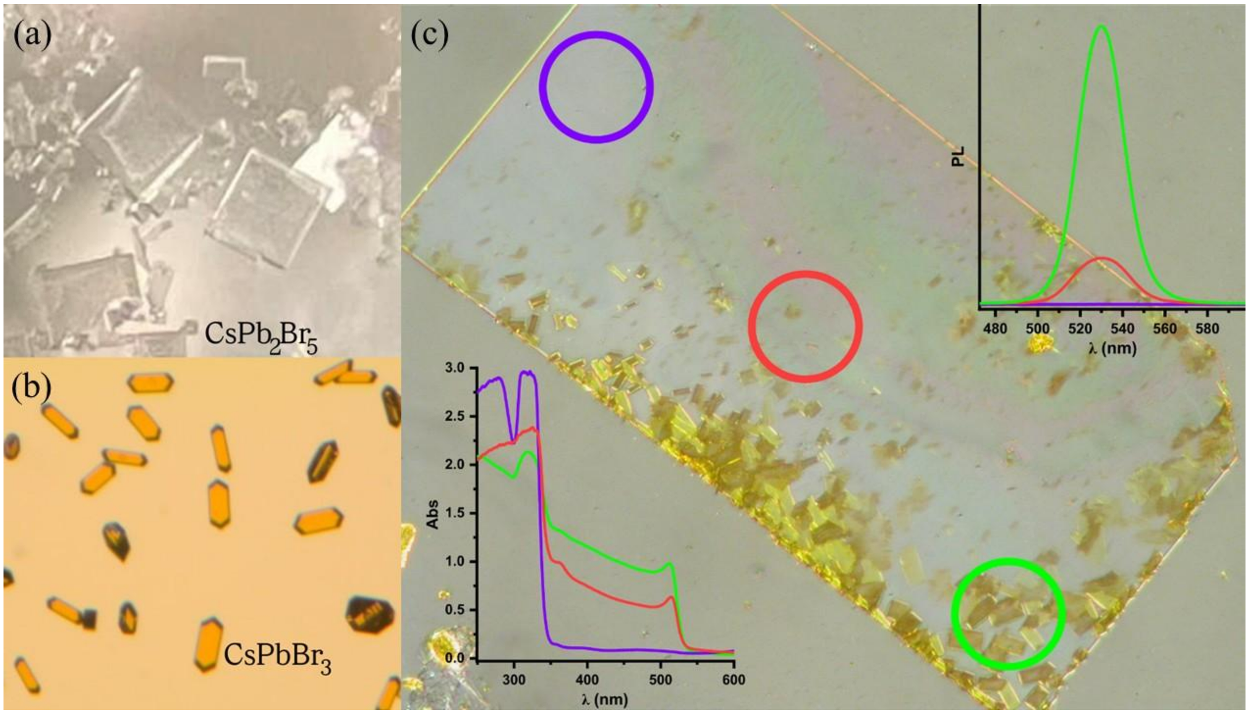

Figure 10. Images of (a) pure $CsPb_2Br_5$ crystal plates; (b) $CsPbBr_3$ crystals; (c) $CsPb_2Br_5$ crystal plate with $CsPbBr_3$ precipitation on its surface. The coloured circles in (c) indicate the 10 µm areas selected for spectrophotometry, with their colours corresponding to the respective absorption and PL spectra shown as insets.

In summary, this article has clarified the long-lasting confusion in the literature regarding the physical properties of $CsPb_2Br_5$. The intrinsic optical properties of the pure material exhibit ultraviolet absorption and there is no PL in the visible region. This study has shown that the layered tetragonal structure of $CsPb_2Br_5$ is exceptionally stable. Structural and spectroscopic experiments conducted on pure single crystals confirmed that this structure persists at least up to 6 GPa. Its structural modifications are precisely correlated with observed bandgap changes. We emphasize the fundamental importance of sample purity for accurate material characterization.

Table 1. Selected properties of pure $CsPb_2Br_5$.

Parameter	*Value*
Thermodynamic stability	
Thermal stability range	at least 95 K – 625 K
Melting temperature	~625 K
Structural stability under pressure	
Crystal system, space group	tetragonal, *I*4/*mcm*
Structural stability range under pressure	up to at least 6 GPa
Compressibility	
Bulk modulus (B_0)	11.5(3) GPa
Derivative of bulk modulus (B_0')	9.3(6)
Optical properties	
Absorption edge	~350 nm
Band gap type	indirect
Total band gap reduction under pressure (up to 6 GPa)	~0.1 eV

2. *White-light emission triggered by pseudo Jahn–Teller distortion at the pressure-induced phase transition in Cs_4PbBr_6* [101]

This work presents a comprehensive study of the zero-dimensional all-inorganic perovskite Cs_4PbBr_6 under pressure using SCXRD, optical absorption, and PL. The experimental results were further supported by electronic band structure calculations, providing a deep understanding of the observed phenomena. The aim of this study was to resolve existing controversies in the literature regarding the physical properties of this material, in particular its behaviour under pressure and the origin of pressure-induced light emission. In 0D perovskites, the BX_6 octahedra are isolated, leading to strong localization of electronic states responsible for optical properties. Cs_4PbBr_6 has been extensively studied for its strong and stable green PL [102–104], but extensive scientific debate has led to the conclusion that pure Cs_4PbBr_6 crystals do not exhibit PL at ambient conditions, and that the green emission is due to $CsPbBr_3$ inclusions [44,105]. This study confirms that pure colourless Cs_4PbBr_6 does not exhibit PL in the visible range at ambient conditions, and that previous reports of green emission were due to impurities, that consist in green and yellow crystals (see Figure 11).

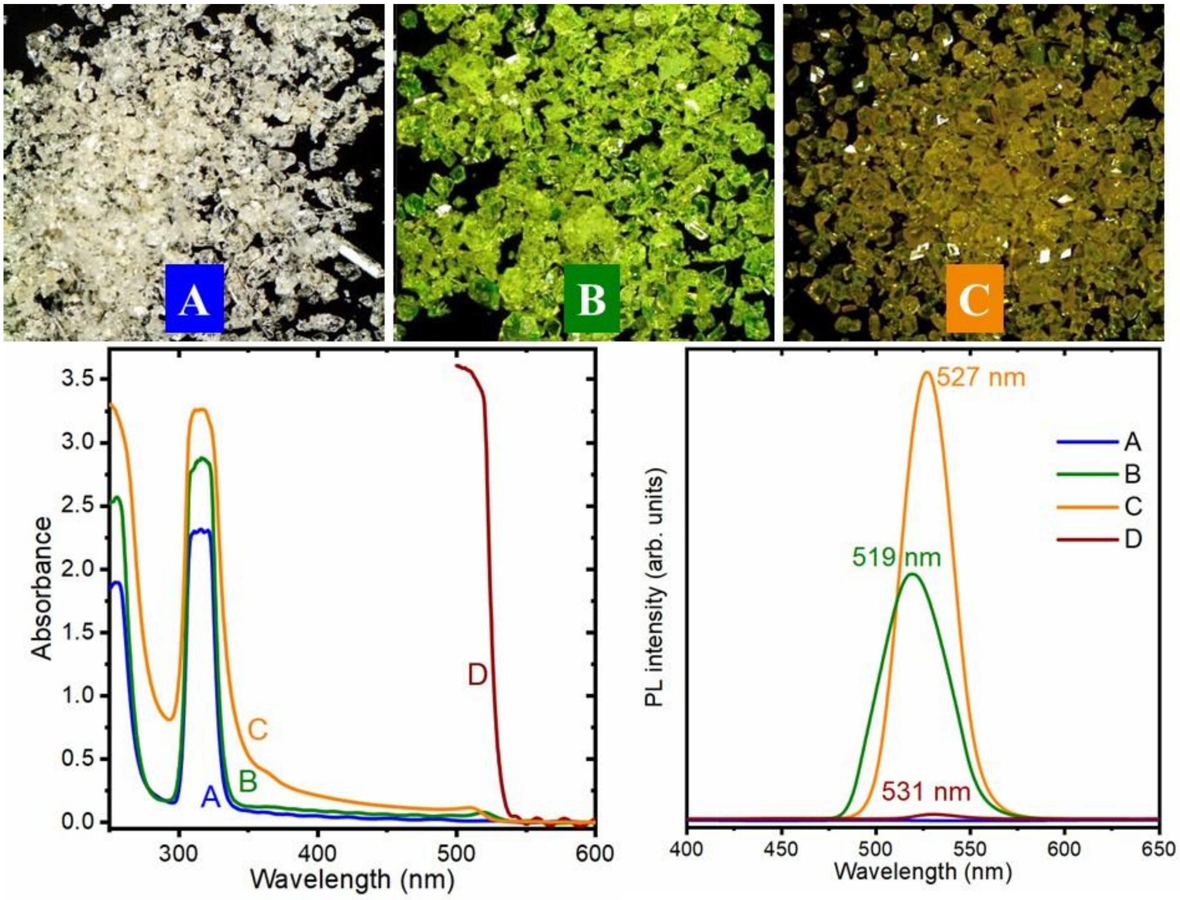

Figure 11. Comparison of the optical absorption and emission spectra of three types of Cs_4PbBr_6 crystals (A-colourless, B-green, C-yellow) with $CsPbBr_3$ (D) [101].

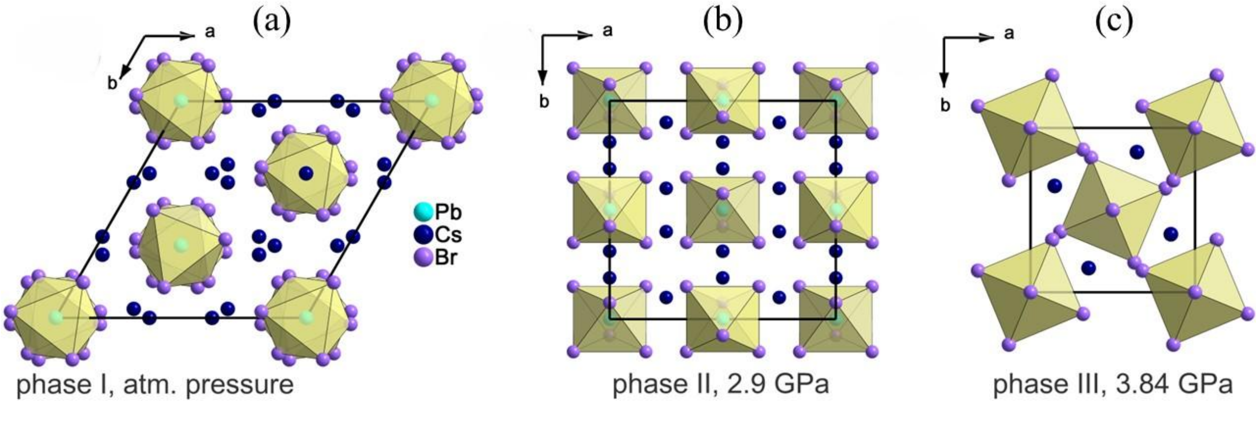

Figure 12. Crystal structures of Cs_4PbBr_6 at different pressures. (a) Phase I at atmospheric pressure, (b) phase II at 2.9 GPa, and (c) phase III at 3.84 GPa [101].

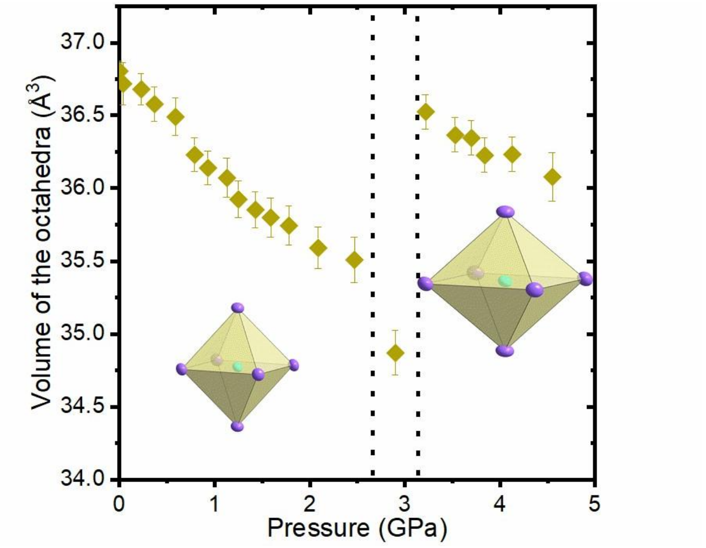

Figure 13. Pressure-induced changes in the volume of $PbBr_6$ octahedron [101].

The key finding of this work is the sequence of two pressure-induced first-order phase transitions. The first transition is observed at approximately 2.6 GPa, and the second at 3.2 GPa. The space group symmetry changes from the rhombohedral $R\bar{3}c$ (phase I) to the orthorhombic *Cmce* (intermediate phase II), and then to the tetragonal *P*4/*mnc* (high-pressure phase III), as shown in Figure 12. This sequence of phase transitions contradicts the reasons of the previously reported paper, where a single phase transition with the symmetry change from $R\bar{3}c$ to *B*2/*b* was reported on the basis of powder diffraction data [106] obtained under pressure in quasi-hydrostatic conditions. Our measurements were performed under genuinely hydrostatic conditions and excluded the influence of deviatoric stress in DAC. The structural motif of isolated $PbBr_6$ octahedra surrounded by Cs^+ cations is preserved in all phases, but their arrangement undergoes distinct changes (see Figure 13). Analysis of the volume-pressure data for phase I, fitted to the third-order Birch-Murnaghan equation of state, allowed us to determine the volume compressibility modulus B_0 = 10.5(7) GPa and its derivative B_0' = 9.7(16). These values are comparable to those of 2D $CsPb_2Br_5$ [95], indicating similar compressibility of both materials, which are significantly softer than 3D $CsPbBr_3$ [75]. For phase III, fitting the data to the second-order equation of state gave B_0 = 13.1(9) GPa, which is slightly higher than in phase I. The crystal compressibility in phase I is nearly isotropic, with a small difference along the *c* axis compared to the *a*-*b* plane, but the anisotropy clearly increases in phase III. However, one of the most intriguing findings is the pressure-induced increase in the volume of $PbBr_6$ octahedra by more than 5% at the transition to the tetragonal phase (phase III). This phenomenon contrasts with the reduction in the unit cell volume and the behaviour of other structural parameters, which show a typical pressure dependence. In phase I, at atmospheric pressure, $PbBr_6$ octahedra are regular, with Pb–Br bonds of 3.022(1) Å. Under pressure, these bonds gradually contract to 2.5 GPa, after which their lengths differentiate in phase II (two longer and four shorter bonds). However, the transition to phase III is associated with an unusual deformation of the octahedra: the four equatorial bonds elongate to 3.061(1) Å (exceeding the bond lengths at atmospheric pressure), while the two axial bonds contract to 2.923(1) Å. We attribute this unusual deformation of the octahedra, which cannot be rationally explained only by pressure-induced structural changes, to an electronically driven geometric distortion known as the pseudo-Jahn-Teller effect (PJTE). Given that the electronic configuration of Pb^{2+} has closed subshells and therefore its ground state is nondegenerate, the PJTE seems to be the only possible explanation. The strong deformation of the $PbBr_6$ octahedra is most likely responsible for the tetragonal arrangement of the crystal structure, and therefore the increase in symmetry in high-pressure phase III can be also attributed to the pressure-induced PJTE.

The optical properties of pure Cs_4PbBr_6 under pressure have also been studied in detail. The absorption edge was found to redshift with increasing pressure, indicating a narrowing of the energy gap. The sharp and well-separated excitonic band at around 315 nm broadens slightly with pressure in phase I, and its width increases dramatically at the transition to phase II, which can be attributed to the differentiation of the Pb–Br bond lengths. Then, the excitonic band splits into two components at the crystal transition to the tetragonal phase III. This splitting corresponds to the massive geometric distortion of the $PbBr_6$ octahedra and also confirms the pressure-induced PJTE in Cs_4PbBr_6. The pressure dependence of the energy gap is characterized by two step changes at 2.6 GPa and 3.2 GPa, which correlates excellently with the phase transitions observed in X-ray studies. The overall narrowing of the energy gap over the entire pressure range studied, up to 4.2 GPa, is greater than 0.51 eV. Electronic band structure calculations, performed by the first-principles method using pressure-dependent structural data, perfectly reproduced the experimental pressure dependence of the energy gap, including jumpwise changes at the transition points. These first-principles calculations were performed by dr hab. Konrad J. Kapcia, prof. UAM of the Faculty of Physics and Astronomy, Adam Mickiewicz University. High-pressure PL experiments on pure Cs_4PbBr_6, performed with excitation in the range of 250–320 nm, revealed the appearance of a broad emission band extending from 400 to 800 nm. This emission, centered at 575 nm, occurs only after the material transition to phase III, above 3.2 GPa. Unlike some layered perovskites, where the emission is enhanced by octahedra tilting, in the case of Cs_4PbBr_6 the white PL is clearly caused by octahedra distortion resulting from the PJTE effect.

In summary, this study explains the behaviour of Cs_4PbBr_6 under pressure. The sequence of two phase transitions ($R\bar{3}c \rightarrow Cmce \rightarrow P4/mnc$) was revealed, correcting earlier reports. Most importantly, an unprecedented volume increase of $PbBr_6$ octahedra in high-pressure phase III is identified and described in detail. Pressure-induced white-light emission from Cs_4PbBr_6 has been associated with pseudo-Jahn-Teller distortions, demonstrating how external pressure can activate or enhance phenomena linked to intrinsic lattice dynamics. This study also highlights the crucial importance of using appropriate structural models and accurate experimental data for the correct interpretation of material properties and provides a solid foundation for further research on zero-dimensional perovskites and their potential optoelectronic applications.

Table 2. Selected properties of pure Cs_4PbBr_6.

Parameter	*Value/description*
Thermodynamic stability	
Thermal stability range	at least 100 K – 800 K

Melting temperature	~800 K
Pressure-induced phase transitions	
Crystal system, space group, phase I	rhombohedral, $R\bar{3}c$
First phase transition pressure	~2.6 GPa
Crystal system, space group, phase II	orthorhombic, *Cmce*
Second phase transition pressure	~3.2 GPa
Crystal system, space group, phase III	tetragonal, *P*4/*mnc*
Compressibility	
Bulk modulus (B_0), phase I	10.5(7) GPa
Derivative of bulk modulus (B_0'), phase I	9.7(16)
Bulk modulus (B_0), phase III	13.1(9) GPa
Optical properties	
Excitonic absorption band, atmospheric pressure	~315 nm
Calculated energy band gap, atmospheric pressure	3.87 eV
Band gap type, phase I	direct
Band gap type, phase II & III	indirect
Total band gap reduction under pressure (up to 4.2 GPa)	~0.5 eV
Photoluminescence appearance	>3.2 GPa
Emission band characteristics	broad (400-800 nm), centered at 575 nm, asymmetric

3. *Effect of pressure and temperature on the structure and optical properties of two-dimensional lead iodide perovskites* [107]

This work focuses on the study of the influence of pressure and temperature on two lead iodide perovskites with 2D architectures, $[C(NH_2)_3]_2PbI_4$ and $CsC[(NH_2)_3]PbI_4$. The inorganic framework of $[C(NH_2)_3]_2PbI_4$ is formed of corner-sharing PbI_6 octahedra, which are arranged in double perovskite layers. A characteristic feature of this framework is the absence of every second octahedra in these layers. As shown in Figure 14a, the voids created by this arrangement, as well as the regions between the inorganic layers, are occupied by guanidinium cations, which act as barriers for charge carriers. Under ambient conditions, this material is characterized by a yellow colour. The properties of the 2D perovskite materials can be modified by the introduction of mixed cations. For this purpose, the compound $CsC[(NH_2)_3]PbI_4$ was crystallized by incorporating both inorganic and organic ions. The structure of this material is characterized by single layers of PbI_6 octahedra connected in a plane by shared corners, and two different ordered cations alternatively occupying the space between the layers (see Figure 14b). The octahedra are tilted to each other in an antiphase manner (in opposite directions) along the *c* direction, creating Pb-I-Pb alternative angles of 110 or 65 degrees. These specific tilts create a system of large and small voids between the layers. The large voids are occupied by the guanidinium ions, and the smaller ones by the cesium ions. The change in octahedral connectivity in $CsC(NH_2)_3PbI_4$, compared to $[C(NH_2)_3]_2PbI_4$, significantly affects the overlap of the lead and iodine orbitals. This affects the absorption edge and as a result the crystals are red in colour. Both of these 2D perovskites can be considered as naturally highly confined quantum systems. Their band structure is highly sensitive to changes in atomic arrangements, which can be precisely manipulated by pressure and temperature. Complementary set of experimental techniques was used to characterize the structural and optical responses of both perovskite materials under varying thermodynamic conditions.

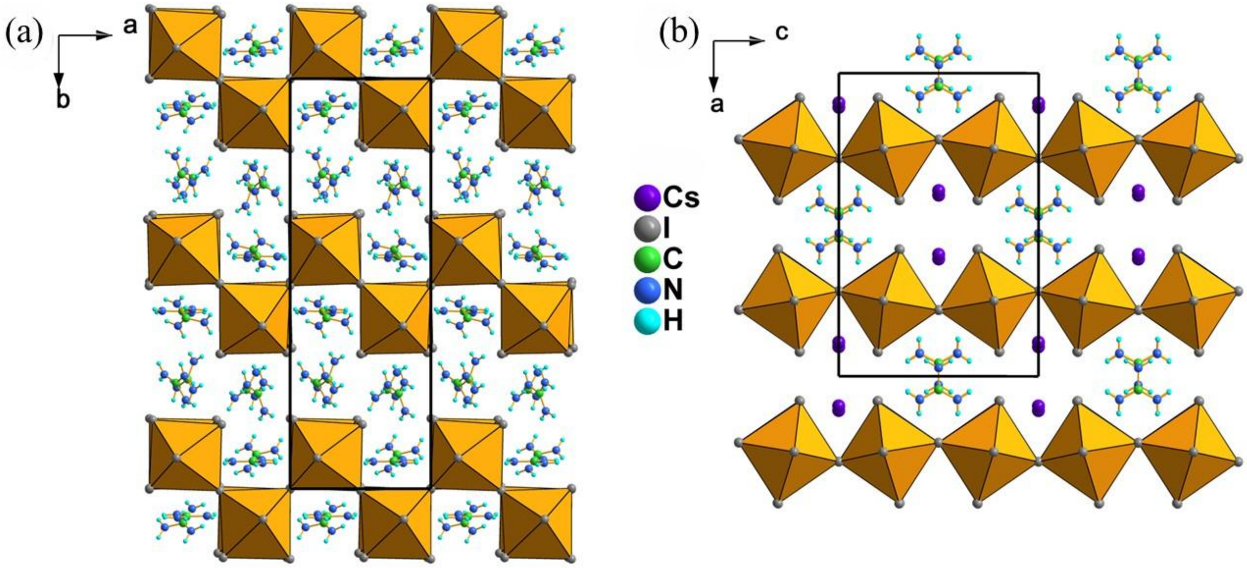

Figure 14. Room-temperature crystal structures of (a) $[C(NH_2)_3]_2PbI_4$, and (b) $CsC[(NH_2)_3]PbI_4$ [107].

Previous studies have shown that $[C(NH_2)_3]_2PbI_4$ undergoes two second-order phase transitions at temperatures T_1 = 356 K and T_2 = 307 K [108]. The high-temperature phase I of the space group *Pmna* transforms to the intermediate phase II of the space group *Pnnm*, and then the crystal enters the low-temperature phase III of the space group $P2_1/n$. However, there have been no reports so far on how the optical properties of this material evolve with temperature. In this work, we examined the temperature-dependent behaviour of the energy gap of a single-crystal sample over a broad temperature range (88–423 K). The measurement showed a gradual decrease in the energy gap with increasing temperature. The phase transitions at T_1 and T_2 caused only small deviations from this dependence. In addition, high-pressure optical measurements were performed. The energy gap experiences a sharp decrease as the crystal undergoes a phase transformation from phase III to the high-pressure phase IV ($P\bar{1}$). This transition is observed at approximately 0.5 GPa at room temperature. Further compression of the crystal to 4.5 GPa results in a continuous decrease in the energy gap. The overall energy gap narrowing in the whole pressure range studied was of approximately 0.2 eV. The high-pressure SCXRD measurements show abrupt changes in the lattice parameters and volume at 0.5 GPa (see Figure 15), confirming that the transition is of first-order type. The observed transition is consistent with predictions from previous differential thermal analysis (DTA) measurements [108], which suggested a phase boundary in the pressure-

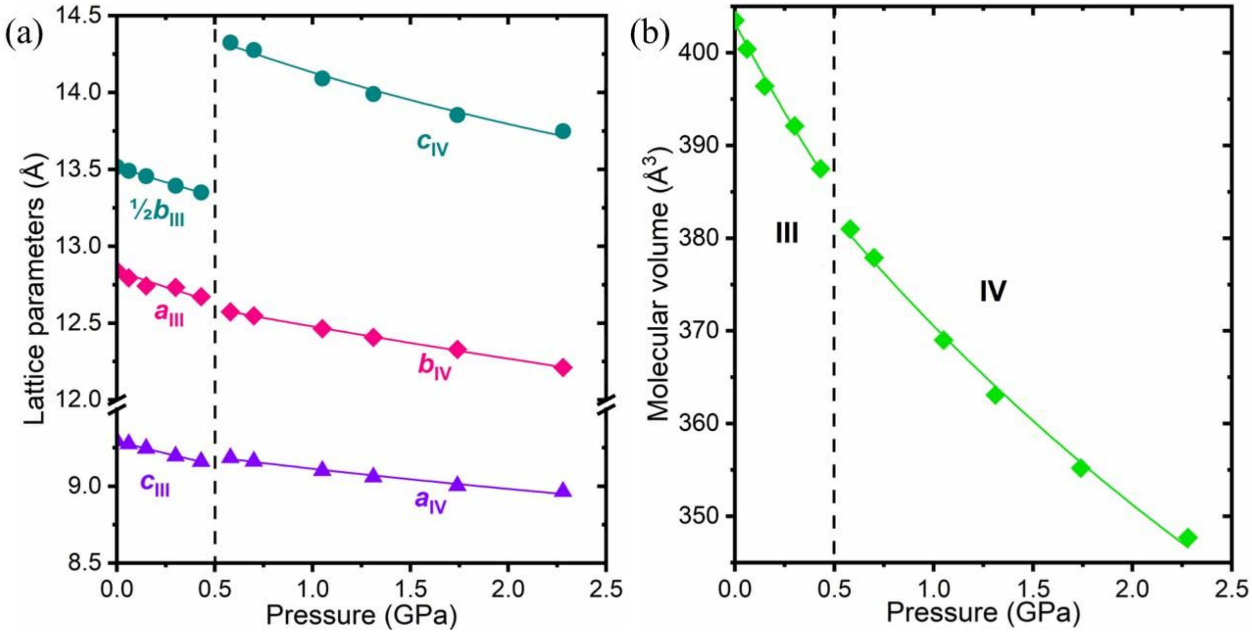

Figure 15. Pressure dependence of (a) the unit cell dimensions and (b) molecular volume of $[C(NH_2)_3]_2PbI_4$ [107].

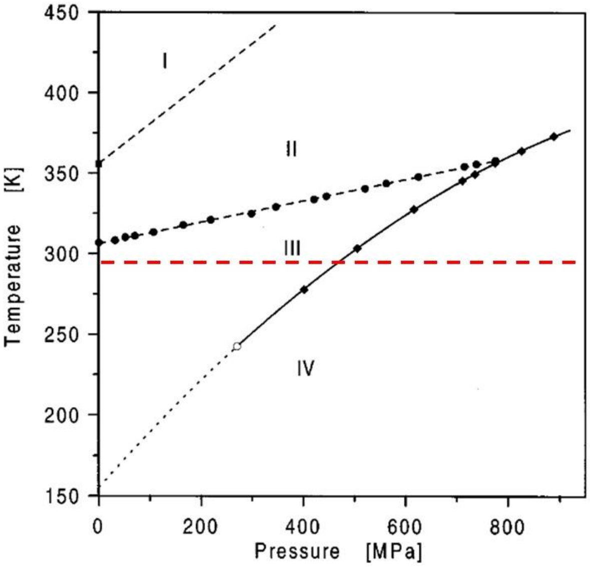

Figure 16. Phase diagram of $[C(NH_2)_3]_2PbI_4$ [108]. Red dashed line represents the experimental high-pressure path followed in this study at room temperature.

temperature phase diagram near this value at room temperature. Our experimental findings provide the first confirmation of this predicted phase boundary. The p-T phase diagram of $[C(NH_2)_3]_2PbI_4$ is shown in Figure 16. The second-order Birch-Murnaghan equation of state was fitted to the experimental data $V(p)$ and showed that high-pressure phase IV is less compressible (B_0 = 13.0(7) GPa) than phase III (B_0 = 9.8(10) GPa). Structural changes include shortening of the Pb–I bonds, reducing the distortion of the octahedra, and straightening of the Pb–I–Pb angles, which is the main mechanism for narrowing the energy gap. A surprising compressibility anisotropy was also observed, the direction perpendicular to the layers is stiffer than the directions in the plane of the layers. This contrast with the typical behaviour of layered materials, where weak interlayer interactions usually result in greater compressibility along the out-of-plane direction.

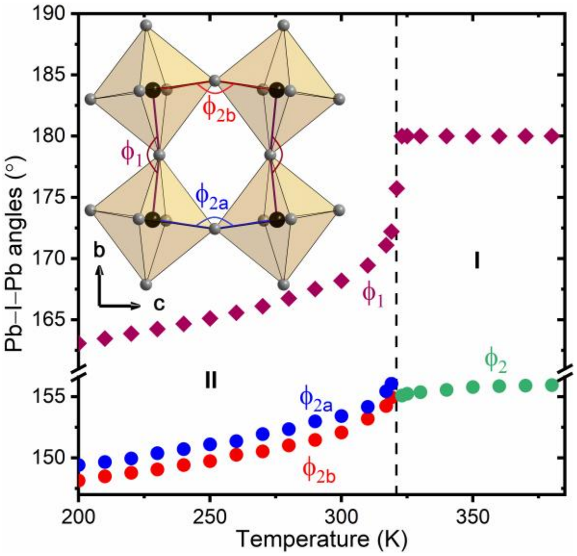

Figure 17. Temperature dependences of the Pb–I–Pb angles of the $CsC[(NH_2)_3]PbI_4$ [107].

DSC measurements of $CsC[(NH_2)_3]PbI_4$ revealed a second-order phase transition at 320.8 K, which had not been previously reported. This thermal anomaly was later validated by temperature-dependent SCXRD, performed in the 200–380 K range. While the structure of this compound was previously reported by Nazarenko et al. [80], our study re-examined its temperature-dependent structural evolution to provide a more detailed understanding. Continuous changes in the lattice parameters and unit cell volume were observed around 321 K. Our structural refinements confirmed that the iodine atoms, which bridge the PbI_6 octahedra along the *c*-axis, are ordered at room temperature, with indications of becoming disordered only as the sample approaches the phase transition point. SCXRD measurements were also used to study the thermal expansion in detail. In phase II (space group *Pnnm*), the lattice parameters *b* and *c* expand with increasing temperature, while, the parameter *a* exhibits a distinct contraction. This is manifested by a significant negative thermal expansion along the axis *a*, with thermal expansion coefficients reaching the values of the order of -10^{-4} K^{-1} as the temperature approaches the transition point. The temperature dependence of the Pb–I–Pb angles, ϕ_1 and ϕ_2, is plotted in Figure 17. As the temperature increases, the gradual straightening of the PbI_6 octahedra leads to the disappearance of the alternating tilts. This causes a halving of the lattice parameter *b* and results in the crystal adopting the higher symmetry space group *Imma* in phase I, above 321 K. In phase I, the iodine atoms bridging the octahedra along the *c*-axis become disordered, occupying two distinct positions with equal occupancy factors. This order-disorder behaviour is consistent with the observed increase in entropy during the transition. The negative thermal expansion along the *a*-axis changes to positive upon transition to phase I.

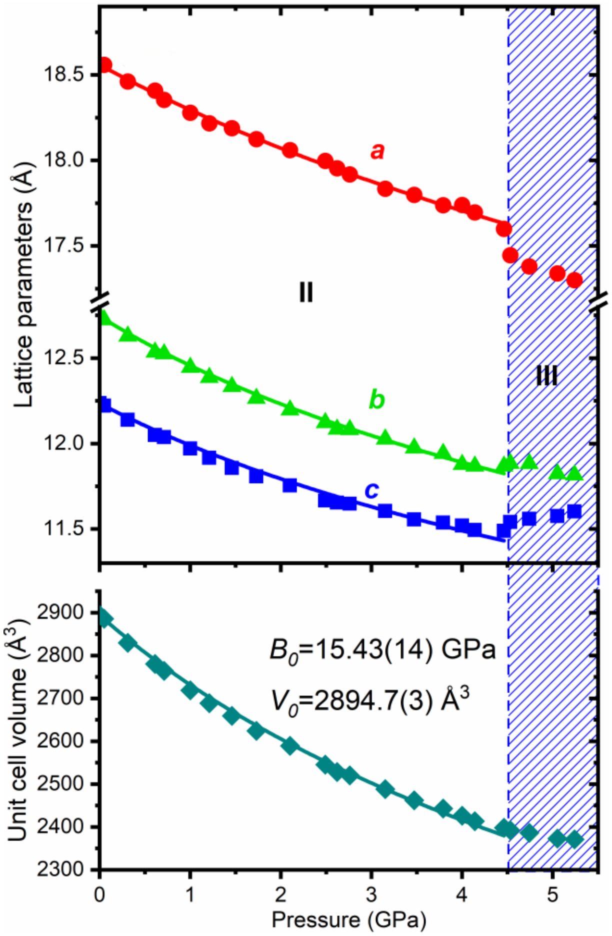

Figure 18. The unit-cell volume and lattice parameters of $CsC[(NH_2)_3]PbI_4$ as a function of pressure [107].

Absorption spectra measurements of a single-crystal plate as a function of temperature showed nonlinear energy band gap narrowing in phase II until the phase transition. This decrease in energy band gap is directly attributed to the straightening of the Pb–I–Pb angles, which increases the overlap between the Pb and I atomic orbitals, which are crucial for electronic transitions near the absorption edge. Above the phase I transition temperature, the temperature-induced changes in energy band gap are smaller and exhibit a linear relationship. The continuous changes in energy band gap confirm the second-order nature of the transition. Furthermore, the optical properties of $CsC[(NH_2)_3]PbI_4$ were measured as a function of pressure up to 5.45 GPa. In the pressure range below 4.5 GPa, the absorption edge gradually red-shifts with increasing pressure. However, above 4.5 GPa a significant jumpwise redshift of the absorption edge was recorded. This behaviour corresponds to substantial reduction in the energy gap. In phase II, the energy gap narrowing is the result of the dominant effect of Pb–I bond shortening over the competing effect of Pb–I–Pb angle bending, while in phase III, this angle straightening further enhances this effect. The overall decrease in energy gap exceeds 12%, and it is accompanied by a distinct change in crystal colour. The pressure induced changes in energy gap were fully reversible, but a large pressure hysteresis was observed in the transition region, confirming the first-order character of the transition. High-pressure SCXRD experiments were performed in the pressure range up to 5.24 GPa. First-order phase transition of isostructural character (space group *Pnnm*) was revealed at approximately 4.5 GPa. This transition is accompanied by a reduction in the distortion of the PbI_6 octahedra. Figure 18 shows the pressure dependence of the unit-cell volume and lattice parameters. The bulk modulus B_0 for phase II, obtained by fitting the second-order Birch-Murnaghan equation of state to the experimental $V(p)$ data, was determined to be 15.4(2) GPa. This value is significantly higher than those determined for phases III and IV of $[C(NH_2)_3]_2PbI_4$, indicating that $CsC[(NH_2)_3]PbI_4$ is inherently less compressible. The material exhibits pronounced anisotropic compressibility, and similarly to $[C(NH_2)_3]_2PbI_4$ it is stiffer in the direction perpendicular to the inorganic layers. In phase III, anomalous negative compressibility was observed along the *c*-axis, probably related to the damping of vibrations of iodine atoms bridging the octahedra. Reducing the amplitude of these vibrations lead to an increase in the average bond length.

In summary, both the temperature increase and the hydrostatic compression lead to the band gap narrowing in the studied 2D perovskites, in contrast to 3D lead perovskites, where the opposite temperature trend is typically observed. This effect is closely related to modifications of the PbI_6 lattice geometry (bond shortening and octahedra rotation) and may be crucial for the design of materials with tunable optoelectronic properties for photovoltaic and optoelectronic applications.

Table 3. Selected properties of $[C(NH_2)_3]_2PbI_4$ and $CsC[(NH_2)_3]PbI_4$.

	$[C(NH_2)_3]_2PbI_4$	**$CsC[(NH_2)_3]PbI_4$**
Parameter	*Value/description*	
Phase transitions (temperature)	second-order transitions at 356 K and 307 K	second-order transition at 320.8 K
Phase transitions (pressure)	first-order transition at ~0.5 GPa	first-order transition at ~4.5 GPa
Crystal system, space group, phase I	orthorhombic, *Pmna*	orthorhombic, *Imma*
Crystal system, space group, phase II	orthorhombic, *Pnnm*	orthorhombic, *Pnnm*
Crystal system, space group, phase III	monoclinic, $P2_1/n$	orthorhombic, *Pnnm*
Crystal system, space group, phase IV	triclinic, $P\overline{1}$	–

Bulk modulus (B_0)	9.8(10) GPa (phase III) and 13.0(7) GPa (phase IV)	15.4(2) GPa (phase II)
Energy gap, atmospheric pressure	2.47 eV	2.22 eV
Total band gap reduction under pressure	~0.2 eV up to 4.5 GPa	~0.27 eV up to 5.5 GPa

V. Conclusions

In this thesis we systematically studied how hydrostatic pressure and temperature affect the structural and optical properties of selected low-dimensional metal-halide perovskites. Structure-property relationships were discussed across four materials: 2D $CsPb_2Br_5$, 0D Cs_4PbBr_6, and 2D guanidinium lead-iodide perovskites, $[C(NH_2)_3]_2PbI_4$ and $CsC(NH_2)_3PbI_4$. The main conclusions are summarized below.

- Pressure and temperature are effective tools for tuning electronic structure in low-dimensional perovskites. In the studied systems, compression systematically reduces interatomic distances and modifies octahedral tilts, producing progressive band-gap narrowing. Similarly, in the 2D iodides, temperature was used to achieve comparable band-gap tuning through the straightening of the angle between octahedra.
- Structural distortions of the lead-halide octahedra (tilting, rotation, and asymmetric deformation) are the origin of the observed optical responses. In all the systems studied, small changes in the Pb–X bond lengths and the Pb–X–Pb angles strongly alter orbitals overlap responsible for the absorption edge, and therefore the absorption and emission properties.
- The phase purity of the sample critically determines the measured optical characteristics. For $CsPb_2Br_5$, visible-range absorption and emission reported in some earlier studies were shown to arise from the 3D $CsPbBr_3$ microcrystals precipitated on the $CsPb_2Br_5$ plates. This underscores the need for accurate materials characterization and careful interpretation of the optical data.
- New pressure-driven phenomena were identified and explained for Cs_4PbBr_6. The crystal undergoes two first-order structural transitions (2.6 and 3.2 GPa) accompanied by abrupt band-gap reductions; the transition to the high-pressure tetragonal phase is marked by an unprecedented expansion of the $PbBr_6$ octahedra. This anomalous deformation is attributed to a pressure-activated pseudo-Jahn–Teller effect and is directly responsible for the emergence of broad band white-light photoluminescence. Such electronically driven geometrical instabilities provide a pathway for creating novel emissive states in materials that are non-emissive at ambient conditions.
- Layered guanidinium lead iodides display pronounced anisotropic mechanical responses, with the axis perpendicular to the inorganic layers significantly stiffer than the in-plane directions. In $CsC(NH_2)_3PbI_4$, we observed negative linear compressibility along one crystallographic direction, a rare response which is linked to changes in iodine atoms vibrational dynamics and octahedral tilts.
- The results obtained emphasize the importance of maintaining hydrostatic conditions, combining single-crystal diffraction with optical measurements, and using structural models derived from high-quality SCXRD data for reliable theoretical interpretation.

Misassignment symmetry of high-pressure phases or the use of nonhydrostatic media can lead to incorrect conclusions about electronic structure and optical behaviour.

- The demonstrated ability to controllably tune band gaps and activate emissive states via pressure-induced octahedral distortions has immediate implications for the design of pressure- or temperature-responsive optoelectronic devices and sensors. More broadly, the findings contribute to the understanding of how structural features, compositional variations, and environmental factors interact, which is essential for the advanced perovskite technologies in photovoltaics, lighting, and sensing.

References

[1] Z.-K. Tan, R.S. Moghaddam, M.L. Lai, P. Docampo, R. Higler, F. Deschler, M. Price, A. Sadhanala, L.M. Pazos, D. Credgington, F. Hanusch, T. Bein, H.J. Snaith, R.H. Friend, Bright Light-Emitting Diodes Based on Organometal Halide Perovskite, *Nat. Nanotechnol.* 9 (2014) 687–692. https://doi.org/10.1038/nnano.2014.149.

[2] S. De Wolf, J. Holovsky, S.-J. Moon, P. Löper, B. Niesen, M. Ledinsky, F.-J. Haug, J.-H. Yum, C. Ballif, Organometallic Halide Perovskites: Sharp Optical Absorption Edge and Its Relation to Photovoltaic Performance, *J. Phys. Chem. Lett.* 5 (2014) 1035–1039. https://doi.org/10.1021/jz500279b.

[3] J. Berry, T. Buonassisi, D.A. Egger, G. Hodes, L. Kronik, Y. Loo, I. Lubomirsky, S.R. Marder, Y. Mastai, J.S. Miller, D.B. Mitzi, Y. Paz, A.M. Rappe, I. Riess, B. Rybtchinski, O. Stafsudd, V. Stevanovic, M.F. Toney, D. Zitoun, A. Kahn, D. Ginley, D. Cahen, Hybrid Organic–Inorganic Perovskites (HOIPs): Opportunities and Challenges, *Adv. Mater.* 27 (2015) 5102–5112. https://doi.org/10.1002/adma.201502294.

[4] S.D. Stranks, H.J. Snaith, Metal-Halide Perovskites for Photovoltaic and Light-Emitting Devices, *Nat. Nanotechnol.* 10 (2015) 391–402. https://doi.org/10.1038/nnano.2015.90.

[5] B. Saparov, D.B. Mitzi, Organic–Inorganic Perovskites: Structural Versatility for Functional Materials Design, *Chem. Rev.* 116 (2016) 4558–4596. https://doi.org/10.1021/acs.chemrev.5b00715.

[6] J.S. Manser, J.A. Christians, P. V. Kamat, Intriguing Optoelectronic Properties of Metal Halide Perovskites, *Chem. Rev.* 116 (2016) 12956–13008. https://doi.org/10.1021/acs.chemrev.6b00136.

[7] P. Tonui, S.O. Oseni, G. Sharma, Q. Yan, G. Tessema Mola, Perovskites Photovoltaic Solar Cells: An Overview of Current Status, *Renew. Sustain. Energy Rev.* 91 (2018) 1025–1044. https://doi.org/10.1016/j.rser.2018.04.069.

[8] A. Kojima, K. Teshima, Y. Shirai, T. Miyasaka, Organometal Halide Perovskites as Visible-Light Sensitizers for Photovoltaic Cells, *J. Am. Chem. Soc.* 131 (2009) 6050–6051. https://doi.org/10.1021/ja809598r.

[9] H.-S. Kim, C.-R. Lee, J.-H. Im, K.-B. Lee, T. Moehl, A. Marchioro, S.-J. Moon, R. Humphry-Baker, J.-H. Yum, J.E. Moser, M. Grätzel, N.-G. Park, Lead Iodide Perovskite Sensitized All-Solid-State Submicron Thin Film Mesoscopic Solar Cell with Efficiency Exceeding 9%, *Sci. Rep.* 2 (2012) 591. https://doi.org/10.1038/srep00591.

[10] M.M. Lee, J. Teuscher, T. Miyasaka, T.N. Murakami, H.J. Snaith, Efficient Hybrid Solar Cells Based on Meso-Superstructured Organometal Halide Perovskites, *Science* 338 (2012) 643–647. https://doi.org/10.1126/science.1228604.

[11] J.H. Heo, S.H. Im, J.H. Noh, T.N. Mandal, C.-S. Lim, J.A. Chang, Y.H. Lee, H. Kim, A. Sarkar, Md.K. Nazeeruddin, M. Grätzel, S. Il Seok, Efficient Inorganic–Organic Hybrid Heterojunction Solar Cells Containing Perovskite Compound and Polymeric Hole Conductors, *Nat. Photonics* 7 (2013) 486–491. https://doi.org/10.1038/nphoton.2013.80.

[12] J. Burschka, N. Pellet, S.-J. Moon, R. Humphry-Baker, P. Gao, M.K. Nazeeruddin, M. Grätzel, Sequential Deposition as A Route to High-Performance Perovskite-Sensitized Solar Cells, *Nature* 499 (2013) 316–319. https://doi.org/10.1038/nature12340.

[13] M. Liu, M.B. Johnston, H.J. Snaith, Efficient Planar Heterojunction Perovskite Solar Cells by Vapour Deposition, *Nature* 501 (2013) 395–398. https://doi.org/10.1038/nature12509.

[14] H.J. Snaith, Perovskites: The Emergence of a New Era for Low-Cost, High-Efficiency Solar Cells, *J. Phys. Chem. Lett.* 4 (2013) 3623–3630. https://doi.org/10.1021/jz4020162.

[15] C.C. Stoumpos, C.D. Malliakas, M.G. Kanatzidis, Semiconducting Tin and Lead Iodide Perovskites with Organic Cations: Phase Transitions, High Mobilities, and Near-Infrared Photoluminescent Properties, *Inorg. Chem.* 52 (2013) 9019–9038. https://doi.org/10.1021/ic401215x.

[16] H. Zhou, Q. Chen, G. Li, S. Luo, T. Song, H.-S. Duan, Z. Hong, J. You, Y. Liu, Y. Yang, Interface Engineering of Highly Efficient Perovskite Solar Cells, *Science* 345 (2014) 542–546. https://doi.org/10.1126/science.1254050.

[17] N.J. Jeon, J.H. Noh, Y.C. Kim, W.S. Yang, S. Ryu, S. Il Seok, Solvent Engineering for High-Performance Inorganic–Organic Hybrid Perovskite Solar Cells, *Nat. Mater.* 13 (2014) 897–903. https://doi.org/10.1038/nmat4014.

[18] W.S. Yang, J.H. Noh, N.J. Jeon, Y.C. Kim, S. Ryu, J. Seo, S. Il Seok, High-Performance Photovoltaic Perovskite Layers Fabricated Through Intramolecular Exchange, *Science* 348 (2015) 1234–1237. https://doi.org/10.1126/science.aaa9272.

[19] P. Calado, A.M. Telford, D. Bryant, X. Li, J. Nelson, B.C. O'Regan, P.R.F. Barnes, Evidence for Ion Migration in Hybrid Perovskite Solar Cells with Minimal Hysteresis, *Nat. Commun.* 7 (2016) 13831. https://doi.org/10.1038/ncomms13831.

[20] Y.G. Kim, K.C. Kwon, Q. Van Le, K. Hong, H.W. Jang, S.Y. Kim, Atomically Thin Two-Dimensional Materials as Hole Extraction Layers in Organolead Halide Perovskite Photovoltaic Cells, *J. Power Sources* 319 (2016) 1–8. https://doi.org/10.1016/j.jpowsour.2016.04.032.

[21] Z. Li, M. Yang, J.-S. Park, S.-H. Wei, J.J. Berry, K. Zhu, Stabilizing Perovskite Structures by Tuning Tolerance Factor: Formation of Formamidinium and Cesium Lead Iodide Solid-State Alloys, *Chem. Mater.* 28 (2016) 284–292. https://doi.org/10.1021/acs.chemmater.5b04107.

[22] A.M. Glazer, The Classification of Tilted Octahedra in Perovskites, *Acta Crystallogr. B* 28 (1972) 3384–3392. https://doi.org/10.1107/S0567740872007976.

[23] R.J.D. Tilley, Perovskites, *Wiley*, 2016. https://doi.org/10.1002/9781118935651.

[24] A. Jaffe, Y. Lin, H.I. Karunadasa, Halide Perovskites under Pressure: Accessing New Properties through Lattice Compression, *ACS Energy Lett.* 2 (2017) 1549–1555. https://doi.org/10.1021/acsenergylett.7b00284.

[25] M. Li, T. Liu, Y. Wang, W. Yang, X. Lü, Pressure Responses of Halide Perovskites with Various Compositions, Dimensionalities, and Morphologies, *Matter Radiat. Extrem.* 5 (2020). https://doi.org/10.1063/1.5133653.

[26] E.M. Mozur, J.R. Neilson, Cation Dynamics in Hybrid Halide Perovskites, *Annu. Rev. Mater. Res.* 51 (2021) 269–291. https://doi.org/10.1146/annurev-matsci-080819-012808.

[27] F. Brivio, J.M. Frost, J.M. Skelton, A.J. Jackson, O.J. Weber, M.T. Weller, A.R. Goñi, A.M.A. Leguy, P.R.F. Barnes, A. Walsh, Lattice Dynamics and Vibrational Spectra of The Orthorhombic, Tetragonal, and Cubic Phases of Methylammonium Lead Iodide, *Phys. Rev. B* 92 (2015) 144308. https://doi.org/10.1103/PhysRevB.92.144308.

[28] M. Pitaro, E.K. Tekelenburg, S. Shao, M.A. Loi, Tin Halide Perovskites: From Fundamental Properties to Solar Cells, *Adv. Mater.* 34 (2022). https://doi.org/10.1002/adma.202105844.

[29] L.M. Farigliano, F. Negreiros Ribeiro, G.M. Dalpian, Phase Transitions in $CsPbBr_3$: Evaluating Perovskite Behavior Over Different Time Scales, *Mater. Adv.* 5 (2024) 5794–5801. https://doi.org/10.1039/D4MA00216D.

[30] J. Yi, X. Ge, E. Liu, T. Cai, C. Zhao, S. Wen, H. Sanabria, O. Chen, A.M. Rao, J. Gao, The Correlation Between Phase Transition and Photoluminescence Properties of $CsPbX_3$ (X = Cl, Br, I) Perovskite Nanocrystals, *Nanoscale Adv.* 2 (2020) 4390–4394. https://doi.org/10.1039/D0NA00545B.

[31] L. Gigli, M. Veit, M. Kotiuga, G. Pizzi, N. Marzari, M. Ceriotti, Thermodynamics and Dielectric Response of BaTiO3 by Data-Driven Modeling, *NPJ Comput. Mater.* 8 (2022) 209. https://doi.org/10.1038/s41524-022-00845-0.

[32] M. Mączka, M. Ptak, A. Gągor, J.K. Zaręba, X. Liang, S. Balčiūnas, O.A. Semenikhin, O.I. Kucheriv, I.A. Gural'skiy, S. Shova, A. Walsh, J. Banys, M. Šimėnas, Phase Transitions, Dielectric Response, and Nonlinear Optical Properties of Aziridinium Lead Halide Perovskites, *Chem. Mater.* 35 (2023) 9725–9738. https://doi.org/10.1021/acs.chemmater.3c02200.

[33] A. Amat, E. Mosconi, E. Ronca, C. Quarti, P. Umari, Md.K. Nazeeruddin, M. Grätzel, F. De Angelis, Cation-Induced Band-Gap Tuning in Organohalide Perovskites: Interplay of Spin–Orbit Coupling and Octahedra Tilting, *Nano Lett.* 14 (2014) 3608–3616. https://doi.org/10.1021/nl5012992.

[34] C. Motta, F. El-Mellouhi, S. Kais, N. Tabet, F. Alharbi, S. Sanvito, Revealing the Role of Organic Cations in Hybrid Halide Perovskite $CH_3NH_3PbI_3$, *Nat. Commun.* 6 (2015) 7026. https://doi.org/10.1038/ncomms8026.

[35] M. Mittal, A. Jana, S. Sarkar, P. Mahadevan, S. Sapra, Size of the Organic Cation Tunes the Band Gap of Colloidal Organolead Bromide Perovskite Nanocrystals, *J. Phys. Chem. Lett.* 7 (2016) 3270–3277. https://doi.org/10.1021/acs.jpclett.6b01406.

[36] M.C. Weidman, M. Seitz, S.D. Stranks, W.A. Tisdale, Highly Tunable Colloidal Perovskite Nanoplatelets through Variable Cation, Metal, and Halide Composition, *ACS Nano* 10 (2016) 7830–7839. https://doi.org/10.1021/acsnano.6b03496.

[37] M.E. Kamminga, H.-H. Fang, M.R. Filip, F. Giustino, J. Baas, G.R. Blake, M.A. Loi, T.T.M. Palstra, Confinement Effects in Low-Dimensional Lead Iodide Perovskite Hybrids, *Chem. Mater.* 28 (2016) 4554–4562. https://doi.org/10.1021/acs.chemmater.6b00809.

[38] Y. Chen, Y. Sun, J. Peng, J. Tang, K. Zheng, Z. Liang, 2D Ruddlesden–Popper Perovskites for Optoelectronics, *Adv. Mater.* 30 (2018). https://doi.org/10.1002/adma.201703487.

[39] C.C. Stoumpos, L. Mao, C.D. Malliakas, M.G. Kanatzidis, Structure–Band Gap Relationships in Hexagonal Polytypes and Low-Dimensional Structures of Hybrid Tin Iodide Perovskites, *Inorg. Chem.* 56 (2017) 56–73. https://doi.org/10.1021/acs.inorgchem.6b02764.

[40] Z. Yuan, C. Zhou, Y. Tian, Y. Shu, J. Messier, J.C. Wang, L.J. van de Burgt, K. Kountouriotis, Y. Xin, E. Holt, K. Schanze, R. Clark, T. Siegrist, B. Ma, One-Dimensional Organic Lead Halide Perovskites with Efficient Bluish White-Light Emission, *Nat. Commun.* 8 (2017) 14051. https://doi.org/10.1038/ncomms14051.

[41] H. Lin, C. Zhou, Y. Tian, T. Siegrist, B. Ma, Low-Dimensional Organometal Halide Perovskites, *ACS Energy Lett.* 3 (2018) 54–62. https://doi.org/10.1021/acsenergylett.7b00926.

[42] T.-M.H. Duong, S. Nobusue, H. Tada, Preparation of Perovskite-Derived One Dimensional Single Crystals Based on Edge-Shared Octahedrons with Pyridine Derivatives, *J. Cryst. Growth* 537 (2020) 125577. https://doi.org/10.1016/j.jcrysgro.2020.125577.

[43] Y. Zhang, M.I. Saidaminov, I. Dursun, H. Yang, B. Murali, E. Alarousu, E. Yengel, B.A. Alshankiti, O.M. Bakr, O.F. Mohammed, Zero-Dimensional Cs_4PbBr_6 Perovskite Nanocrystals, *J. Phys. Chem. Lett.* 8 (2017) 961–965. https://doi.org/10.1021/acs.jpclett.7b00105.

[44] Q.A. Akkerman, A.L. Abdelhady, L. Manna, Zero-Dimensional Cesium Lead Halides: History, Properties, and Challenges, *J. Phys. Chem. Lett.* 9 (2018) 2326–2337. https://doi.org/10.1021/acs.jpclett.8b00572.

[45] M. Cao, Y. Damji, C. Zhang, L. Wu, Q. Zhong, P. Li, D. Yang, Y. Xu, Q. Zhang, Low-Dimensional-Networked Cesium Lead Halide Perovskites: Properties, Fabrication, and Applications, *Small Methods* 4 (2020). https://doi.org/10.1002/smtd.202000303.

[46] I.C. Smith, E.T. Hoke, D. Solis-Ibarra, M.D. McGehee, H.I. Karunadasa, A Layered Hybrid Perovskite Solar-Cell Absorber with Enhanced Moisture Stability, *Angew. Chem. Int. Ed.* 53 (2014) 11232–11235. https://doi.org/10.1002/anie.201406466.

[47] S. Ramakrishnan, B. Chen, X. Zhang, Y. Xie, X. Tong, Y. Xu, A.N. Alphenaar, A. Ruthen, A.J. Babatunde, Y. Zhang, M. Cotlet, D.B. Mitzi, Q. Yu, Phase-Stabilized 2D/3D Hetero-Bilayers via Lattice Matching for Efficient and Stable Inverted Solar Cells, *Joule* 9 (2025) 101954. https://doi.org/10.1016/j.joule.2025.101954.

[48] Y. Zhang, J. Liu, Z. Wang, Y. Xue, Q. Ou, L. Polavarapu, J. Zheng, X. Qi, Q. Bao, Synthesis, Properties, and Optical Applications of Low-Dimensional Perovskites, *Chem. Comm.* 52 (2016) 13637–13655. https://doi.org/10.1039/C6CC06425F.

[49] K. Hong, Q. Van Le, S.Y. Kim, H.W. Jang, Low-Dimensional Halide Perovskites: Review and Issues, *J. Mater. Chem. C* 6 (2018) 2189–2209. https://doi.org/10.1039/C7TC05658C.

[50] G. Wu, R. Liang, M. Ge, G. Sun, Y. Zhang, G. Xing, Surface Passivation Using 2D Perovskites toward Efficient and Stable Perovskite Solar Cells, *Adv. Mater.* 34 (2022). https://doi.org/10.1002/adma.202105635.

[51] Y. Shi, Z. Ma, D. Zhao, Y. Chen, Y. Cao, K. Wang, G. Xiao, B. Zou, Pressure-Induced Emission (PIE) of One-Dimensional Organic Tin Bromide Perovskites, *J. Am. Chem. Soc.* 141 (2019) 6504–6508. https://doi.org/10.1021/jacs.9b02568.

[52] S. Seth, A. Samanta, Photoluminescence of Zero-Dimensional Perovskites and Perovskite-Related Materials, *J. Phys. Chem. Lett.* 9 (2018) 176–183. https://doi.org/10.1021/acs.jpclett.7b02931.

[53] F. Brivio, A.B. Walker, A. Walsh, Structural and Electronic Properties of Hybrid Perovskites for High-Efficiency Thin-Film Photovoltaics from First-Principles, *APL Mater.* 1 (2013). https://doi.org/10.1063/1.4824147.

[54] L. Kong, G. Liu, J. Gong, Q. Hu, R.D. Schaller, P. Dera, D. Zhang, Z. Liu, W. Yang, K. Zhu, Y. Tang, C. Wang, S.-H. Wei, T. Xu, H. Mao, Simultaneous Band-Gap Narrowing and Carrier-Lifetime Prolongation of Organic–Inorganic Trihalide Perovskites, *Proc. Natl. Acad. Sci.* 113 (2016) 8910–8915. https://doi.org/10.1073/pnas.1609030113.

[55] R. Prasanna, A. Gold-Parker, T. Leijtens, B. Conings, A. Babayigit, H.-G. Boyen, M.F. Toney, M.D. McGehee, Band Gap Tuning via Lattice Contraction and Octahedral Tilting in Perovskite Materials for Photovoltaics, *J. Am. Chem. Soc.* 139 (2017) 11117–11124. https://doi.org/10.1021/jacs.7b04981.

[56] J.H. Noh, S.H. Im, J.H. Heo, T.N. Mandal, S. Il Seok, Chemical Management for Colorful, Efficient, and Stable Inorganic–Organic Hybrid Nanostructured Solar Cells, *Nano Lett.* 13 (2013) 1764–1769. https://doi.org/10.1021/nl400349b.

[57] G.E. Eperon, S.D. Stranks, C. Menelaou, M.B. Johnston, L.M. Herz, H.J. Snaith, Formamidinium Lead Trihalide: A Broadly Tunable Perovskite for Efficient Planar Heterojunction Solar Cells, *Energy Environ. Sci.* 7 (2014) 982. https://doi.org/10.1039/c3ee43822h.

[58] M.R. Filip, G.E. Eperon, H.J. Snaith, F. Giustino, Steric Engineering of Metal-Halide Perovskites with Tunable Optical Band Gaps, *Nat. Commun.* 5 (2014) 5757. https://doi.org/10.1038/ncomms6757.

[59] M.R. Filip, F. Giustino, Computational Screening of Homovalent Lead Substitution in Organic–Inorganic Halide Perovskites, *J. Phys. Chem. C* 120 (2016) 166–173. https://doi.org/10.1021/acs.jpcc.5b11845.

[60] S. Colella, E. Mosconi, P. Fedeli, A. Listorti, F. Gazza, F. Orlandi, P. Ferro, T. Besagni, A. Rizzo, G. Calestani, G. Gigli, F. De Angelis, R. Mosca, $MAPbI_{3-x}Cl_x$ Mixed Halide Perovskite for Hybrid Solar Cells: The Role of Chloride as Dopant on the Transport and Structural Properties, *Chem. Mater.* 25 (2013) 4613–4618. https://doi.org/10.1021/cm402919x.

[61] M. Szafrański, A. Katrusiak, Mechanism of Pressure-Induced Phase Transitions, Amorphization, and Absorption-Edge Shift in Photovoltaic Methylammonium Lead Iodide, *J. Phys. Chem. Lett.* 7 (2016) 3458–3466. https://doi.org/10.1021/acs.jpclett.6b01648.

[62] Al.L. Efros, M. Rosen, The Electronic Structure of Semiconductor Nanocrystals, *Annu. Rev. Mater. Sci.* 30 (2000) 475–521. https://doi.org/10.1146/annurev.matsci.30.1.475.

[63] T.M. Weeraddana, S.M. Premathilaka, Y. Tang, A.D. Antu, A. Roach, J. Yang, L. Sun, Dielectrically Confined Stable Excitons in Few-Atom-Thick PbS Nanosheets, *J. Phys. Chem. Lett.* 13 (2022) 7756–7761. https://doi.org/10.1021/acs.jpclett.2c02254.

[64] T. Ishihara, J. Takahashi, T. Goto, Optical Properties Due to Electronic Transitions in Two-Dimensional Semiconductors $(C_nH_{2n+1}NH_3)_2PbI_4$, *Phys. Rev. B* 42 (1990) 11099–11107. https://doi.org/10.1103/PhysRevB.42.11099.

[65] Y. Takeoka, M. Fukasawa, T. Matsui, K. Kikuchi, M. Rikukawa, K. Sanui, Intercalated Formation of Two-Dimensional and Multi-Layered Perovskites in Organic Thin Films, *Chem. Comm.* (2005) 378. https://doi.org/10.1039/b413398f.

[66] B. Saparov, D.B. Mitzi, Organic–Inorganic Perovskites: Structural Versatility for Functional Materials Design, *Chem. Rev.* 116 (2016) 4558–4596. https://doi.org/10.1021/acs.chemrev.5b00715.

[67] X. Gong, O. Voznyy, A. Jain, W. Liu, R. Sabatini, Z. Piontkowski, G. Walters, G. Bappi, S. Nokhrin, O. Bushuyev, M. Yuan, R. Comin, D. McCamant, S.O. Kelley, E.H. Sargent, Electron–Phonon Interaction in Efficient Perovskite Blue Emitters, *Nat. Mater.* 17 (2018) 550–556. https://doi.org/10.1038/s41563-018-0081-x.

[68] M. Szafrański, A. Katrusiak, Photovoltaic Hybrid Perovskites under Pressure, *J. Phys. Chem. Lett.* 8 (2017) 2496–2506. https://doi.org/10.1021/acs.jpclett.7b00520.

[69] R. Zhang, W. Cai, T. Bi, N. Zarifi, T. Terpstra, C. Zhang, Z.V. Verdeny, E. Zurek, S. Deemyad, Effects of Nonhydrostatic Stress on Structural and Optoelectronic Properties of Methylammonium Lead Bromide Perovskite, *J. Phys. Chem. Lett.* 8 (2017) 3457–3465. https://doi.org/10.1021/acs.jpclett.7b01367.

[70] L. Kong, G. Liu, J. Gong, Q. Hu, R.D. Schaller, P. Dera, D. Zhang, Z. Liu, W. Yang, K. Zhu, Y. Tang, C. Wang, S.-H. Wei, T. Xu, H. Mao, Simultaneous Band-Gap Narrowing and Carrier-Lifetime Prolongation of Organic–Inorganic Trihalide Perovskites, *Proc. Natl. Acad. Sci.* 113 (2016) 8910–8915. https://doi.org/10.1073/pnas.1609030113.

[71] Y.-Q. Zhao, Q.-R. Ma, B. Liu, Z.-L. Yu, M.-Q. Cai, Pressure-Induced Strong Ferroelectric Polarization in Tetra-Phase Perovskite $CsPbBr_3$, *Phys. Chem. Chem. Phys.* 20 (2018) 14718–14724. https://doi.org/10.1039/C8CP01338A.

[72] W. Cai, J. He, H. Li, R. Zhang, D. Zhang, D.Y. Chung, T. Bhowmick, C. Wolverton, M.G. Kanatzidis, S. Deemyad, Pressure-Induced Ferroelectric-Like Transition Creates a Polar Metal in Defect Antiperovskites $Hg_3Te_2X_2$ ($X = Cl$, Br), *Nat. Commun.* 12 (2021) 1509. https://doi.org/10.1038/s41467-021-21836-7.

[73] L. Zhang, L. Wu, K. Wang, B. Zou, Pressure-Induced Broadband Emission of 2D Organic–Inorganic Hybrid Perovskite $(C_6H_5C_2H_4NH_3)_2PbBr_4$, *Adv. Sci.* 6 (2019). https://doi.org/10.1002/advs.201801628.

[74] S. Guo, Y. Zhao, K. Bu, Y. Fu, H. Luo, M. Chen, M.P. Hautzinger, Y. Wang, S. Jin, W. Yang, X. Lü, Pressure-Suppressed Carrier Trapping Leads to Enhanced Emission in Two-Dimensional Perovskite $(HA)_2(GA)Pb_2I_7$, *Angew. Chem. Int. Ed.* 59 (2020) 17533–17539. https://doi.org/10.1002/anie.202001635.

[75] M. Szafrański, A. Katrusiak, K. Ståhl, Time-Dependent Transformation Routes of Perovskites $CsPbBr_3$ and $CsPbCl_3$ under High Pressure, *J. Mater. Chem. A* 9 (2021) 10769–10779. https://doi.org/10.1039/d1ta01875b.

[76] C. Song, H. Yang, F. Liu, G.J. Cheng, Ultrafast Femtosecond Pressure Modulation of Structure and Exciton Kinetics in 2D Halide Perovskites for Enhanced Light Response and Stability, *Nat. Commun.* 12 (2021) 4879. https://doi.org/10.1038/s41467-021-25140-2.

[77] S. Dai, Tuning the Circularly Polarized Photoluminescence of Chiral 2D Perovskites by High Pressure, *ArXiv* (2023). https://doi.org/10.48550/arXiv.2308.11622.

[78] T. Yin, B. Liu, J. Yan, Y. Fang, M. Chen, W.K. Chong, S. Jiang, J.-L. Kuo, J. Fang, P. Liang, S. Wei, K.P. Loh, T.C. Sum, T.J. White, Z.X. Shen, Pressure-Engineered Structural and Optical Properties of Two-Dimensional $(C_4H_9NH_3)_2PbI_4$ Perovskite Exfoliated nm-Thin Flakes, *J. Am. Chem. Soc.* 141 (2019) 1235–1241. https://doi.org/10.1021/jacs.8b07765.

[79] D. Stojkovski, M. Szafrański, High-Pressure Structural and Optical Studies of Pure Low-Dimensional Cesium Lead Chlorides $CsPb_2Cl_5$ and Cs_4PbCl_6, *Inorg. Chem.* 63 (2024) 7903–7911. https://doi.org/10.1021/acs.inorgchem.4c00809.

[80] O. Nazarenko, M.R. Kotyrba, M. Wörle, E. Cuervo-Reyes, S. Yakunin, M. V. Kovalenko, Luminescent and Photoconductive Layered Lead Halide Perovskite Compounds Comprising Mixtures of Cesium and Guanidinium Cations, *Inorg. Chem.* 56 (2017) 11552–11564. https://doi.org/10.1021/acs.inorgchem.7b01204.

[81] V. Pawar, M. Kumar, P.A. Jha, S.K. Gupta, A.S.K. Sinha, P.K. Jha, P. Singh, Ambient Atmospheric Temperature Processed Lead Halide Perovskites, *J. Therm. Anal. Calorim.* 139 (2020) 3073–3078. https://doi.org/10.1007/s10973-019-08676-w.

[82] C. Qin, T. Matsushima, D. Klotz, T. Fujihara, C. Adachi, The Relation of Phase-Transition Effects and Thermal Stability of Planar Perovskite Solar Cells, *Adv. Sci.* 6 (2019). https://doi.org/10.1002/advs.201801079.

[83] Agilent Technologies, CrysAlisPro: Data Collection and Processing Software for X-Ray Diffractometers, (2010).

[84] Sheldrick G.M., A Short History of SHELX, *Acta Crystallogr. A* 64 (2008) 112–122.

[85] O. V. Dolomanov, L.J. Bourhis, R.J. Gildea, J.A.K. Howard, H. Puschmann, *OLEX2*: a Complete Structure Solution, Refinement and Analysis Program, *J. Appl. Crystallogr.* 42 (2009) 339–341. https://doi.org/10.1107/S0021889808042726.

[86] J. Tauc, R. Grigorovici, A. Vancu, Optical Properties and Electronic Structure of Amorphous Germanium, *Phys. Status Solidi B* 15 (1966) 627–637. https://doi.org/10.1002/pssb.19660150224.

[87] L. Merrill, W.A. Bassett, Miniature Diamond Anvil Pressure Cell for Single Crystal X-Ray Diffraction Studies, *Rev. Sci. Instrum.* 45 (1974) 290–294. https://doi.org/10.1063/1.1686607.

[88] G.J. Piermarini, S. Block, J.D. Barnett, Hydrostatic Limits in Liquids and Solids to 100 kbar, *J. Appl. Phys.* 44 (1973) 5377–5382. https://doi.org/10.1063/1.1662159.

[89] K. Murata, S. Aoki, Development of High Pressure Medium Achieving High Quality Hydrostatic Pressure, *The Review of High Pressure Science and Technology* 26 (2016) 3–7. https://doi.org/10.4131/jshpreview.26.3.

[90] D. Staško, J. Prchal, M. Klicpera, S. Aoki, K. Murata, Pressure Media for High Pressure Experiments, Daphne Oil 7000 series, *High Press. Res.* 40 (2020) 525–536. https://doi.org/10.1080/08957959.2020.1825706.

[91] G.J. Piermarini, S. Block, J.D. Barnett, R.A. Forman, Calibration of the Pressure Dependence of the R_1 Ruby Fluorescence Line to 195 kbar, *J. Appl. Phys.* 46 (1975) 2774–2780. https://doi.org/10.1063/1.321957.

[92] D.D. Ragan, R. Gustavsen, D. Schiferl, Calibration of the Ruby R_1 and R_2 Fluorescence Shifts as a Function of Temperature from 0 to 600 K, *J. Appl. Phys.* 72 (1992) 5539–5544. https://doi.org/10.1063/1.351951.

[93] A. Katrusiak, Shadowing and Absorption Corrections of Single-Crystal High-Pressure Data, *Z. Kristallogr. Cryst. Mater.* 219 (2004) 461–467. https://doi.org/10.1524/zkri.219.8.461.38328.

[94] M. Rivers, V. Prakapenka, A. Kubo, C. Pullins, C. Holl, S. Jacobsen, The COMPRES/GSECARS Gas-Loading System for Diamond Anvil Cells at the Advanced Photon Source, *High Press. Res.* 28 (2008) 273–292. https://doi.org/10.1080/08957950802333593.

[95] V. Drushliak, M. Szafrański, Thermodynamic Stability, Structure, and Optical Properties of Perovskite-Related $CsPb_2Br_5$ Single Crystals under Pressure, *Inorg. Chem.* 61 (2022) 14389–14396. https://doi.org/10.1021/acs.inorgchem.2c02253.

[96] K.-H. Wang, L. Wu, L. Li, H.-B. Yao, H.-S. Qian, S.-H. Yu, Large-Scale Synthesis of Highly Luminescent Perovskite-Related $CsPb_2Br_5$ Nanoplatelets and Their Fast Anion Exchange, *Angew. Chem.* 128 (2016) 8468–8472. https://doi.org/10.1002/ange.201602787.

[97] C. Qin, T. Matsushima, A.S.D. Sandanayaka, Y. Tsuchiya, C. Adachi, Centrifugal-Coated Quasi-Two-Dimensional Perovskite $CsPb_2Br_5$ Films for Efficient and Stable Light-Emitting Diodes, *J. Phys. Chem. Lett.* 8 (2017) 5415–5421. https://doi.org/10.1021/acs.jpclett.7b02371.

[98] X. Tang, S. Han, Z. Zu, W. Hu, D. Zhou, J. Du, Z. Hu, S. Li, Z. Zang, All-Inorganic Perovskite $CsPb_2Br_5$ Microsheets for Photodetector Application, *Front. Phys.* 5 (2018). https://doi.org/10.3389/fphy.2017.00069.

[99] Z. Ma, F. Li, G. Qi, L. Wang, C. Liu, K. Wang, G. Xiao, B. Zou, Structural Stability and Optical Properties of Two-Dimensional Perovskite-Like $CsPb_2Br_5$ Microplates in Response to Pressure, *Nanoscale* 11 (2019) 820–825. https://doi.org/10.1039/c8nr05684f.

[100] M. Rodová, J. Brožek, K. Knížek, K. Nitsch, Phase Transitions In Ternary Caesium Lead Bromide, *J. Therm. Anal. Calorim.* 71 (2003) 667–673. https://doi.org/10.1023/A:1022836800820.

[101] V. Drushliak, K.J. Kapcia, M. Szafrański, White-Light Emission Triggered By Pseudo Jahn–Teller Distortion At The Pressure-Induced Phase Transition in Cs_4PbBr_6, *J. Mater. Chem. C* Mater 12 (2024) 4360–4368. https://doi.org/10.1039/D4TC00036F.

[102] M.I. Saidaminov, J. Almutlaq, S. Sarmah, I. Dursun, A.A. Zhumekenov, R. Begum, J. Pan, N. Cho, O.F. Mohammed, O.M. Bakr, Pure Cs_4PbBr_6: Highly Luminescent Zero-Dimensional Perovskite Solids, *ACS Energy Lett.* 1 (2016) 840–845. https://doi.org/10.1021/acsenergylett.6b00396.

[103] D. Chen, Z. Wan, X. Chen, Y. Yuan, J. Zhong, Large-Scale Room-Temperature Synthesis and Optical Properties of Perovskite-Related Cs_4PbBr_6 Fluorophores, *J. Mater. Chem. C* 4 (2016) 10646–10653. https://doi.org/10.1039/C6TC04036E.

[104] J.-H. Cha, J.H. Han, W. Yin, C. Park, Y. Park, T.K. Ahn, J.H. Cho, D.-Y. Jung, Photoresponse of $CsPbBr_3$ and Cs_4PbBr_6 Perovskite Single Crystals, *J. Phys. Chem. Lett.* 8 (2017) 565–570. https://doi.org/10.1021/acs.jpclett.6b02763.

[105] M. Nikl, E. Mihokova, K. Nitsch, F. Somma, C. Giampaolo, G.P. Pazzi, P. Fabeni, S. Zazubovich, Photoluminescence of Cs_4PbBr_6 Crystals and Thin Films, *Chem. Phys. Lett.* 306 (1999) 280–284. https://doi.org/10.1016/S0009-2614(99)00477-7.

[106] Z. Ma, Z. Liu, S. Lu, L. Wang, X. Feng, D. Yang, K. Wang, G. Xiao, L. Zhang, S.A.T. Redfern, B. Zou, Pressure-Induced Emission of Cesium Lead Halide Perovskite Nanocrystals, *Nat. Commun.* 9 (2018) 4506. https://doi.org/10.1038/s41467-018-06840-8.

[107] V. Drushliak, M. Szafrański, Effect of Pressure and Temperature on the Structure and Optical Properties of Two-Dimensional Lead Iodide Perovskites, *Chem. Comm*. 61 (2025) 8019–8022. https://doi.org/10.1039/D5CC01232E.

[108] M. Szafrański, A. Katrusiak, Phase Transitions in the Layered Structure of Diguanidinium Tetraiodoplumbate, *Phys. Rev. B* 61 (2000) 1026–1035. https://doi.org/10.1103/PhysRevB.61.1026.

Statements of co-authors

Poznań, 15th September, 2025

Prof. dr hab. Marek Szafrański
Department of Experimental Physics of Condensed Phase
Institute of Physics
Faculty of Physics and Astronomy
Adam Mickiewicz University in Poznań
ul. Uniwersytetu Poznańskiego 2, 61-614 Poznań, Poland
e-mail: masza@amu.edu.pl

Co-author Statement

I hereby confirm that I am a co-author of the following publications:

1. Drushliak, V. and Szafrański, M. "Thermodynamic stability, structure, and optical properties of perovskite-related $CsPb_2Br_5$ single crystals under pressure", **Inorg. Chem.**, 2022, 61, 14389-14396.

2. Drushliak, V., Kapcia, K. J. and Szafrański, M. "White-light emission triggered by pseudo Jahn–Teller distortion at the pressure-induced phase transition in Cs_4PbBr_6", ***J. Mater. Chem. C***, 2024,12, 4360-4368.

3. Drushliak, V. and Szafrański, M. "Effect of pressure and temperature on the structure and optical properties of two-dimensional lead iodide perovskites", **Chem. Commun.**, 2025, 61, 8019-8022.

My contribution to these works included conceptualisation, designing and supervision of the experiments, discussing the results, co-writing the manuscripts, and final editing.

M. Szafrański
Marek Szafrański

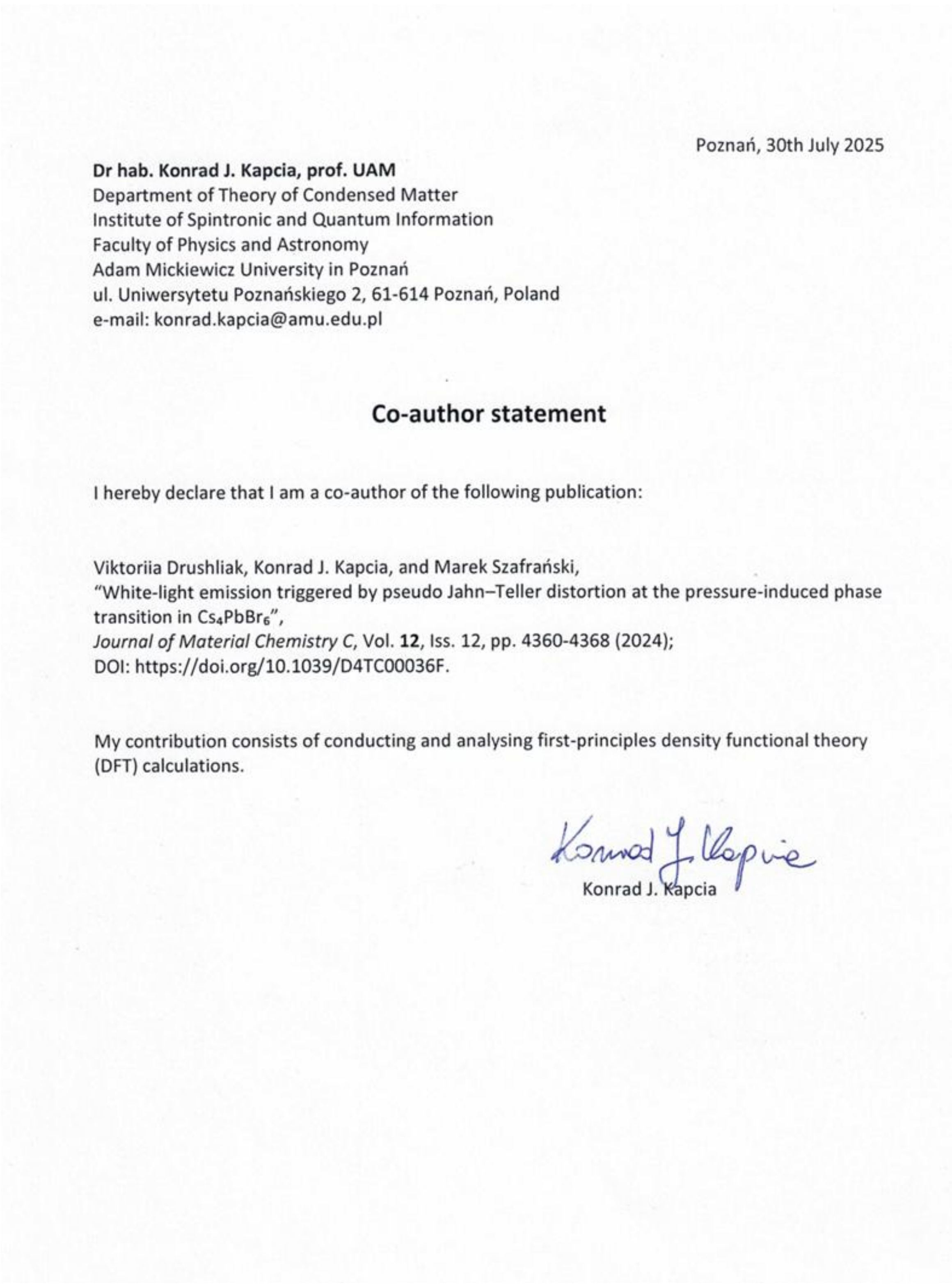

Poznań, 30th July 2025

Dr hab. Konrad J. Kapcia, prof. UAM
Department of Theory of Condensed Matter
Institute of Spintronic and Quantum Information
Faculty of Physics and Astronomy
Adam Mickiewicz University in Poznań
ul. Uniwersytetu Poznańskiego 2, 61-614 Poznań, Poland
e-mail: konrad.kapcia@amu.edu.pl

Co-author statement

I hereby declare that I am a co-author of the following publication:

Viktoriia Drushliak, Konrad J. Kapcia, and Marek Szafrański,
"White-light emission triggered by pseudo Jahn–Teller distortion at the pressure-induced phase transition in Cs_4PbBr_6",
Journal of Material Chemistry C, Vol. **12**, Iss. 12, pp. 4360-4368 (2024);
DOI: https://doi.org/10.1039/D4TC00036F.

My contribution consists of conducting and analysing first-principles density functional theory (DFT) calculations.

Konrad J. Kapcia

Konrad J. Kapcia

Publications

1. *Thermodynamic stability, structure, and optical properties of perovskite-related $CsPb_2Br_5$ single crystals under pressure*
   Viktoriia Drushliak, Marek Szafrański
   Inorg. Chem., **2022** *61* (36), 14389-14396 (Open Access)
   https://doi.org/10.1021/acs.inorgchem.2c02253

2. *White-light emission triggered by pseudo Jahn–Teller distortion at the pressure-induced phase transition in Cs_4PbBr_6*
   Viktoriia Drushliak, Konrad J. Kapcia, Marek Szafrański
   J. Mater. Chem. C, **2024**, 12, 4360-4368
   https://doi.org/10.1039/D4TC00036F

3. *Effect of pressure and temperature on the structure and optical properties of two-dimensional lead iodide perovskites*
   Viktoriia Drushliak, Marek Szafrański
   Chem. Commun., **2025**, 61, 8019-8022
   https://doi.org/10.1039/D5CC01232E

Inorganic Chemistry

pubs.acs.org/IC

Article

Thermodynamic Stability, Structure, and Optical Properties of Perovskite-Related $CsPb_2Br_5$ Single Crystals under Pressure

Viktoriia Drushliak and Marek Szafrański*

Cite This: *Inorg. Chem.* 2022, 61, 14389−14396

Read Online

ACCESS | Metrics & More | Article Recommendations | Supporting Information

ABSTRACT: $CsPb_2Br_5$ belongs to all inorganic perovskite-related quasi-two-dimensional materials that have attracted considerable attention due to their potential for optoelectronic applications. In this study, we solve numerous controversies on the physical properties of this material. We show that optical absorption in the visible spectrum and green photoluminescence are due to microcrystallites of the three-dimensional $CsPbBr_3$ perovskite settled on the $CsPb_2Br_5$ plates and that carefully cleaned crystal plates are devoid of these features. The high-pressure structural and spectroscopic experiments, performed on the single crystals free of $CsPbBr_3$ impurities, evidenced that the layered tetragonal structure of $CsPb_2Br_5$ is stable at least up to 6 GPa. The absorption edge is located in the ultraviolet at around 350 nm and continuously red shifts under pressure. Moderate band gap narrowing is well correlated to the pressure-induced changes in the crystal structure. Although the compressibility of $CsPb_2Br_5$ is much higher than for $CsPbBr_3$, the response in optical properties is weaker because the Pb−Br layers responsible for the optical absorption are much less affected by hydrostatic pressure than those built of Cs^+ cations. Our study clarifies the confusing data in the literature on the optical properties and thermodynamic stability of $CsPb_2Br_5$.

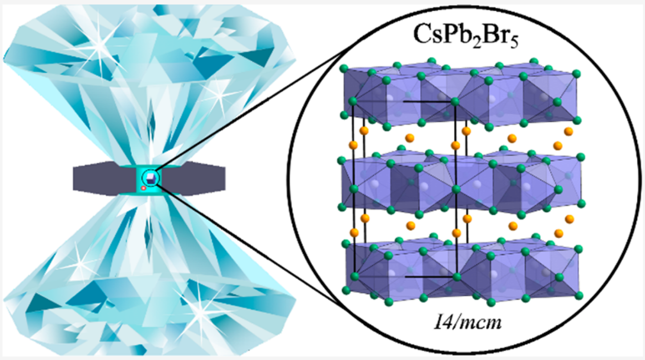

1. INTRODUCTION

In the recent decade, organic−inorganic perovskite semiconductors have attracted unprecedented attention from the scientific community.[1] This interest stems from their excellent photovoltaic and optoelectronic properties combined with easy and low-cost fabrication. However, the long-term stability problems in the operating environment have not yet been solved. In this area, a very promising research direction is connected with all-inorganic perovskites that exhibit better resistance to atmospheric conditions, while their optoelectronic parameters are comparable to those of their hybrid counterparts, as was demonstrated for $CsPbBr_3$.[2] Cesium lead bromide can crystallize in orange (three-dimensional, 3D) and white (one-dimensional, 1D) forms, but also with different stoichiometries,[3] forming low-dimensional structures: Cs_4PbBr_6, often termed a zero-dimensional perovskite (0D), and $CsPb_2Br_5$, exhibiting a two-dimensional architecture (2D). These low-dimensional perovskite-related materials have gained remarkable interest because of strong photoluminescence (PL) in the visible spectrum,[4,5] reported recently, which opens prospects for applications in light-emitting diodes,[6] lasers,[7] and photodetectors.[8,9]

Here, we present a systematic structural and optical spectroscopic high-pressure study performed on pure single crystals of $CsPb_2Br_5$. In the tetragonal structure of $CsPb_2Br_5$, the bicapped trigonal prisms $PbBr_8$ are connected by faces into layers perpendicular to the *c*-axis. These Pb−Br layers are sandwiched between layers composed of Cs^+ cations.[10,11] The crystal structure is shown in Figure 1. The quasi-2D character of the structure should result in a wider band gap compared to that of the 3D orange form of $CsPbBr_3$ for which the energy gap $E_g = 2.34$ eV[12] ($\lambda = 530$ nm). Indeed, in the original work,[3] published by Wells in 1893, $CsPb_2Br_5$ is characterized as a white powder, indicating an absorption edge in the ultraviolet region. Therefore, the location of the absorption edge in the visible spectrum around 515−525 nm in numerous papers[5,6,8,13] is highly questionable because in that case the crystal could not be colorless. Furthermore, theoretical calculations of the electronic structure indicate that the energy gap in $CsPb_2Br_5$ is of indirect type,[5,10,14] and for that reason, strong PL should be excluded. In fact, detailed studies of carefully prepared material showed that pure $CsPb_2Br_5$ does not absorb light in the visible region and is PL inactive.[10,14,15] The controversial strong green emission was discussed by

Received: June 28, 2022
Published: September 1, 2022

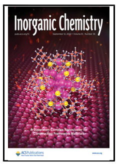

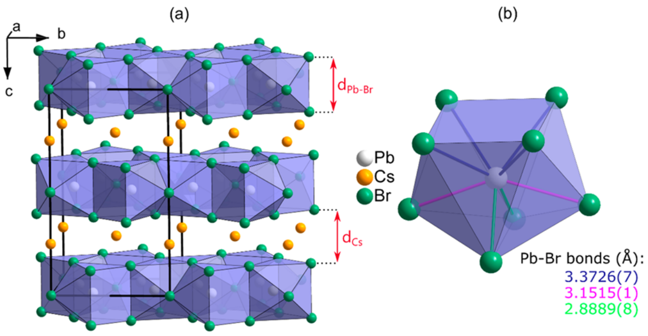

Figure 1. (a) Crystal structure of $CsPb_2Br_5$ with the thickness of the Pb−Br and Cs layers marked by the arrows and (b) the bicapped trigonal prism $PbBr_8$ being the building unit of the Pb−Br layers. The three different Pb−Br distances and their values determined under ambient conditions are marked with different colors.

several groups, which indicated possible origins of this emission, such as impurities of the orange phase of $CsPbBr_3$ mixed with $CsPb_2Br_5$,[16] $CsPbBr_3$ nanocrystals embedded in $CsPb_2Br_5$ microplates,[17] amorphous lead bromide ammonium complexes present on the surface of the nanosheets,[18] or intrinsic crystal defects.[19] It appears that the methodology of $CsPb_2Br_5$ preparation is crucial in this respect because even a small amount of $CsPbBr_3$ admixture strongly affects the optical properties of the material obtained. This is clearly seen in previously published studies,[5,6,8,13] where on the basis of the standard powder X-ray diffraction analysis the material is defined as "pure", while its absorption edge and PL properties are evidently dominated by the presence of the orange form of $CsPbBr_3$, and they are dramatically different from those of the truly pure substance.[10,15] Although from the point of view of optoelectronic applications the strongly light-emitting two-phase material is very attractive, the physical properties determined for such material and their assignment to the pure form lead to misleading information and errors of interpretation of the data.

In this study, we report the response of the $CsPb_2Br_5$ structure to hydrostatic pressure and the related changes in the optical properties of the crystal. Special emphasis was placed on the synthesis and crystallization procedures. We show that our results obtained for pure single crystals are completely different from those published previously.[13]

2. MATERIALS AND METHODS

2.1. Chemicals. Cesium carbonate (Aldrich, 99%), hydrobromic acid for analysis (Acros Organics, 48% solution in water), and lead(II) acetate trihydrate (Aldrich, 99.999%) were purchased and used without further purification. The water was purified by double distillation.

2.2. Synthesis of $CsPb_2Br_5$. Cesium bromide and lead(II) bromide were obtained by reactions of hydrobromic acid with cesium carbonate and lead(II) acetate trihydrate. The stoichiometric amounts of CsBr and $PbBr_2$ were dissolved in hot water acidified with HBr. Slow cooling of the solution to room temperature resulted in the crystallization of thin $CsPb_2Br_5$ plates. The precipitated crystals were filtrated, washed with hexane, and dried. We also performed a series of crystallizations to determine the optimal conditions for growing the good-quality pure crystals. In these experiments, the amount of HBr acid in the solution and/or the CsBr:$PbBr_2$ ratio were modified.

2.3. Calorimetric and Thermogravimetric Analysis. The thermal stability of $CsPb_2Br_5$ was studied by the thermogravimetric analysis method (TGA) using a TGA Q50 instrument (TA Instruments) and by differential scanning calorimetry (DSC) with a

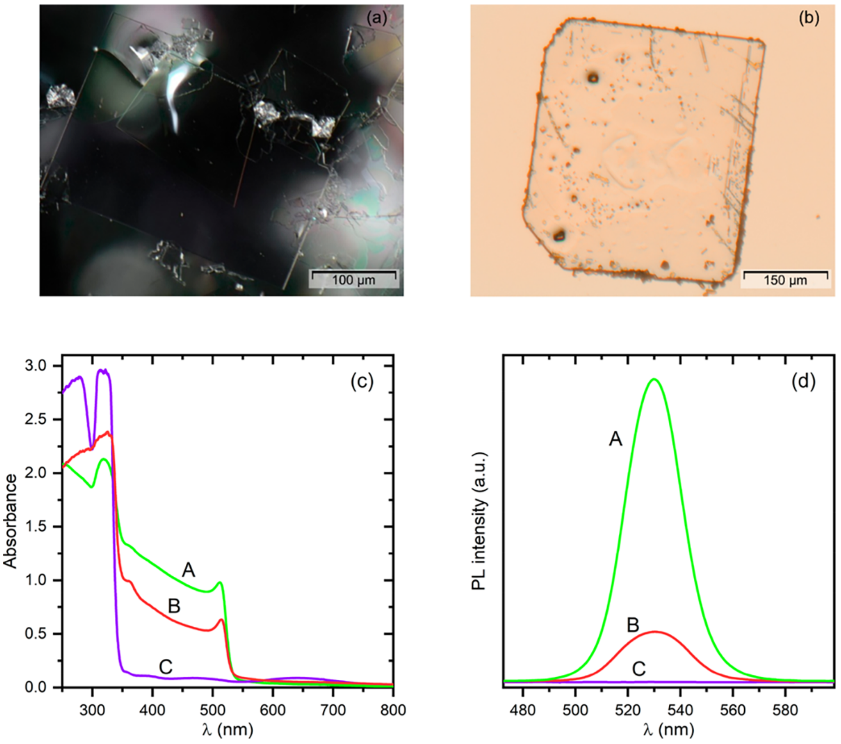

Figure 2. Photographs of crystals taken from the solution: (a) after washing and drying (reflected light) and (b) after drying only, with visible microcrystals of orange $CsPbBr_3$ crystallized on the surface plate (transmitted light). Absorption (c) and photoluminescence (d) spectra of $CsPb_2Br_5$. The spectra recorded for two different as-grown (unwashed) crystal plates are marked by A and B, and the spectra of the cleaned plate are marked by C.

https://doi.org/10.1021/acs.inorgchem.2c02253
Inorg. Chem. 2022, 61, 14389−14396

Q2000 calorimeter (TA Instruments). DSC experiments were performed on as-grown crystals while TGA runs were measured on powdered samples, both at a temperature change rate of 10 K min^{-1}.

2.4. Single-Crystal High-Pressure X-ray Diffraction. A Merrill-Bassett diamond anvil cell (DAC)[20] equipped with diamond anvils (type Ia, 800 μm culets) supported on steel discs with conical windows was used for single-crystal X-ray diffraction (SCXRD) high-pressure experiments. The single crystal of $CsPb_2Br_5$ and the ruby chip for pressure calibration were glued to the culet of one anvil and placed into the spark-eroded hole in the tungsten gasket (initial thickness 250 μm, hole diameter 350−380 μm). The chamber was filled with isopropanol as a pressure medium, ensuring hydrostatic conditions up to ~4.2 GPa.[21] The pressure inside the DAC was monitored by using the ruby fluorescence method,[22] before and after each measurement. The overall pressure uncertainty was <0.03 GPa. All SCXRD measurements were performed at room temperature by using an Oxford Diffraction Gemini A Ultra diffractometer operating with graphite-monochromated Mo Kα radiation (λ = 0.71073 Å). Data were collected and processed by using CrysAlisPro software.[23] The structures were solved and refined by using SHELX programs.[24] Crystallographic information files (CIFs) for $CsPb_2Br_5$ structures determined under different pressures (2176587−2176600) have been deposited in the Inorganic Crystal Structure Database.

2.5. Optical Measurements. For high-pressure optical spectroscopic measurements, diamond anvils type IIa, supported by tungsten carbide seats with conical windows, were used. The hydrostatic liquid and other experimental details were the same as in the case of diffraction experiments. The pressure dependence of the absorption edge was measured on a 3.9 μm thick plate and on a nanosheet of the average thickness 30 nm, which was grown in situ on the diamond culet surface. The thickness of the nanosheet was determined with the atomic force microscopy (AFM) technique, whereas an interference method combined with optical microscopy was used to measure the thickness of the microplates (see Figure S1). Absorption and diffuse reflectance spectra were recorded by a Jasco MSV-5100 microscopic spectrophotometer. The absorption spectra were collected from the small area of the crystals of 30 μm in diameter by using a continuous speed of 200 nm min^{-1} and a spectral bandwidth of 5 nm.

PL spectra were measured with a homemade attachment to the Jasco MSV-5100 spectrophotometer, where a xenon lamp served as an excitation source in the spectral range 320−500 nm, and a Spectra Academy SV2100 spectrometer was applied for analysis of the spectrum emitted by the sample. All spectroscopic measurements were performed at room temperature.

3. RESULTS AND DISCUSSION

3.1. Characterization of the Material. An overview of the papers published on $CsPb_2Br_5$ shows a large diversity of methods applied for the synthesis and crystallization of this material.[3,5,6,10,14,16,25−28] Many of these studies were focused on the preparation of microcrystals or nanocrystals by triggering off a sudden crystallization through a hot injection method.[8,13,14,17,18,25] In such syntheses, the control of a single-phase crystallization is limited, especially when the substrates can form structures of different stoichiometries. For the purposes of this work, we used the simplest method of crystallization from an aqueous solution, which was already described by Wells in 1893[3] and has been successfully used recently.[11,15] The obtained crystals were colorless and of good optical quality (Figure 2a). Their layered tetragonal symmetry structure was confirmed by SCXRD measurements (Figure 1; for details, see also Table S1). The space group symmetry $I4/mcm$ and the lattice parameters $a = b$ = 8.4931(1) Å and c = 15.1786(3) Å are consistent with the previously reported data.[29] According to our DSC and TGA measurements, this structure is stable at least between 95 and 625 K (see Figures S2 and S3). In particular, our study did not confirm the thermal anomaly observed previously at 341.5 K.[30] The only DSC anomaly was detected at 625 K, where the crystal melts.

The purity of the crystals grown, and especially the presence of $CsPbBr_3$ admixture, was monitored by the absorption spectroscopy method. The orange form of $CsPbBr_3$ exhibits strong absorption below ca. 530 nm, and even trace amounts of this substance in the studied material are clearly reflected in the absorption spectrum. Therefore, this method is much more sensitive than the commonly used powder X-ray diffraction. The crystallizations performed from the water solutions, acidified with different amounts of HBr, showed that all of the obtained and carefully cleaned crystals exhibit the same optical properties; that is, they are colorless and transparent, their absorption edge is located below 350 nm, and they are devoid of green PL (see plots C in Figure 2c,d). This also concerns the crystals grown from the strongly acidified solution, which crystallized together with the orange form of $CsPbBr_3$. The only visible difference was in the thickness of the plates, which clearly increased with the amount of acid in the solution. This is a result of the better solubility of the substrates and their higher concentrations in the acidified solution. It is well-known that the 3D $CsPbBr_3$ perovskite crystallizes in water solution only at a sufficiently high concentration of HBr; otherwise, $CsPb_2Br_5$ is formed,[3] regardless of the 1:1 stoichiometry of CsBr:$PbBr_2$ in the solution. Our experiments confirmed that also in solutions containing an excess of CsBr the crystals of $CsPb_2Br_5$ were obtained in pure form. Thus, it is evident that $CsPb_2Br_5$ crystallizes without any inclusions of $CsPbBr_3$, even in solutions of disturbed stoichiometry. However, it should be noticed that the crystals harvested from the solution have to be carefully washed and dried to remove the remaining solution. Living these remains on crystal plates leads to an increase in HBr concentration in the droplets of the mother liquor due to water evaporation, and finally it results in the precipitation of $CsPbBr_3$ micro- and nanocrystallites on the surface of $CsPb_2Br_5$ crystals (Figure 2b). Therefore, such "unwashed" crystal plates absorb light in the visible spectrum below 520−530 nm and exhibit strong green PL; that is, they show typical characteristics of the orange form of $CsPbBr_3$. This is illustrated in Figure 2c,d where the absorption and PL spectra of two as-grown unwashed plates (A, B) and of the cleaned plate (C) are shown. The intensity of PL is correlated to the absorbance of the samples in the spectral range 350−550 nm, which clearly depends on the amount of $CsPbBr_3$ on the crystal surfaces. All our further experiments were performed on pure $CsPb_2Br_5$ crystals.

A review of data from the literature shows that the optical spectrum of $CsPb_2Br_5$ has been the subject of numerous studies, but only very few experiments have been performed for noncontaminated samples. In Figure 3 we compare the spectrum measured by the diffuse reflectance method with that obtained from the optical absorption measurements on the 30 nm thick sheet. The reflective spectrum is presented in the form of a normalized Kubelka−Munk function,[31] $F(R_\infty) = \alpha/S = (1 - R_\infty)^2/2R_\infty$, where α is the absorption coefficient, S is the scattering coefficient of the powdered sample, and R_∞ is the diffuse reflectance of an infinitely thick layer. The two peaks visible in this spectrum at 336 nm (3.69 eV) and 307 nm (4.04 eV) are in excellent agreement with the earlier reflectance data.[11] However, a comparison with the conventional absorption spectrum reveals essential differences, as the absorption peaks are clearly blue shifted to 320 nm (3.87 eV)

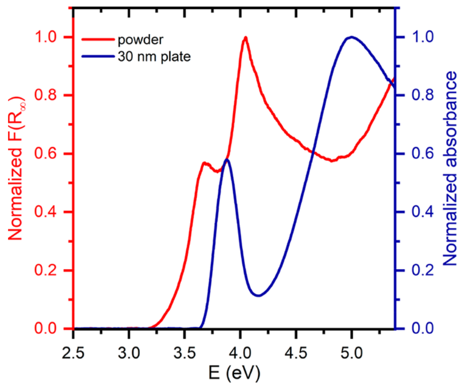

Figure 3. Normalized Kubelka−Munk function for powdered sample (left *Y*-axis) and normalized absorbance for 30 nm thick plate (right *Y*-axis) as functions of energy.

and 255 nm (4.86 eV), respectively. This discrepancy can indicate a substantial difference between the bulk electronic states, responsible for the transient absorbance, and the surface electronic states that contribute mainly to the reflection. For comparison purposes, we also measured the diffuse reflectance and absorption spectra of the 3D perovskite $MAPbBr_3$. These spectra, plotted in Figure S4, show the same trend as in the case of $CsPb_2Br_5$. Therefore, it is evident that the energy gaps determined from the absorption and reflectance data can differ considerably. It is worth noting that the onset of 3D lead-halide perovskites absorption is dominated by excitonic absorption,[32] and it is also characteristic of 2D $CsPb_2Br_5$, for which the excitonic band at 320 nm determines the absorption edge of the crystal.

3.2. Pressure Dependence of Structural Parameters of $CsPb_2Br_5$.

The SCXRD data were collected in the pressure range to 4.2 GPa. As shown in Figure 4, the hydrostatic compression of the crystal results in a continuous shortening of the lattice parameters and a decrease in the unit cell volume. The monotonic contraction of the crystal, as well as the preservation of the space group symmetry *I*4/*mcm* in the whole studied pressure range, testifies that this layered structure is highly stable not only in a wide temperature range but also under pressure. The lack of structural transformation is surprising in contrast to the recently published high-pressure study of $CsPb_2Br_5$, where an isostructural phase transition was postulated at 1.6 GPa,[13] associated with a stepwise change in the lattice parameters and ∼3% decrease in the unit-cell volume. However, it should be noted that in this study the measurements by powder XRD were performed by using silicon oil as a pressure medium, which is hydrostatic to ∼1 GPa only. In this case, the pressure dependence of the lattice parameters can be strongly distorted by the nonhydrostatic conditions of the experiments. For the sake of comparison, our $V(p)$ data are plotted in Figure S5a together with those previously reported in ref 13. The most striking is a deepening discrepancy between these two data sets as the pressure increases. For example, at atmospheric pressure the unit-cell volume determined from our single-crystal data ($V = 1092$ Å^3) is very close to that measured by the powder diffraction method in ref 13 ($V = 1088$ Å^3), while under a pressure of 4 GPa the corresponding values strongly diverge (925 vs 965 Å^3, respectively). Moreover, it is worth noting that the discontinuities in the lattice parameters derived from the powder diffraction data are in fact hardly correlated to the smooth changes in the presented diffraction patterns,[13] and therefore the reported phase transition seems to be highly questionable.

The experimental $V(p)$ data plotted in Figure 4b were fitted by the third-order Birch−Murnaghan equation of state:[33]

$$p(V) = \frac{3B_0}{2}\left[\left(\frac{V_0}{V}\right)^{7/3} - \left(\frac{V_0}{V}\right)^{5/3}\right]\left\{1 + \frac{3}{4}(B_0' - 4)\left[\left(\frac{V_0}{V}\right)^{2/3} - 1\right]\right\}$$

where V_0 is the volume of the reference unit cell at ambient pressure, B_0 is the isothermal bulk modulus at ambient pressure, and B_0' is the pressure derivative of the bulk modulus extrapolated to $p = 0$. The fitting procedure performed by using EosFit7-GUI program[34] allowed us to determine the bulk modulus $B_0 = 11.5(3)$ GPa and its derivative $B_0' = 9.3(6)$ of $CsPb_2Br_5$. These parameters can be compared with those of $CsPbBr_3$. For this purpose, the single-crystal $V(p)$ data published recently for the orange form of $CsPbBr_3$[12] were fitted by the third-order Birch−Murnaghan equation (see Figure S5b) with $B_0 = 15.0(8)$ GPa and $B_0' = 6.0(18)$. Because B_0 and B_0' are correlated,[36] a comparison of these parameters for $CsPb_2Br_5$ and $CsPbBr_3$ was made by plotting B_0' versus B_0, together with their confidence ellipses, as illustrated in Figure S8. This plot shows that the confidence ellipses do not overlap even at the 99.7% confidence level, and therefore we conclude

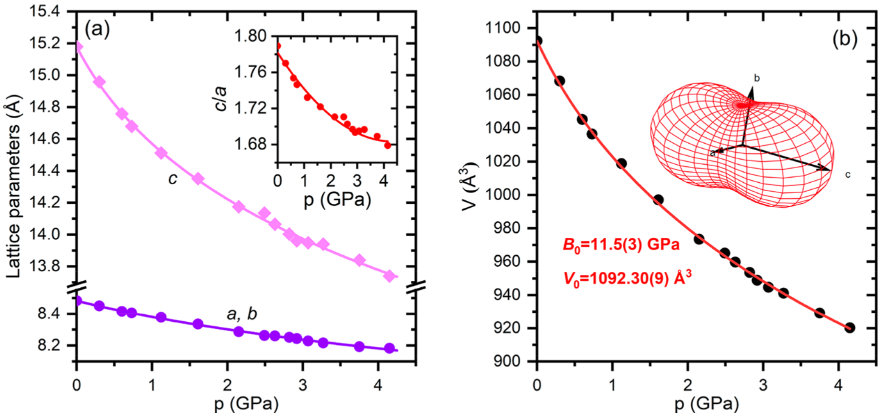

Figure 4. (a) Pressure dependence of the lattice parameters and (b) unit cell volume of $CsPb_2Br_5$. The lattice parameters and unit cell volume were fitted with the third-order Birch−Murnaghan EOS (solid lines). The inset in (b) shows the compressibility indicatrix calculated by using PASCAL software.[35]

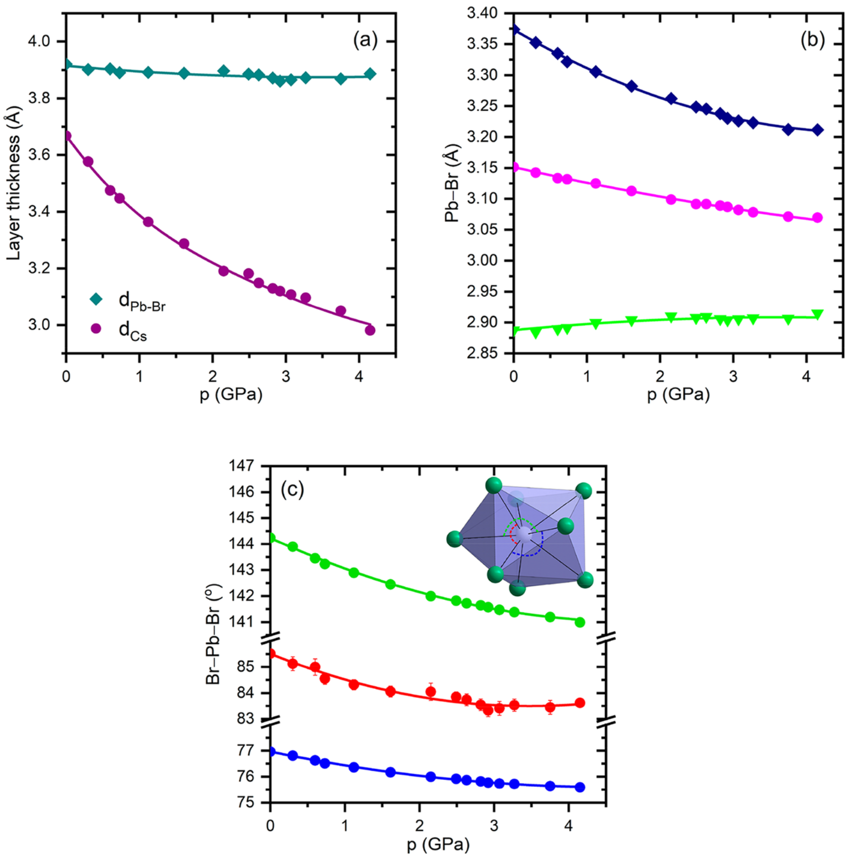

Figure 5. Pressure dependence of structural parameters in the compressed single crystal of $CsPb_2Br_5$: (a) the thickness of the Pb−Br and Cs layers, (b) the Pb−Br distances, and (c) the selected Br−Pb−Br angles; layers and Pb−Br distances are defined in Figure 1.

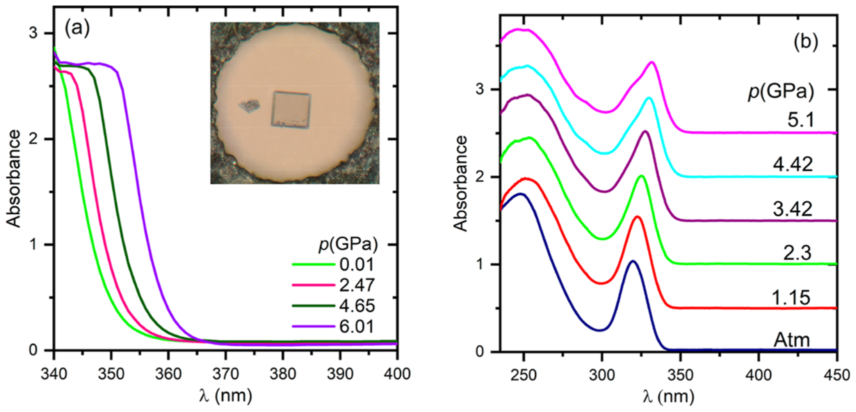

Figure 6. Selected absorption spectra of $CsPb_2Br_5$ recorded under different pressures: (a) for the 3.9 μm thick microplate and (b) for the 30 nm thick nanosheet. The inset shows the crystal in the DAC.

that the 3D perovskite $CsPbBr_3$ is less compressible than the layered $CsPb_2Br_5$. The inset in Figure 4b shows that the compressibility of $CsPb_2Br_5$ is strongly anisotropic, much higher along the c direction perpendicular to the layers than in the a−b plane. It should be noted that this anisotropy varies with increasing pressure, as indicated by the nonlinear decrease in the c/a ratio (see the inset plot in Figure 4a). The linear compressibility coefficients calculated at zero pressure β_a = 14.3(8) TPa^{-1} and β_c = 61(3) TPa^{-1} were used to determine independently the bulk modulus B_0 = 11.2(6) GPa. This value is in very good accordance with that derived from the fitting of the unit-cell volume. The low value of B_0 shows that $CsPb_2Br_5$ is relatively soft as for all-inorganic material. However, this is also characteristic for 3D organic−inorganic metal halide perovskites:[37,38] for example, for $CH_3NH_3SnI_3$, B_0 = 12.6(7) GPa; for $HC(NH_2)_2SnI_3$, B_0 = 8.0(7) GPa; and for $HC(NH_2)_2PbI_3$, B_0 = 11.0(2) GPa. The other important issue is the high value of B_0', which typically is close to 4 while for $CsPb_2Br_5$ it is raised to 9.3(6). This high value is justified by the layered character of the structure as similar values were reported; for example, for graphite-like BC, B_0' = 8.0(6),[39] and for layered $GeSe_2$, B_0' = 9.1(22).[40]

In the structure of $CsPb_2Br_5$ the layers built of the face-connected bicapped trigonal prisms $PbBr_8$ are more resistant to external hydrostatic pressure than the layers composed of Cs^+ cations. This is apparent in Figure 5a, where the changes in the

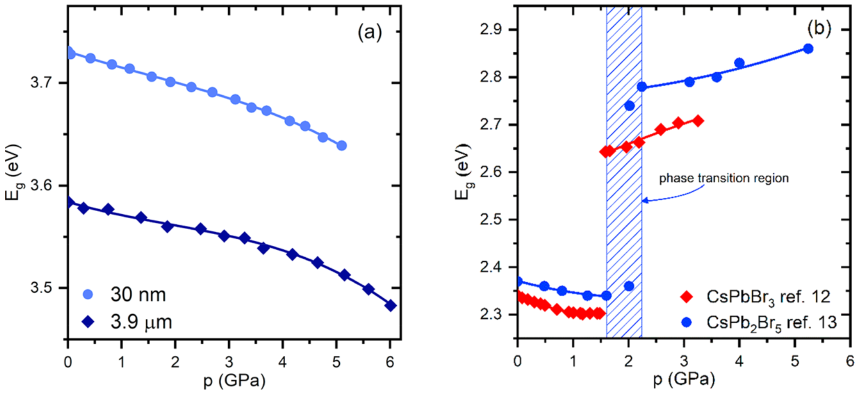

Figure 7. (a) Pressure-induced red shift of the band gap of $CsPb_2Br_5$ determined for two samples of different thickness in this work. (b) Comparison of the data reported in the literature for $CsPb_2Br_5$[13] with the results published for 3D $CsPbBr_3$.[12]

thickness of both layers are plotted as a function of pressure. In the Pb−Br layers, Pb^{2+} is coordinated by eight Br^- that form a polyhedron with three different Pb−Br distances (see Figure 1). At atmospheric pressure, these distances are strongly differentiated taking the values 3.374 Å (4×), 3.151 Å (2×), and 2.888 Å (2×). Similarly, their pressure dependences are also diversified. As shown in Figure 5b, with increasing pressure, the six longest Pb−Br bonds contract, while the two shortest bonds slightly elongate.

3.3. Absorption Edge and Energy Gap of Compressed $CsPb_2Br_5$.

The absorption spectra of $CsPb_2Br_5$ were measured under pressure on a single-crystal microplate and on a nanosheet during compression cycles. The selected spectra are plotted in Figure 6. As can be seen, for the 3.9 μm thick plate only the absorption edge is accessible, while the nanosheet spectrum is structured with a well-shaped excitonic band at 320−330 nm. The absorption onset is gradually red shifted with increasing pressure. To determine the energy gap, the absorption edges were converted to Tauc plots[41] (see Figure S6) by plotting $(\alpha h\nu)^2$ versus photon energy $h\nu$, where α is the absorption coefficient of the material. The values of E_g thus obtained are plotted as a function of pressure in Figure 7a. It is evident that the band gap of $CsPb_2Br_5$ decreases monotonically with increasing pressure, without any anomalies that could be attributed to phase transitions. The $E_g(p)$ dependence is linear in the pressure range to about 4 GPa, whereas under higher pressures, beyond the hydrostatic limit of isopropanol, some nonlinearity occurs. It is not clear whether this is an intrinsic feature of the crystal or the result of nonhydrostatic conditions, which can substantially affect the properties of materials.[42,43] The character of pressure-induced changes is the same regardless of the thickness of the samples, and the only difference is that for the thicker plate the obtained value of E_g is markedly lower, but such a relation can be expected for samples of substantially different thickness, as can be deduced from the plots in Figure S7.

In the studied pressure range of 6 GPa, the overall band gap reduction is about 0.1 eV. This relatively moderate change in E_g well correlates with the subtle changes in the thickness of the compressed Pb−Br layers (Figure 5a). The calculations of the electronic band structure indicate that the band gap in $CsPb_2Br_5$ has an indirect character, but the direct gap is only slightly larger.[7] The top valence bands are composed mainly of the Br−4p, Pb−6p and Pb−6s orbitals, while the Pb−6p and Br−4p orbitals dominantly contribute to the lowest conduction bands. The orbitals of Cs^+ cations do not contribute to the electronic states responsible for the absorption edge, and therefore the largest pressure effect, visible in Figure 5a as a remarkable narrowing of the Cs^+ layers, does not have a direct translation into the optical properties of the crystal. Thus, the band gap of $CsPb_2Br_5$ is mainly determined by the structure of Pb−Br layers and its modification under pressure. As shown in Figure 5b (see also Figure 1b), crystal compression results in contraction of the six longest Pb−Br distances, while the two shortest bonds slightly elongate. The shortening of Pb−Br bonds enhances the overlap of the atomic orbitals, leading to an upward shift of the maximum valence band and, as a consequence, to a red shift of the band gap. The opposite and therefore competitive effect comes from the Br−Pb−Br angles bending.[44] The relatively small changes observed in the angles (Figure 5c) indicate that the contraction of the Pb−Br bonds has a dominant influence on the modification of the electronic states responsible for the absorption edge.

In discussing the pressure dependence of E_g, we have to refer to the data reported by Ma et al.,[13] which are plotted for comparison in Figure 7b. It is obvious that our results are in stark contrast to those obtained by Ma et al. This applies to the pressure-induced changes in the band gap as well as to its value, which is even more important. To explain these discrepancies, we plotted in Figure 7b our recently published $E_g(p)$ results measured for 3D $CsPbBr_3$.[12] The correlation between these data and the results presented by Ma et al. is evident. Therefore, we conclude that they studied, in fact, the pressure dependence of the $CsPbBr_3$ band gap instead of $CsPb_2Br_5$. Most probably, their samples were strongly contaminated with $CsPbBr_3$, and their interpretation of the results seems to be even more puzzling when considering that the same group of authors had previously published two articles on the optical properties of $CsPbBr_3$ under pressure.[45,46]

4. CONCLUSIONS

This study confirms that green photoluminescence and absorption in the visible spectrum are not intrinsic features of $CsPb_2Br_5$ but originate from $CsPbBr_3$ impurities. The microcrystallites of the orange $CsPbBr_3$ do not form inclusions embedded in the crystal plates of $CsPb_2Br_5$ but precipitate on their surfaces. Therefore, we suppose that the majority of the literature data were in fact collected for the $CsPb_2Br_5$:$CsPbBr_3$ composites instead of $CsPb_2Br_5$. We show also that the commonly used diffuse reflectance method for the absorption edge and band gap determination gives optical parameters that are remarkably different from those obtained from the optical absorption measurements. This discrepancy indicates that the energies of the surface and bulk electronic states of $CsPb_2Br_5$ differ significantly, which may also be characteristic for other similar materials.

Pressure was applied as a clean and effective tool to modify the distances between the atoms and bond angles and thus the related electronic structure of $CsPb_2Br_5$. Although the compressibility of this 2D perovskite-like material is larger than that of 3D $CsPbBr_3$, the pressure-induced changes in the optical parameters are smaller. The layered architecture of $CsPb_2Br_5$ is reflected in a strongly anisotropic response to hydrostatic compression. The crystal shrinks much weaker in the a−b plane, i.e., parallel to the layers, than in perpendicular c direction. Furthermore, external mechanical stress affects the layers built of Cs^+ cations much more than the Pb−Br frameworks. The moderate changes within the Pb−Br layers translate into the moderate monotonic narrowing of the band gap with increasing pressure. Moreover, our study performed on the genuinely pure crystals has shown that the tetragonal structure of $CsPb_2Br_5$ is stable in a wide temperature range, at least between 90 and 625 K, and the crystal does not undergo any structural transformation in the pressure range up to 6 GPa. These results shed new light on the physical properties of $CsPb_2Br_5$ and show the interpretative pitfalls associated with the experiments performed carelessly.

■ ASSOCIATED CONTENT

Supporting Information

The Supporting Information is available free of charge at https://pubs.acs.org/doi/10.1021/acs.inorgchem.2c02253.

Selected crystallographic and refinement data, DSC and TGA results, figures illustrating experimental details, and plots illustrating a comparison to the literature data (PDF)

Accession Codes

CCDC 2176587−2176600 contain the supplementary crystallographic data for this paper. These data can be obtained free of charge via www.ccdc.cam.ac.uk/data_request/cif, or by emailing data_request@ccdc.cam.ac.uk, or by contacting The Cambridge Crystallographic Data Centre, 12 Union Road, Cambridge CB2 1EZ, UK; fax: +44 1223 336033.

■ AUTHOR INFORMATION

Corresponding Author

Marek Szafrański − *Faculty of Physics, Adam Mickiewicz University, 61-614 Poznań, Poland;* orcid.org/0000-0001-8178-5222; Email: masza@amu.edu.pl

Author

Viktoriia Drushliak − *Faculty of Physics, Adam Mickiewicz University, 61-614 Poznań, Poland;* orcid.org/0000-0003-1934-6370

Complete contact information is available at: https://pubs.acs.org/10.1021/acs.inorgchem.2c02253

Notes

The authors declare no competing financial interest.

■ ACKNOWLEDGMENTS

The authors are grateful for the financial support from the Polish National Science Centre, Grant Opus 16 No. 2018/31/B/ST3/02188. The authors also thank Prof. Marceli Koralewski for his help with the diffuse reflectance measurements and Dr. Maciej Wiesner for the determination of the crystals thickness using the AFM technique.

■ REFERENCES

(1) Tonui, P.; Oseni, S. O.; Sharma, G.; Yan, Q.; Tessema Mola, G. Perovskites Photovoltaic Solar Cells: An Overview of Current Status. *Renew. Sustain. Energy Rev.* **2018**, *91*, 1025−1044.

(2) Li, X.; Tan, Y.; Lai, H.; Li, S.; Chen, Y.; Li, S.; Xu, P.; Yang, J. All-Inorganic $CsPbBr_3$ Perovskite Solar Cells with 10.45% Efficiency by Evaporation-Assisted Deposition and Setting Intermediate Energy Levels. *ACS Appl. Mater. Interfaces* **2019**, *11*, 29746−29752.

(3) Wells, H. L. Uber Die Casium-Und Kalium-Bleihalogenide. *Z. Anorg. Allg. Chem.* **1893**, *3*, 195−210.

(4) Akkerman, Q. A.; Abdelhady, A. L.; Manna, L. Zero-Dimensional Cesium Lead Halides: History, Properties, and Challenges. *J. Phys. Chem. Lett.* **2018**, *9*, 2326−2337.

(5) Wang, K.-H.; Wu, L.; Li, L.; Yao, H.-B.; Qian, H.-S.; Yu, S.-H. Large-Scale Synthesis of Highly Luminescent Perovskite-Related $CsPb_2Br_5$ Nanoplatelets and Their Fast Anion Exchange. *Angew. Chem.* **2016**, *128*, 8468−8472.

(6) Qin, C.; Matsushima, T.; Sandanayaka, A. S. D.; Tsuchiya, Y.; Adachi, C. Centrifugal-Coated Quasi-Two-Dimensional Perovskite $CsPb_2Br_5$ Films for Efficient and Stable Light-Emitting Diodes. *J. Phys. Chem. Lett.* **2017**, *8*, 5415−5421.

(7) Tang, X.; Hu, Z.; Yuan, W.; Hu, W.; Shao, H.; Han, D.; Zheng, J.; Hao, J.; Zang, Z.; Du, J.; Leng, Y.; Fang, L.; Zhou, M. Perovskite $CsPb_2Br_5$ Microplate Laser with Enhanced Stability and Tunable Properties. *Adv. Opt. Mater.* **2017**, *5*, 1600788.

(8) Tang, X.; Han, S.; Zu, Z.; Hu, W.; Zhou, D.; Du, J.; Hu, Z.; Li, S.; Zang, Z. All-Inorganic Perovskite $CsPb_2Br_5$ Microsheets for Photodetector Application. *Front. Phys.* **2018**, *5*, 69.

(9) Wang, R.; Li, Z.; Li, S.; Wang, P.; Xiu, J.; Wei, G.; Liu, H.; Jiang, N.; Liu, Y.; Zhong, M. All-Inorganic Perovskite $CsPb_2Br_5$ Nanosheets for Photodetector Application Based on Rapid Growth in Aqueous Phase. *ACS Appl. Mater. Interfaces* **2020**, *12*, 41919−41931.

(10) Dursun, I.; de Bastiani, M.; Turedi, B.; Alamer, B.; Shkurenko, A.; Yin, J.; El-Zohry, A. M.; Gereige, I.; AlSaggaf, A.; Mohammed, O. F.; Eddaoudi, M.; Bakr, O. M. $CsPb_2Br_5$ Single Crystals: Synthesis and Characterization. *ChemSusChem* **2017**, *10*, 3746−3749.

(11) Nazarenko, O.; Kotyrba, M. R.; Wörle, M.; Cuervo-Reyes, E.; Yakunin, S.; Kovalenko, M. V. Luminescent and Photoconductive Layered Lead Halide Perovskite Compounds Comprising Mixtures of Cesium and Guanidinium Cations. *Inorg. Chem.* **2017**, *56*, 11552−11564.

(12) Szafrański, M.; Katrusiak, A.; Ståhl, K. Time-Dependent Transformation Routes of Perovskites $CsPbBr_3$ and $CsPbCl_3$ under High Pressure. *J. Mater. Chem. A* **2021**, *9*, 10769−10779.

(13) Ma, Z.; Li, F.; Qi, G.; Wang, L.; Liu, C.; Wang, K.; Xiao, G.; Zou, B. Structural Stability and Optical Properties of Two-Dimensional Perovskite-like $CsPb_2Br_5$ Microplates in Response to Pressure. *Nanoscale* **2019**, *11*, 820−825.

(14) Li, G.; Wang, H.; Zhu, Z.; Chang, Y.; Zhang, T.; Song, Z.; Jiang, Y. Shape and Phase Evolution from $CsPbBr_3$ Perovskite Nanocubes to Tetragonal $CsPb_2Br_5$ Nanosheets with an Indirect Bandgap. *Chem. Commun.* **2016**, *52*, 11296−11299.

(15) Zhang, Z.; Zhu, Y.; Wang, W.; Zheng, W.; Lin, R.; Huang, F. Growth, Characterization and Optoelectronic Applications of Pure-Phase Large-Area $CsPb_2Br_5$ Flake Single Crystals. *J. Mater. Chem. C* **2018**, *6*, 446−451.

(16) Li, J.; Zhang, H.; Wang, S.; Long, D.; Li, M.; Guo, Y.; Zhong, Z.; Wu, K.; Wang, D.; Zhang, T. Synthesis of All-Inorganic $CsPb_2Br_5$ Perovskite and Determination of Its Luminescence Mechanism. *RSC Adv.* **2017**, *7*, 54002−54007.

(17) Zhang, T.; Chen, Z.; Shi, Y.; Xu, Q. H. The Photoluminescence Mechanism of $CsPb_2Br_5$ Microplates Revealed by Spatially Resolved Single Particle Spectroscopy. *Nanoscale* **2019**, *11*, 3216−3221.

(18) Acharyya, P.; Pal, P.; Samanta, P. K.; Sarkar, A.; Pati, S. K.; Biswas, K. Single Pot Synthesis of Indirect Band Gap 2D $CsPb_2Br_5$ Nanosheets from Direct Band Gap 3D $CsPbBr_3$ Nanocrystals and the Origin of Their Luminescence Properties. *Nanoscale* **2019**, *11*, 4025−4034.

(19) Zhou, Y. Q.; Xu, J.; Liu, J. B.; Liu, B. X. Green Emission Induced by Intrinsic Defects in All-Inorganic Perovskite $CsPb_2Br_5$. *J. Phys. Chem. Lett.* **2019**, *10*, 6118−6123.

(20) Merrill, L.; Bassett, W. A. Miniature Diamond Anvil Pressure Cell for Single Crystal X-ray Diffraction Studies. *Rev. Sci. Instrum.* **1974**, *45*, 290−294.

(21) Piermarini, G. J.; Block, S.; Barnett, J. D. Hydrostatic Limits in Liquids and Solids to 100 kbar. *J. Appl. Phys.* **1973**, *44*, 5377−5382.

(22) Piermarini, G. J.; Block, S.; Barnett, J. D.; Forman, R. A. Calibration of the Pressure Dependence of the R_1 Ruby Fluorescence Line to 195 kbar. *J. Appl. Phys.* **1975**, *46*, 2774−2780.

(23) Agilent Technologies. CrysAlisPro: Data Collection and Processing Software for X-Ray Diffractometers, Santa Clara, CA, 2010.

(24) Sheldrick, G. M. A Short History of SHELX. *Acta Crystallogr. A* **2008**, *64*, 112−122.

(25) Zhang, X.; Xu, B.; Zhang, J.; Gao, Y.; Zheng, Y.; Wang, K.; Sun, X. W. All-Inorganic Perovskite Nanocrystals for High-Efficiency Light Emitting Diodes: Dual-Phase $CsPbBr_3$-$CsPb_2Br_5$ Composites. *Adv. Funct. Mater.* **2016**, *26*, 4595−4600.

(26) Turedi, B.; Lee, K. J.; Dursun, I.; Alamer, B.; Wu, Z.; Alarousu, E.; Mohammed, O. F.; Cho, N.; Bakr, O. M. Water-Induced Dimensionality Reduction in Metal-Halide Perovskites. *J. Phys. Chem. C* **2018**, *122*, 14128−14134.

(27) Yin, J.; Zhang, G.; Tao, X. A Fractional Crystallization Technique towards Pure Mega-Size $CsPb_2Br_5$ Single Crystal Films. *CrystEngComm* **2019**, *21*, 1352−1357.

(28) Murugadoss, G.; Thangamuthu, R.; Senthil Kumar, S. M.; Anandhan, N.; Rajesh Kumar, M.; Rathishkumar, A. Synthesis of Ligand-Free, Large Scale with High Quality All-Inorganic $CsPbI_3$ and $CsPb_2Br_5$ Nanocrystals and Fabrication of All-Inorganic Perovskite Solar Cells. *J. Alloys Compd.* **2019**, *787*, 17−26.

(29) Cola, M.; Massarotti, V.; Riccardi, R.; Sinistri, C. Binary Systems Formed by Lead Bromide with (Li, Na, K, Rb, Cs and Tl)Br: A DTA and Diffractometric Study. *Z. Naturforsch.* **1971**, *26*, 1328−1332.

(30) Rodová, M.; Brožek, J.; Knížek, K.; Nitsch, K. Phase Transitions in Ternary Caesium Lead Bromide. *J. Therm. Anal. Calorim.* **2003**, *71*, 667−673.

(31) Kubelka, P.; Munk, F. Ein Beitrag Zur Optik Der Farbanstriche. *Z. Technol. Physik* **1931**, *12*, 593−601.

(32) Chen, X.; Lu, H.; Yang, Y.; Beard, M. C. Excitonic Effects in Methylammonium Lead Halide Perovskites. *J. Phys. Chem. Lett.* **2018**, *9*, 2595−2603.

(33) Birch, F. Finite Elastic Strain of Cubic Crystals. *Phys. Rev.* **1947**, *71*, 809−824.

(34) Gonzalez-Platas, J.; Alvaro, M.; Nestola, F.; Angel, R. EosFit7-GUI: A New Graphical User Interface for Equation of State Calculations, Analyses and Teaching. *J. Appl. Crystallogr.* **2016**, *49*, 1377−1382.

(35) Cliffe, M. J.; Goodwin, A. L. PASCal: A Principal Axis Strain Calculator for Thermal Expansion and Compressibility Determination. *J. Appl. Crystallogr.* **2012**, *45*, 1321−1329.

(36) Anzellini, S.; Burakovsky, L.; Turnbull, R.; Bandiello, E.; Errandonea, D. P-V-T Equation of State of Iridium Up to 80 GPa and 3100 K. *Crystals* **2021**, *11*, 452.

(37) Lee, Y.; Mitzi, D. B.; Barnes, P. W.; Vogt, T. Pressure-Induced Phase Transitions and Templating Effect in Three-Dimensional Organic-Inorganic Hybrid Perovskites. *Phys. Rev. B* **2003**, *68*, No. 020103(R).

(38) Liu, G.; Kong, L.; Gong, J.; Yang, W.; Mao, H. K.; Hu, Q.; Liu, Z.; Schaller, R. D.; Zhang, D.; Xu, T. Pressure-Induced Bandgap Optimization in Lead-Based Perovskites with Prolonged Carrier Lifetime and Ambient Retainability. *Adv. Funct. Mater.* **2017**, *27*, 1604208.

(39) Solozhenko, V. L.; Kurakevych, O. O.; Solozhenko, E. G.; Chen, J.; Parise, J. B. Equation of State of Graphite-like BC. *Solid State Commun.* **2006**, *137*, 268−271.

(40) Stølen, S; Grzechnik, A; Grande, T; Mezouar, M Anisotropic Compressibility and Expansivity in Layered $GeSe_2$. *Solid State Commun.* **2000**, *115*, 249−252.

(41) Tauc, J.; Grigorovici, R.; Vancu, A. Optical Properties and Electronic Structure of Amorphous Germanium. *Phys. Status Solidi B* **1966**, *15*, 627−637.

(42) Zhang, R.; Cai, W.; Bi, T.; Zarifi, N.; Terpstra, T.; Zhang, C.; Verdeny, Z. V.; Zurek, E.; Deemyad, S. Effects of Nonhydrostatic Stress on Structural and Optoelectronic Properties of Methylammonium Lead Bromide Perovskite. *J. Phys. Chem. Lett.* **2017**, *8*, 3457−3465.

(43) Errandonea, D.; Meng, Y.; Somayazulu, M.; Häusermann, D. Pressure-Induced $\alpha \rightarrow \omega$ Transition in Titanium Metal: A Systematic Study of the Effects of Uniaxial Stress. *Physica B* **2005**, *355*, 116−125.

(44) Kong, L.; Liu, G.; Gong, J.; Hu, Q.; Schaller, R. D.; Dera, P.; Zhang, D.; Liu, Z.; Yang, W.; Zhu, K.; Tang, Y.; Wang, C.; Wei, S.-H.; Xu, T.; Mao, H.-k. Simultaneous Band-Gap Narrowing and Carrier-Lifetime Prolongation of Organic-Inorganic Trihalide Perovskites. *Proc. Natl. Acad. Sci. U. S. A.* **2016**, *113*, 8910−8915.

(45) Zhang, L.; Zeng, Q.; Wang, K. Pressure-Induced Structural and Optical Properties of Inorganic Halide Perovskite $CsPbBr_3$. *J. Phys. Chem. Lett.* **2017**, *8*, 3752−3758.

(46) Xiao, G.; Cao, Y.; Qi, G.; Wang, L.; Liu, C.; Ma, Z.; Yang, X.; Sui, Y.; Zheng, W.; Zou, B. Pressure Effects on Structure and Optical Properties in Cesium Lead Bromide Perovskite Nanocrystals. *J. Am. Chem. Soc.* **2017**, *139*, 10087−10094.

Supporting Information

Thermodynamic Stability, Structure and Optical Properties of Perovskite-Related $CsPb_2Br_5$ Single Crystals Under Pressure

Viktoriia Drushliak and Marek Szafrański*

Faculty of Physics, Adam Mickiewicz University, Uniwersytetu Poznańskiego 2, 61-614 Poznań,

Poland

Corresponding author e-mail: masza@amu.edu.pl

Table S1. Selected crystallographic and refinement data for the structures of $CsPb_2Br_5$.

Crystal formula	$CsPb_2Br_5$					
Crystal system	Tetragonal					
Space group	*I*4/*mcm*					
Z	4					
Pressure (GPa)	0.0001	0.73	1.12	2.15	3.07	3.75
Crystal size (mm)	0.16 × 0.12 × 0.09	0.21 × 0.21 × 0.03	0.23 × 0.15 × 0.02	0.21 × 0.21 × 0.03	0.23 × 0.15 × 0.02	0.23 × 0.15 × 0.02
a,b (Å)	8.4831 (1)	8.4043(7)	8.3789 (4)	8.2869 (3)	8.2293 (6)	8.1935 (9)
c (Å)	15.1786 (3)	14. 675(2)	14.512 (12)	14.175 (14)	13.949 (13)	13.84 (2)
Volume (Å^3)	1092.30 (3)	1036.5(2)	1018.9 (8)	973.4 (10)	944.7 (9)	929.1 (15)
ρ (g cm^{-3})	5.758	6.068	6.173	6.461	6.658	6.769
μ (mm^{-1})	52.25	55.10	56.06	58.67	60.46	61.47
No. of measured, independent and observed [$I > 2\sigma(I)$] reflections	6625, 451, 433	2200, 207, 165	2178, 134, 133	2146, 117, 108	2282, 136, 128	2233, 137, 130
R_{int}	0.055	0.066	0.078	0.103	0.094	0.091
R_1 [$I > 2\sigma(I)$], $R_1(all)$	0.020, 0.021	0.034, 0.048	0.024, 0.024	0.022, 0.028	0.032, 0.035	0.029, 0.030
wR_2 [$I > 2\sigma(I)$], $wR_2\,(all)$	0.086, 0.088	0.081, 0.084	0.060, 0.060	0.057, 0.058	0.082, 0.084	0.071, 0.072
S	0.756	1.151	1.273	1.354	1.250	1.207

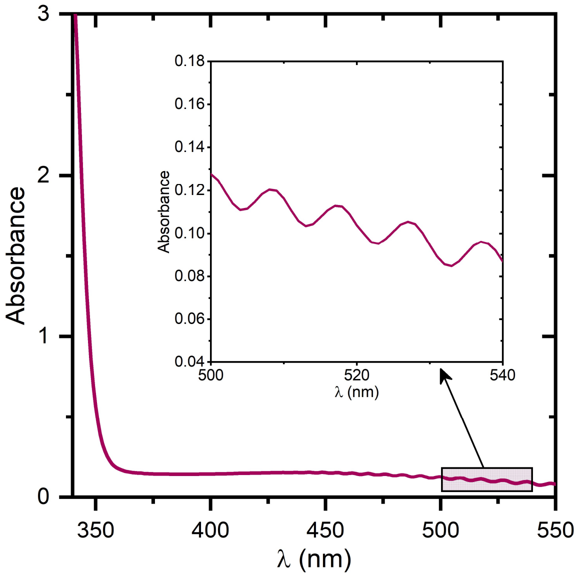

Figure S1. Interference fringes observed outside the absorption region of the $CsPb_2Br_5$ crystal plate. The positions of the interference maxima/minima were used to determine the thickness of the crystal.

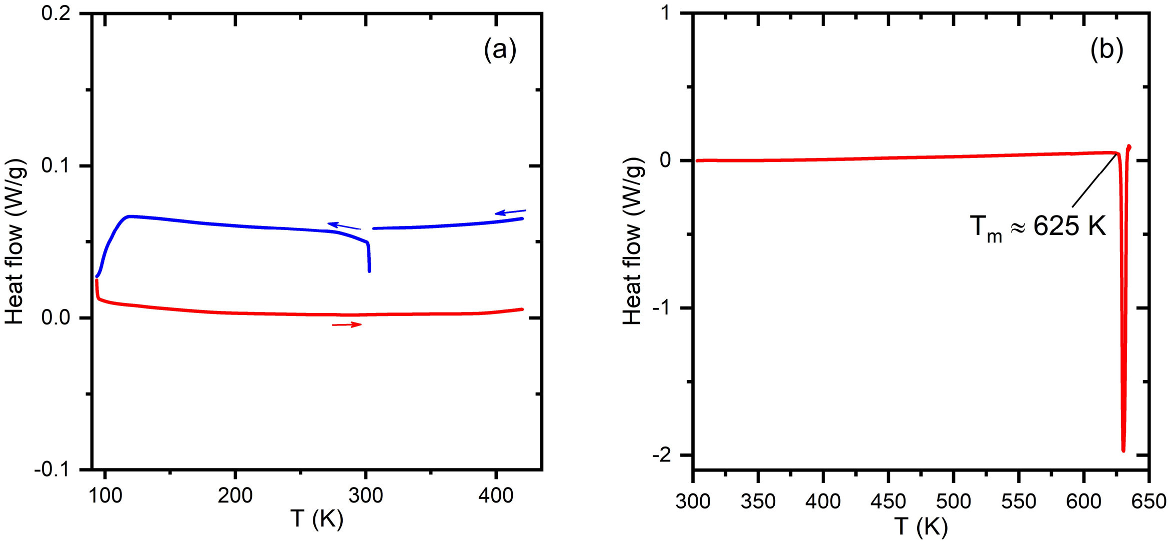

Figure S2. DSC runs recorded for $CsPb_2Br_5$ in the temperature range 95–420 K (a) and in the high-temperature range close to the melting point (b). The temperature was varied at a rate of 10 $Kmin^{-1}$.

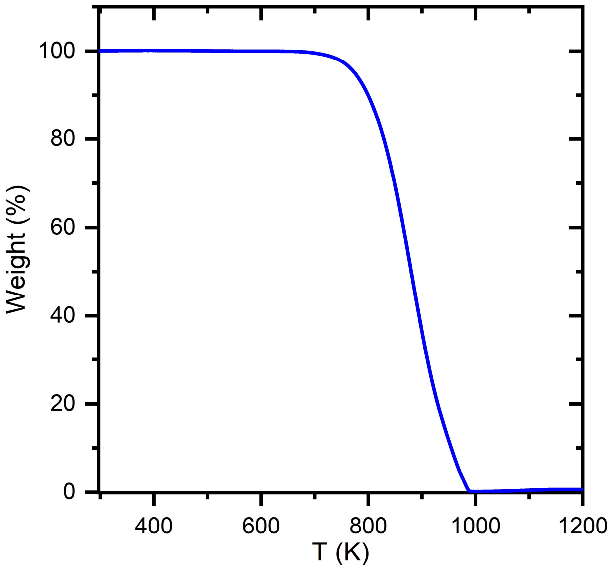

Figure S3. TGA curve for powdered $CsPb_2Br_5$ measured at a rate of 10 Kmin^{-1}.

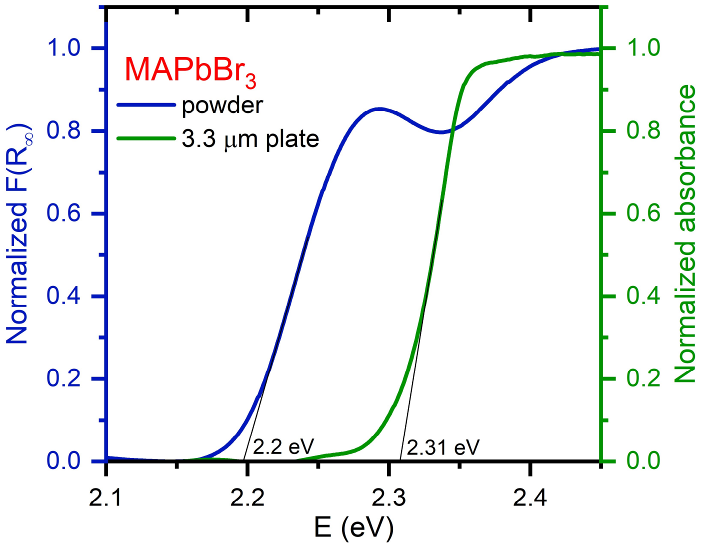

Figure S4. Comparison of the absorption and diffuse reflectance spectra for the methylammonium lead tribromide, $MAPbBr_3$.

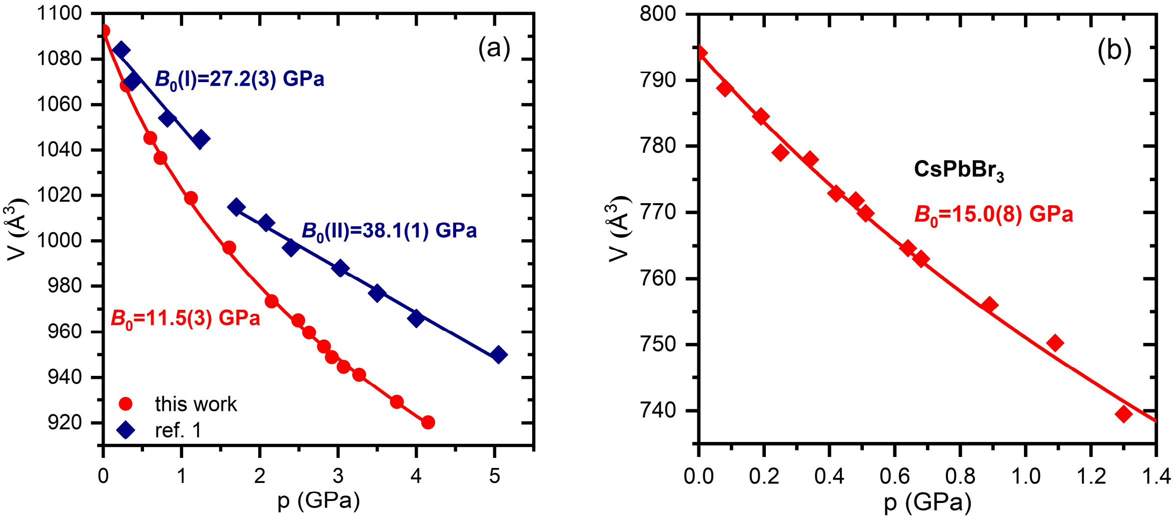

Figure S5. (a) Pressure dependence of the unit cell volume of $CsPb_2Br_5$ determined in this work from the single-crystal X-ray diffraction and compared to the literature data measured by powder diffraction.[1] The solid lines correspond to the fitted equation of states. (b) The literature $V(p)$ data[2] fitted with the second-order Birch-Murnaghan equation of state.

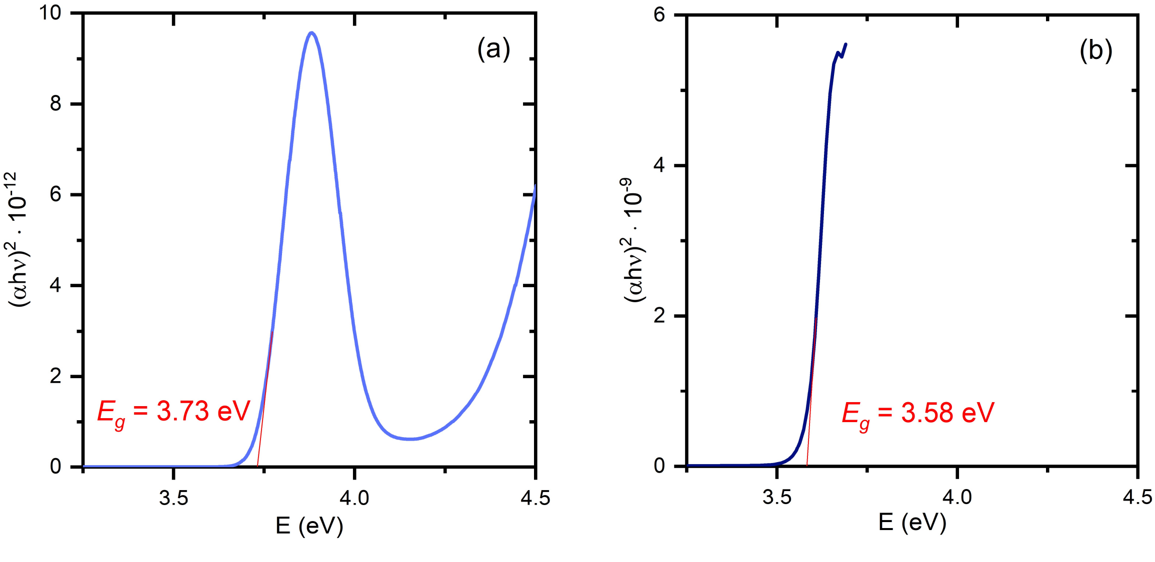

Figure S6. Tauc plots[3] and energy gaps determined from the absorption spectra measured for the 30 nm (a) and 3.9 μm (b) thick $CsPb_2Br_5$ plates.

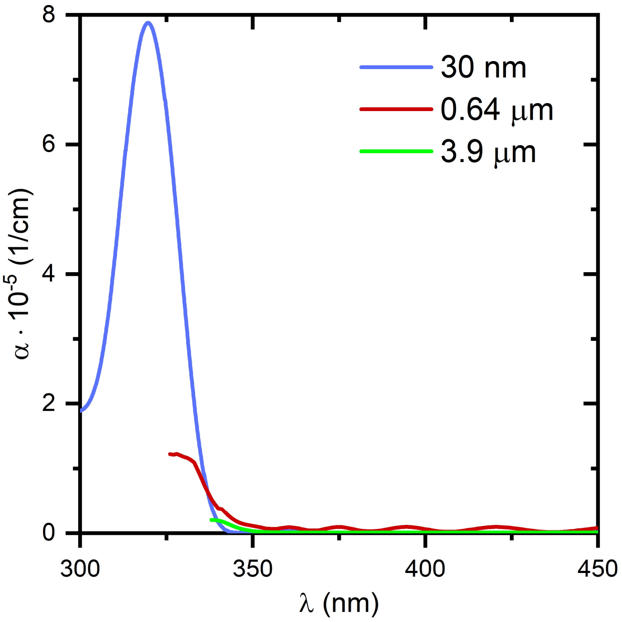

Figure S7. Absorption spectra of $CsPb_2Br_5$ measured for the plates of different thickness.

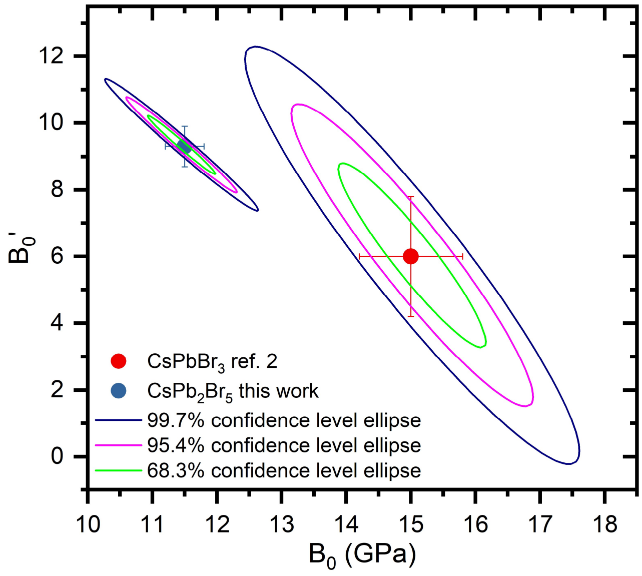

Figure S8. Values B_0' plotted versus B_0 for $CsPb_2Br_5$ and $CsPbBr_3$. The different confidence level ellipses are shown.

REFERENCES

(1) Ma, Z.; Li, F.; Qi, G.; Wang, L.; Liu, C.; Wang, K.; Xiao, G.; Zou, B. Structural Stability and Optical Properties of Two-Dimensional Perovskite-like $CsPb_2Br_5$ Microplates in Response to Pressure. *Nanoscale* **2019**, *11*, 820–825.

(2) Szafrański, M.; Katrusiak, A.; Ståhl, K. Time-Dependent Transformation Routes of Perovskites $CsPbBr_3$ and $CsPbCl_3$ under High Pressure. *J. Mater. Chem. A* **2021**, *9*, 10769–10779.

(3) Tauc, J.; Grigorovici, R.; Vancu, A. Optical Properties and Electronic Structure of Amorphous Germanium. *Phys. Status Solidi B* **1966**, *15*, 627–637.

Journal of
Materials Chemistry C

ROYAL SOCIETY
OF CHEMISTRY

PAPER

Check for updates

Cite this: J. Mater. Chem. C, 2024, 12, 4360

White-light emission triggered by pseudo Jahn–Teller distortion at the pressure-induced phase transition in Cs_4PbBr_6†

Viktoriia Drushliak, Konrad J. Kapcia and Marek Szafrański*

Received 4th January 2024,
Accepted 19th February 2024

DOI: 10.1039/d4tc00036f

rsc.li/materials-c

The zero-dimensional all-inorganic perovskite Cs_4PbBr_6 has been studied under pressure by single-crystal X-ray diffraction, optical absorption, and photoluminescence. The analysis of the experimental results has been supported by calculations of the electronic band structure. The crystal undergoes a sequence of two first-order pressure-induced phase transitions at 2.6 and 3.2 GPa with the space group changes $R\bar{3}c \rightarrow Cmce \rightarrow I4/mnc$, which contradicts the previously reported transition $R\bar{3}c \rightarrow B2/b$. Under compression, the crystal bandgap progressively narrows across the three phases, and in a jumpwise manner at the transition points, leading to an overall decrease of the energy gap by more than 0.5 eV at 4.2 GPa. The pressure evolution of the bandgap perfectly correlates with the electronic band structure changes modelled by first-principles calculations using the pressure-dependent structural data. Our structural study revealed an unprecedented pressure-induced increase in the volume of $PbBr_6$ octahedra, by more than 5%, upon the transition to the tetragonal phase. This distortion, associated with the shortening of two and the lengthening of four Pb–Br distances, has been attributed to the pseudo Jahn–Teller (PJT) effect. Thus, the pressure-induced white-light emission that occurs upon the transition to the tetragonal phase is evidently induced by the PJT distortion.

Introduction

Metal halide perovskites are one of the hottest topics in materials science because of their great potential for photovoltaic, optoelectronic, and multifunctional applications.[1,2] The outstanding properties of these materials, including high optical absorption coefficients and long diffusion lengths of charge carriers, are crucial for the high quantum efficiency of solar cells and light-emitting devices.[1,3,4] A classical metal halide perovskite structure AMX_3 (M is a divalent metal and X = Cl, Br or I) consists of MX_6 octahedra forming a corner-sharing framework where the cuboctahedral voids are occupied by the A-site organic or inorganic cations.[5] However, there are also numerous low-dimensional perovskite-related materials that have attracted considerable interest in recent years.[6–9] With decreasing dimensionality, the MX_6 octahedra are less connected, and ultimately, in the so-called zero-dimensional (0D) perovskites, they become isolated.[9] This leads to a strong localization of the electronic states responsible for the optical properties of these materials. A typical 0D metal halide perovskite is Cs_4PbBr_6 which has been intensely studied due to the strong and stable green photoluminescence (PL) of the quantum yield much higher than that of $CsPbBr_3$.[10–12] The absorption edge in the visible range and the green emission have often been attributed to the intrinsic properties of Cs_4PbBr_6 or Br vacancy defects.[10–19] However, the extensive debate on this topic led to the conclusion that pure Cs_4PbBr_6 crystals do not show any PL under ambient conditions, while green PL is due to the $CsPbBr_3$ inclusions.[8,20] The Br vacancies have been excluded as possible green luminescence centres by the combined Raman and PL high-pressure study.[21]

Interestingly, a broad emission band induced by pressure was reported for Cs_4PbBr_6 nanocrystals.[22] It is worth noting that in the case of 0D Cs_4PbBr_6, the size effects should be negligible because the optical properties of this material are governed by isolated molecular-like octahedra. Therefore, similar pressure effects can be expected for both bulk crystals and nanocrystals. Moreover, in the aforementioned high-pressure study, the 355 nm excitation laser line was used while the ambient-pressure absorption edge of Cs_4PbBr_6 is located below 340 nm. It is obvious that under these specific experimental conditions, excitation is unattainable, making luminescence impossible, regardless of the material properties. Under pressure, the absorption edge redshifts, but only at around 3 GPa can the absorption of the excitation light be effective. These conditions coincide with the onset of the white-light emission[22]

Faculty of Physics, Adam Mickiewicz University, Uniwersytetu Poznańskiego 2, 61-614 Poznań, Poland. E-mail: masza@amu.edu.pl

† Electronic supplementary information (ESI) available. CCDC 2313400–2313420. For ESI and crystallographic data in CIF or other electronic format see DOI: https://doi.org/10.1039/d4tc00036f

and therefore the question arises of whether this is a pressure-induced effect or just the result of tuning the absorption spectrum to the excitation line. Furthermore, silicon oil, which ensures hydrostatic conditions to 1 GPa at most, appears not to be the best choice for the pressure-transmitting medium in the case where the phenomenon studied occurs above 3 GPa. The unexpected emission has been associated with the phase transition between the rhombohedral phase I (space group $R\bar{3}c$) and monoclinic phase II (space group $B2/b$) as inferred from the powder X-ray diffraction patterns.[22]

In the paper published by Wells in 1893,[23] Cs_4PbBr_6 was described as a colourless substance, whereas most of the recent studies have been carried out on the green form, and also crystallization of the yellow crystals was reported,[24] although they were not characterized. In this study we obtained the three forms of Cs_4PbBr_6 and compared their optical and structural properties. The previously observed pressure-induced structural phase transition of Cs_4PbBr_6 has been re-examined by single crystal X-ray diffraction (SCXRD) up to 4.6 GPa, under genuinely hydrostatic conditions to exclude the influence of deviatoric stress, which occurs in the diamond anvil cell (DAC) when the pressure is nonhydrostatic. Our study did not confirm the rhombohedral to monoclinic phase transition, but instead we disclosed a sequence of two successive structural transitions at *ca.* 2.6 and 3.2 GPa. These transitions were confirmed by spectroscopic experiments. The detailed structural information derived from the single-crystal measurements sheds new light on the profound changes in the optical properties of the crystal.

Materials and methods

In the first step, CsBr was obtained by reacting Cs_2CO_3 (Aldrich, 99%) and HBr (Acros Organics, 48% water solution) in an aqueous solution. Cs_4PbBr_6 was synthesized by mixing stoichiometric amounts of CsBr dissolved in water and $PbBr_2$ dissolved in HBr. To dissolve the precipitate formed during this synthesis, DMF (*N*,*N*-dimethylformamide, Eurochem, grade for analysis) was successively added to the heated solution (70–100 °C) with constant stirring until the solution became completely transparent. Then the solution was left for slow cooling and crystallization. Because of the different evaporation rates of HBr, H_2O and DMF, with the dissolution process usually lasting 2–3 hours, full control of the crystallization conditions was hindered. The crystallization procedure repeated several times yielded colourless, green and yellow crystals of Cs_4PbBr_6. We observed that different kinds of crystals, for example green and colourless, could be formed even from the solution in the same beaker. Therefore, it seems that the crystallization process of different forms of Cs_4PbBr_6 depends not only on the solution composition, but also factors such as the temperature and rate of crystallization can be crucial.

X-ray diffraction under high pressure

For high-pressure X-ray diffraction experiments a single crystal of Cs_4PbBr_6 was mounted in a modified Merrill-Bassett DAC[25] equipped with symmetric diamond anvils (culet diameter 0.8 mm) supported on steel discs with conical windows. The gasket was made of a 250 μm thick steel foil in which a spark-eroded hole of 350–380 μm in diameter was made. Isopropanol was used as a hydrostatic liquid. The pressure was calibrated on the basis of the ruby fluorescence line displacement,[26] with an accuracy better than 0.03 GPa. SCXRD data were collected using a four-circle Oxford Diffraction Gemini A Ultra diffractometer operating with a graphite-monochromated Mo Kα radiation source (λ = 0.71073 Å). The cell was centered by the gasket-shadowing method.[27] Data were collected and processed using CrysAlisPro software.[28] The crystal structures were solved and refined using SHELX programs.[29] The selected structural and refinement details are collected in Table S1 (ESI†) while full crystallographic information files have been submitted to the inorganic crystal structure database with numbers 2313400–2313420.†

High-pressure optical absorption and photoluminescence

A modified Merrill-Bassett DAC equipped with low-fluorescence type IIa diamond anvils was used for optical measurements. The pressure chamber containing the sample and ruby chip was filled with Daphne Oil 7575, which ensured hydrostatic conditions to about 4 GPa.[30,31] Absorption spectra were collected using a Jasco MSV-5100 microscopic spectrophotometer. The absorbance was measured from the small sample area of 30 μm in diameter, at a scan speed 200 nm min^{-1} and a spectral bandwidth of 5 nm, in the range 230–600 nm.

PL measurements were carried out with a homemade attachment to the Jasco MSV-5100. A xenon lamp with two kinds of UV filters served as an excitation source in the spectral range 250–320 or 320–500 nm. The light emitted by the single-crystal sample was analyzed with a Spectra Academy SV2100 spectrometer.

The absorption and PL spectra were measured at room temperature.

First-principles calculations

The first-principles calculations were performed using the projector augmented wave (PAW) potentials[32] and the generalized gradient approximation (GGA) in the Perdew, Burke, and Ernzerhof (PBE) parametrization.[33] We have used the VASP code,[34–36] and the calculations were based on the stoichiometric structures of Cs_4PbBr_6 obtained from the diffraction experiments. The simulations were performed for the trigonal, orthorhombic and tetragonal structures using respective primitive cells consisting of two formula units (22 atoms) for every phase. We included four valence electrons for Pb atoms ($6s^2$ $6p^2$), nine for Cs atoms ($5s^2$ $5p^6$ $6s^1$), and seven for Br atoms ($4s^2$ $4p^5$). A plane wave energy cutoff of 300 eV was used. The energy convergence criterium was set at 10^{-8} for electronic iterations. For the summation over the reciprocal space, we used a 12 × 12 × 12 Monkhorst–Pack *k*-point grid.[37] The characteristic points in the first Brillouin zone were determined using the SeeK-path tool.[38,39] The spin–orbit coupling was not included in the calculations.

Results

Characteristics of the crystals grown

The single crystals of three Cs_4PbBr_6 forms grown from H_2O:DMF solutions are shown in Fig. 1a. On average the crystals size was about 0.1 mm. The colourless form A does not exhibit PL in the visible range, while green light is evidently emitted under UV irradiation of the coloured forms B and C (Fig. 1b). Our optical measurements show that these three forms are characterized by different absorption and PL spectra, as illustrated in Fig. 1c and d, where, for comparison, we also plotted the spectra of $CsPbBr_3$. The colourless crystals exhibit a strong excitonic absorption band centered at 315 nm which is characteristic of Cs_4PbBr_6,[20] and do not absorb or emit light in the visible range. Therefore, we conclude that this is a pure form of Cs_4PbBr_6 without inclusions of $CsPbBr_3$. The yellow and green forms, apart from the strong absorption at 315 nm also absorb light in the visible range below 530 nm, indicating an admixture of 3D $CsPbBr_3$.[40–42] Both the strongest visible light absorption and the highest PL intensity testify that yellow crystals contain the highest density of inclusions. The single crystal of $CsPbBr_3$ shows a much lower PL intensity compared to $CsPbBr_3$ nanocrystals dispersed in the Cs_4PbBr_6 matrix. This is probably due to strong PL quenching in bulk crystals, which is related to the low binding energy of excitons in the 3D perovskite.[12] It should also be noted that the location of the PL peak clearly depends on the concentration of $CsPbBr_3$. For bulk $CsPbBr_3$ the PL peak is centered at 531 nm, while for yellow and green crystals it occurs at 527 nm and 519 nm, respectively.

The determination of the structure of the colourless and yellow Cs_4PbBr_6 crystals by SCXRD under ambient conditions confirmed the trigonal space group $R\bar{3}c$ of both forms, consistent with previous reports.[13,43] No structural differences were found between the pure crystal and that with $CsPbBr_3$ inclusions, and also their unit-cell dimensions are very similar (Table S2, ESI†). This indicates that the nano-sized islands of $CsPbBr_3$, embedded in the matrix of Cs_4PbBr_6, do not distort the host lattice very much. It is also interesting that the influence of the host network on the properties of the $CsPbBr_3$ inclusions under high pressure seems to be minor. This is

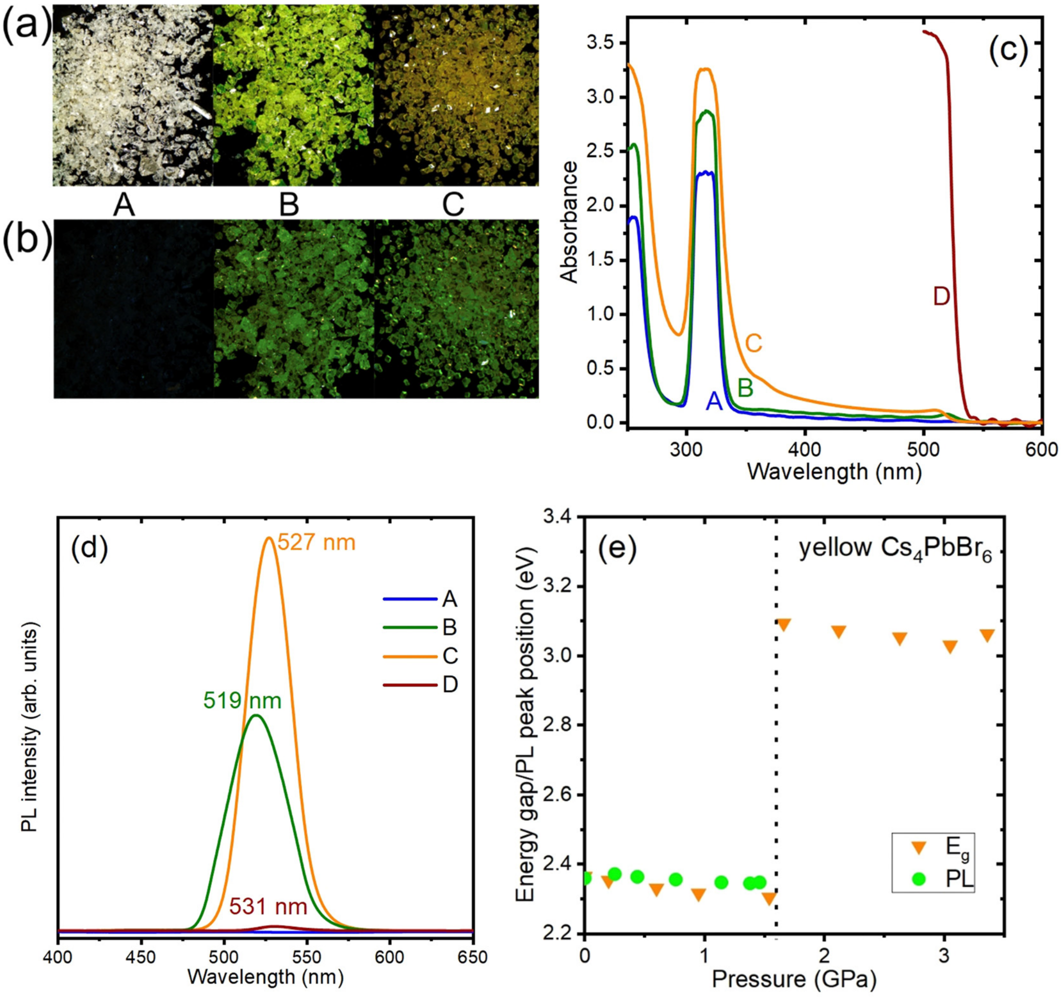

Fig. 1 Photographs of three types of Cs_4PbBr_6 crystals (A-colourless, B-green, C-yellow) under white light (a) and UV (b) illumination, the comparison of their optical absorption (c) and emission (d) spectra with those of $CsPbBr_3$ (D), and the pressure dependence of the energy gap and green PL peak position of the yellow form (e). The thickness of the samples: A - 1.7 μm, B - 2.8 μm, C - 4.7 μm, D - 3 μm.

evidenced by the pressure study of the absorption and green PL, performed for the yellow form of the Cs_4PbBr_6 crystals. The absorption edge, observed under atmospheric pressure at around 520 nm (see curve C in Fig. 1c), was monitored as a function of pressure and the corresponding energy gap was determined. As shown in Fig. 1e, at around 1.5 GPa the energy gap sharply increases, indicating a first-order phase transition. Both the value of the energy gap, its pressure behaviour, and the transition pressure, are in very good agreement with the results obtained earlier for bulk crystals of $CsPbBr_3$.[42] Moreover, the disappearance of green PL after the transition to the high-pressure phase is in excellent accordance with the similar observations reported for $CsPbBr_3$.[44] Thus, it is evident that the pressure-induced phase transition occurs in the $CsPbBr_3$ crystallites embedded in the host matrix of Cs_4PbBr_6, which is consistent with the earlier study.[21]

Pressure-induced changes in the structure of Cs_4PbBr_6

High-pressure X-ray diffraction data was collected on the pure high-quality Cs_4PbBr_6 crystals in the pressure range up to 4.6 GPa. The pressure dependences of the unit-cell dimensions and volume, as shown in Fig. 2a and b, indicate two first-order phase transitions at about 2.6 and 3.2 GPa. The three phases of the crystal are denoted by Roman numbers starting from the ambient-pressure trigonal phase I of the space group $R\bar{3}c$. In intermediate phase II the crystal symmetry changes to the orthorhombic space group *Cmce*, whereas the high-pressure phase III is tetragonal with the space group symmetry $P4/mnc$. The structural motif of isolated $PbBr_6$ octahedra surrounded by Cs^+ cations is preserved in all phases, but the arrangement of the octahedra is distinctly different, as illustrated in Fig. 3. The transformations of the unit cell at the phase transitions are shown in Fig. 4. The fitting of the experimental data $V(T)$ measured in phase I using the third-order Birch–Murnaghan equation of state (B–M EoS)[45] resulted in a bulk modulus B_0 = 10.5(7) GPa and its derivative B_0' = 9.7(16). These parameters are comparable to those reported recently for 2D $CsPb_2Br_5$ [B_0 = 11.5(3) GPa and B_0' = 9.3(6)][46] indicating similar compressibility of both materials, which are substantially softer than 3D

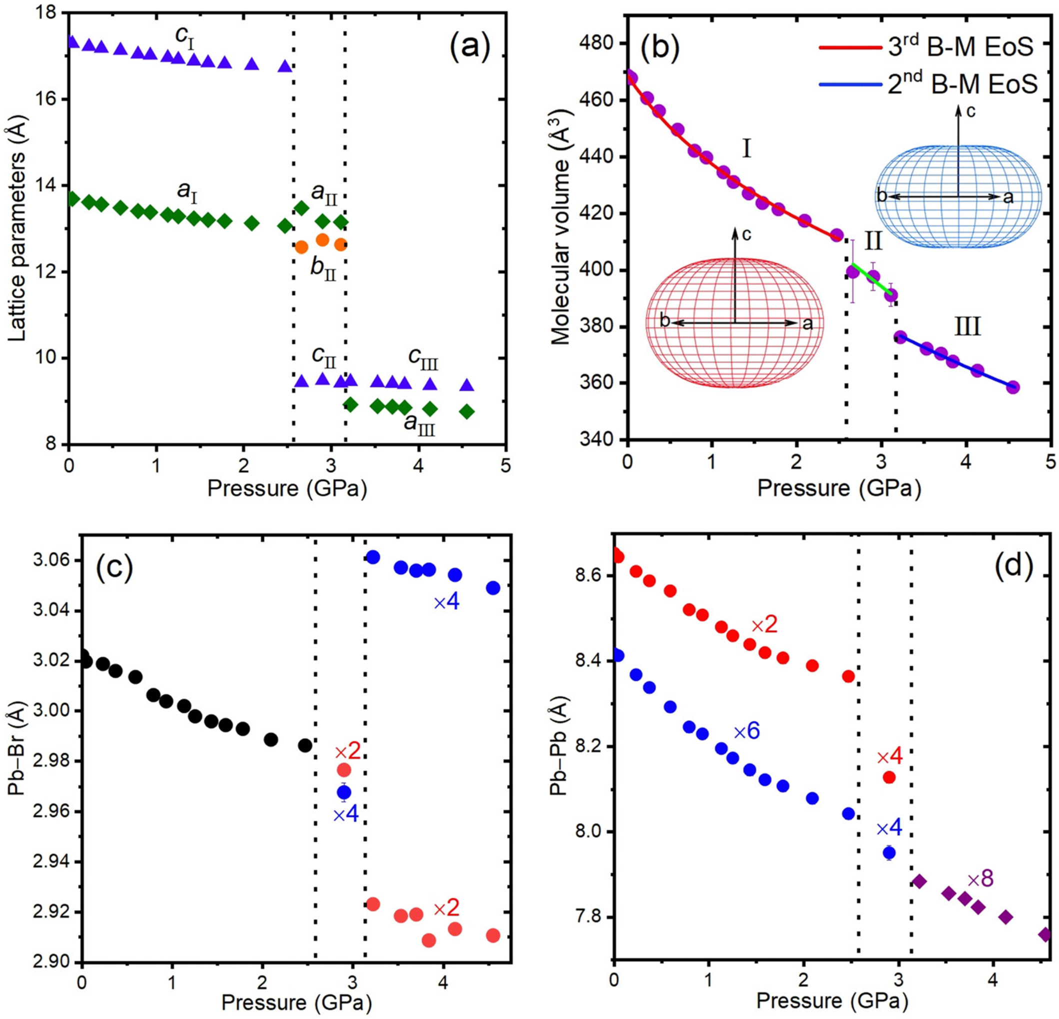

Fig. 2 Pressure dependence of Cs_4PbBr_6 structural parameters: (a) unit cell dimensions, (b) molecular volume, (c) Pb–Br bond lengths, and (d) Pb–Pb distances. The multiplicity of the bonds of the same length is marked. The molecular volume in phases I and III was fitted using the 3rd- and 2nd-order B–M EoS, respectively. The line in phase II serves only as a guide for the eyes. The insets in (b) show the compressibility indicatrices calculated for phases I and III using PASCAL software.[47]

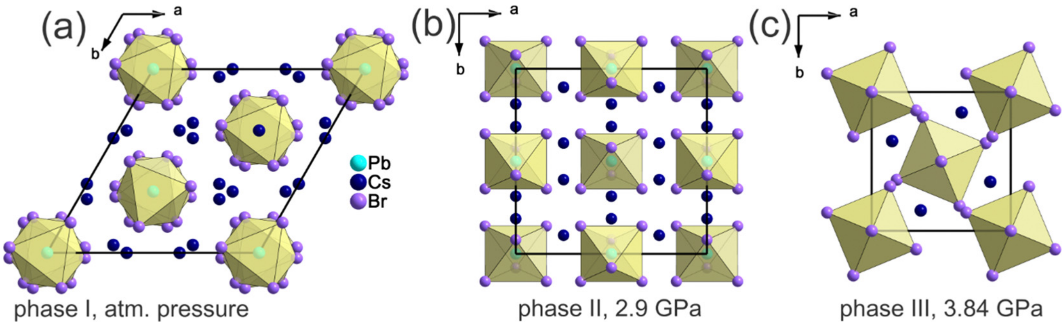

Fig. 3 Projections of the crystal structures of Cs_4PbBr_6 in phase I at atmospheric pressure (a), phase II under pressure of 2.9 GPa (b), and phase III under pressure 3.84 GPa (c).

$CsPbBr_3$ (B_0 = 15.0(8) GPa).[42] The comparison was made by plotting B_0' *versus* B_0 together with their confidence ellipses, as shown in Fig. S2 (ESI†). We also fitted the $V(T)$ data of Cs_4PbBr_6 in phase III using the second-order B–M EoS. The bulk modulus obtained B_0 = 13.1(9) GPa is slightly larger than in phase I. The crystal compressibility in phase I is almost isotropic, only slightly smaller along *c* than in the perpendicular *a-b* plane, but the anisotropy clearly increases in phase III, as illustrated by the compressibility indicatrices plotted in Fig. 2b. At atmospheric pressure in phase I, the $PbBr_6$ octahedra are regular with all Pb–Br bonds length of 3.022(1) Å. Under pressure, the Pb–Br bonds gradually contract up to 2.5 GPa, where the transition to phase II differentiates their lengths (Fig. 2c). In phase II at 2.9 GPa, two longer bonds are of 2.977(2) Å and four shorter of 2.968(4) Å, so the distortion of the octahedra is not very large. The transition to phase III is associated with unprecedented deformation of the octahedra. The four equatorial bonds elongate to 3.061(1) Å that exceeds the length of Pb–Br at ambient pressure, while the two axial bonds contract to 2.923(1) Å. The deformation of the octahedra at the transition to phase III is associated with a large increase in their volume by more than 5% (Fig. 5), which contrasts with the decrease in the volume of the unit cell (Fig. 2b) and with the behaviour of other structural parameters. From the plot in Fig. 2d it is evident that the distances between the octahedra exhibit normal pressure dependence, decreasing at the transitions points as well as across all the phases during compression. Furthermore, the volume of the polyhedron created by the Cs^+ cations surrounding each $PbBr_6$ octahedron, $V_{Cs–Cs}$, also decreases with increasing pressure (Fig. 5). Thus, the unusual distortion of the octahedra can hardly be rationalized by pressure-induced structural changes, which leads to the conclusion that the reason may lie in the intrinsic properties of the octahedra. A possible explanation is an electronically driven geometrical distortion caused by the pressure-induced cooperative Jahn–Teller (JTE) or pseudo Jahn–Teller (PJTE) effect. Considering that the electronic configuration of Pb^{2+} ([Xe]$6s^24f^{14}5d^{10}$) has closed subshells, and therefore its ground state is nondegenerate, the PJTE seems to be the only possible option.[48] The PJTE distortion occurs as a result of the vibronic coupling of the nondegenerate ground and excited states, and there is no limitation in the energy gap between the interacting states. The strong deformation of $PbBr_6$ octahedra is most probably responsible for tetragonal arrangement of the crystal structure, and therefore the symmetry increase in the high-pressure phase III can be attributed to the pressure-induced PJTE.

High-pressure optical measurements of Cs_4PbBr_6

The absorption spectra of pure Cs_4PbBr_6 measured in the pressure range up to 4.2 GPa are shown in Fig. 6a. The absorption edge redshifts under compression, indicating a bandgap narrowing. The sharp and well-separated excitonic band at around 315 nm broadens slightly under compression in phase I and its width suddenly rises at the transition to phase II. This broadening can be ascribed to the differentiation of Pb–Br lengths in the orthorhombic phase II (see Fig. 2c). However, the most spectacular is the band splitting into two components when the crystal transforms to the tetragonal

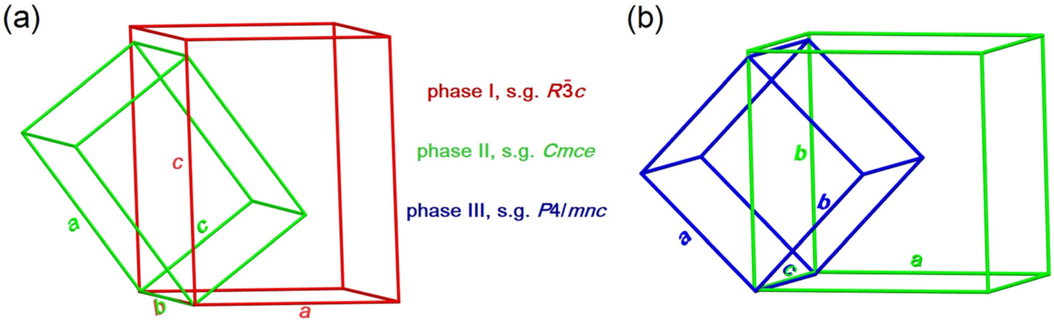

Fig. 4 Relationships between the unit cells of Cs_4PbBr_6 in phases I and II (a) and II and III (b).

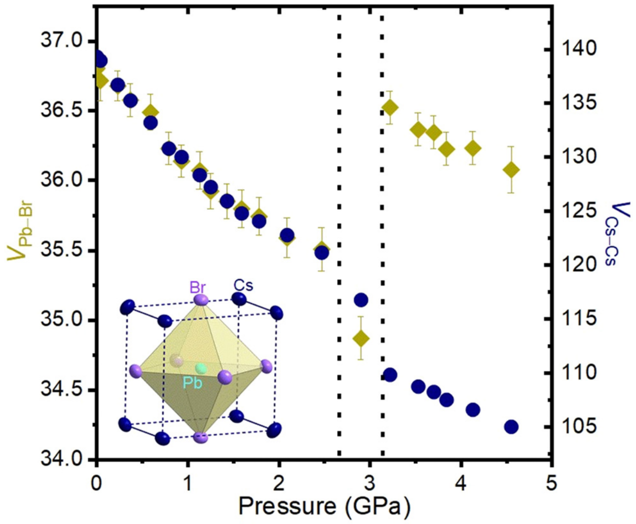

Fig. 5 Pressure-induced changes in the volume of the $PbBr_6$ octahedron and in the polyhedron formed of Cs^+ cations surrounding each octahedron.

phase III. The splitting confirms a huge geometrical distortion of the $PbBr_6$ octahedra, testifying the pressure-induced PJT effect in Cs_4PbBr_6.

For the bandgap determination, the absorption edges measured under pressure were transformed to Tauc plots,[49] as illustrated in Fig. S3 (ESI†). In these graphs, the intersection of a linear part of $(\alpha h\nu)^2$ with the $h\nu$-axis (α is the absorption coefficient of the material) defines the energy gap E_g. The pressure dependence of E_g for pure Cs_4PbBr_6 is shown in Fig. 6b. The two steps at 2.6 and 3.2 GPa correspond to first-order phase transitions observed in the X-ray diffraction study. The narrowing tendency in the bandgap with increasing pressure, observed across the three phases of the crystal, results in a substantial E_g decrease by 0.51 eV at 4.2 GPa.

Atomic coordinates derived from SCXRD high-pressure experiments were used for first-principle calculations to monitor the electronic band structure of Cs_4PbBr_6 under compression. The representative band structures and atom- and orbital-projected densities of states for phases I–III are shown in Fig. 7a–c. The bands are very flat in the trigonal phase I and of only slightly enhanced dispersion in phases II and III. This is because they originate in the isolated $PbBr_6$ octahedra and hence their molecular-like character. In all phases the valence-band maximum (VBM) has a dominant character of Br-4p and Pb-6s orbitals while the conduction band minimum (CBM) is mainly contributed from Pb-6p orbitals. The energy gap of 3.87 eV, calculated using the atomic positions determined for the crystal structure under atmospheric pressure, is in good agreement with previous calculations.[13,50,51] The energy gap has a direct character in phase I and is located at the Γ-point of the Brillouin zone (Fig. 7a), whereas in phases II and III the calculated gap is indirect (Fig. 7b and c). The splitting of the lowest absorption band into two components in phase III at 3.3 GPa (Fig. 6a) was estimated to be of 0.37 eV, which well corresponds to the calculated separation of 0.37 eV between the two lowest valence bands in this phase, as seen in the right panel of Fig. 7c.

The experimental pressure dependence of the bandgap (Fig. 6b) is very well reproduced by the calculations. As shown in Fig. 7d, the redshift trend in the whole pressure range, the

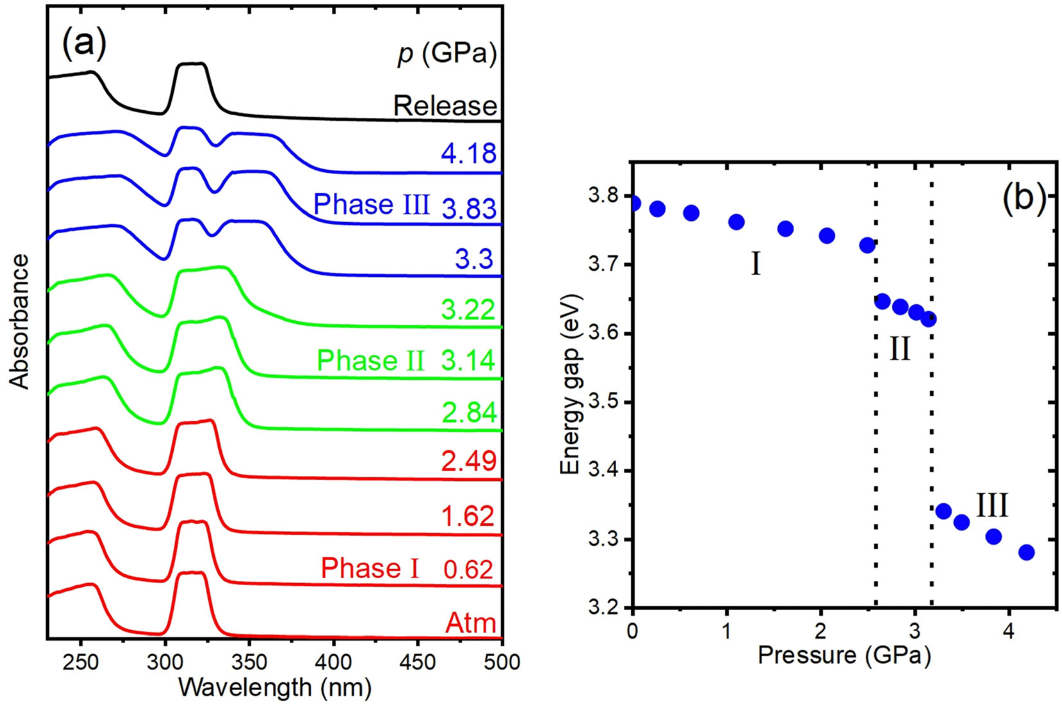

Fig. 6 Selected absorption spectra of the pure Cs_4PbBr_6 single-crystal plate 1.7 μm thick under different pressures in phases I, II, and III (a), and the pressure dependence of the bandgap (b).

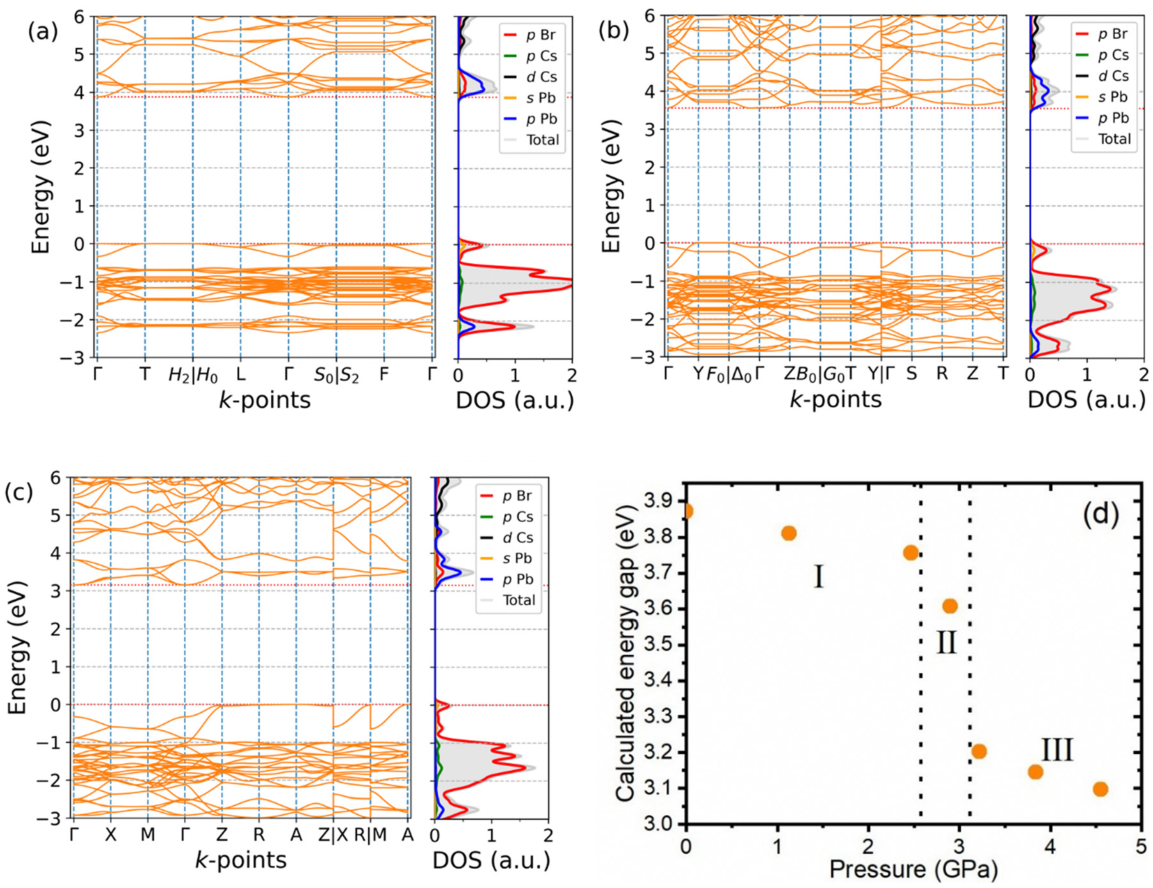

Fig. 7 Electronic band structure (left) of phase I at atmospheric pressure (a), phase II under pressure of 2.9 GPa (b), and phase III under pressure of 3.22 GPa (c), and the pressure dependence of the calculated energy gap (d). On the right panels, total densities of states (grey shadow) and partial densities of states (orbital or atom species projected, as labelled) are presented. The lengths of the specific lines in the *k*-space are shown as equal in the figures and they do not reflect their real lengths.

jumpwise changes at the transition points, and the overall decrease in E_g perfectly match the experiment. This is strongly in contrast to the previously reported results of calculations[22] where the energy gap of Cs_4PbBr_6 at 4 GPa is higher than that at ambient pressure. The reason for such a discrepancy is the improper symmetry ascribed to the high-pressure phase, resulting in the incorrect structural model, which was used for DFT calculations.

The narrowing of the bandgap in the whole studied pressure range is well correlated with the changes in Pb–Br bonds length, which are observed across the three phases of Cs_4PbBr_6 (Fig. 2c). The character of the VBM and CBM implies that the transitions which contribute to the absorption edge are very sensitive to changes in the Pb–Br distances. The shortening of the Pb–Br bonds under compression enhances the overlapping of the Pb-6s and Br-4p orbitals, which increases the VBM and leads to a decrease of E_g.[52] Thus, in phase I the contraction of the regular $PbBr_6$ octahedra leads to monotonic bandgap narrowing. At the transition to phase II, the Pb–Br bonds differentiate into two groups, but the stepwise decrease in E_g is evidently related with the occurrence of shorter bonds. Similarly, the two shortest Pb–Br bonds determine the bandgap in phase III. Their sharp shortening as a result of the PJTE is clearly reflected in a large sudden decrease in E_g at the transition between phases II and III.

Photoluminescence

High-pressure PL experiments were performed for pure Cs_4PbBr_6 using excitation in the spectral range 250–320 nm. At low temperatures, Cs_4PbBr_6 exhibits a weak emission band at 375 nm that is quenched with increasing temperature and therefore not observed under ambient conditions.[53] As expected, we have not detected any PL intensity at atmospheric pressure, but also in the whole pressure range of phases I and II. Our detailed examination shows that a broad emission band extending from 400 to 800 nm and centered at 575 nm appears only after the transition to phase III above 3.2 GPa (Fig. 8). The band is asymmetric with a large Stokes shift, and its intensity increases sharply with increasing pressure in the pressure range studied to 5.4 GPa. The full bandwidth at half maximum (FWHM) exceeds 220 nm at 3.26 GPa and is progressively reduced under compression to *ca.* 180 nm at 5.4 GPa. Although the general character of pressure-induced PL observed in our experiment is similar as in the earlier study,[22] it should be noted that the spectra presented in Fig. 7 exhibit a rich substructure while smooth bands were reported for nanocrystalline Cs_4PbBr_6.

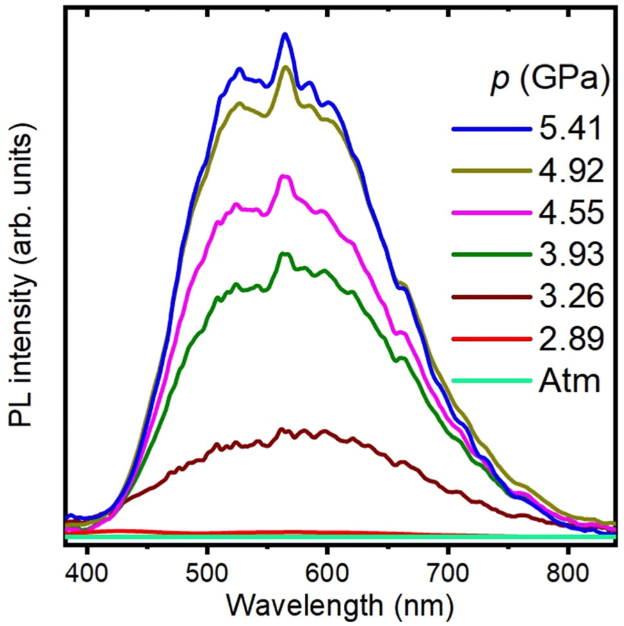

Fig. 8 Pressure evolution of the white-light emission of pure Cs_4PbBr_6.

The white-light emission has been ascribed to the radiative decay of self-trapped excitons (STEs).[22] This mechanism involves transient elastic structural distortion that lower the energy of the excited system.[54] The broadband emission with a large Stokes shift, originating in STEs, was reported for 2D and 1D hybrid perovskites,[54–57] and also for 0D organic–inorganic hybrid materials.[58] Searching for correlations between the broad PL and structural parameters in the layered perovskites, it was found that out-of-plane tilting of the corner-linked metal halide octahedra strongly enhances the emission.[54] This type of lattice deformation is absent in the case of Cs_4PbBr_6, but white PL is evidently triggered by the PJTE distortion of the octahedra.

Conclusions

We have reexamined the 0D perovskite Cs_4PbBr_6 under hydrostatic pressure using SCXRD, optical absorption, and PL experiments. Two pressure-induced first-order phase transitions have been revealed in structural study and confirmed independently by optical measurements. The sequence of structural transitions with disclosed symmetry changes $R\bar{3}c \rightarrow Cmce \rightarrow I4/mnc$ clarifies the pressure response of the crystal structure under genuinely hydrostatic pressure. The proper assignment of the space groups and the refinement of the structures in phases I, II, and III allowed us to obtain precise structural information, which was employed to model the electronic structure of the crystal as a function of pressure using DFT calculations. The calculations perfectly reproduce the experimental pressure dependence of the crystal bandgap, including jumpwise changes at the transition points. The unusual increase in the volume of the $PbBr_6$ octahedra, observed at the transition to the tetragonal phase, pertains to the most intriguing pressure-induced phenomena. This volume increase has been attributed to the PJTE, as a result of which the two vertical Pb–Br bonds contract while the bonds in the equatorial plane are extended. This distortion is responsible for the continuous emission of Cs_4PbBr_6 spanning 400 to 800 nm in high-pressure phase III. Our study demonstrates the importance of proper structural models and accurate structural data for the theoretical analysis of the experimental data and interpretation of materials properties.

Conflicts of interest

There are no conflicts to declare.

Acknowledgements

V. D. and M. S. acknowledge the financial support from the Polish National Science Centre, Grant Opus 16 No. 2018/31/B/ST3/02188. K. J. K. thanks Przemysław Piekarz and Andrzej Ptok for constructive discussions and sincerely acknowledges the hospitality of the Henryk Niewodniczański Institute of Nuclear Physics (of the Polish Academy of Sciences) in Kraków (Poland) as well as access to their computational resources.

References

1 S. D. Stranks and H. J. Snaith, *Nat. Nanotechnol.*, 2015, **10**, 391–402.
2 Z.-K. Tan, R. S. Moghaddam, M. L. Lai, P. Docampo, R. Higler, F. Deschler, M. Price, A. Sadhanala, L. M. Pazos, D. Credgington, F. Hanusch, T. Bein, H. J. Snaith and R. H. Friend, *Nat. Nanotechnol.*, 2014, **9**, 687–692.
3 D. N. Dirin, I. Cherniukh, S. Yakunin, Y. Shynkarenko and M. V. Kovalenko, *Chem. Mater.*, 2016, **28**, 8470–8474.
4 M. M. Lee, J. Teuscher, T. Miyasaka, T. N. Murakami and H. J. Snaith, *Science*, 2012, **338**, 643–647.
5 N. Ali, S. Rauf, W. Kong, S. Ali, X. Wang, A. Khesro, C. P. Yang, B. Zhu and H. Wu, *Renewable Sustainable Energy Rev.*, 2019, **109**, 160–186.
6 J.-C. Hebig, I. Kühn, J. Flohre and T. Kirchartz, *ACS Energy Lett.*, 2016, **1**, 309–314.
7 K.-H. Wang, L. Wu, L. Li, H.-B. Yao, H.-S. Qian and S.-H. Yu, *Angew. Chem.*, 2016, **55**, 8328–8332.
8 Q. A. Akkerman, A. L. Abdelhady and L. Manna, *J. Phys. Chem. Lett.*, 2018, **9**, 2326–2337.
9 B. M. Benin, D. N. Dirin, V. Morad, M. Wörle, S. Yakunin, G. Rainò, O. Nazarenko, M. Fischer, I. Infante and M. V. Kovalenko, *Angew. Chem.*, 2018, **57**, 11329–11333.
10 M. I. Saidaminov, J. Almutlaq, S. Sarmah, I. Dursun, A. A. Zhumekenov, R. Begum, J. Pan, N. Cho, O. F. Mohammed and O. M. Bakr, *ACS Energy Lett.*, 2016, **1**, 840–845.
11 D. Chen, Z. Wan, X. Chen, Y. Yuan and J. Zhong, *J. Mater. Chem. C Mater*, 2016, **4**, 10646–10653.

12 J.-H. Cha, J. H. Han, W. Yin, C. Park, Y. Park, T. K. Ahn, J. H. Cho and D.-Y. Jung, *J. Phys. Chem. Lett.*, 2017, **8**, 565–570.

13 M. De Bastiani, I. Dursun, Y. Zhang, B. A. Alshankiti, X.-H. Miao, J. Yin, E. Yengel, E. Alarousu, B. Turedi, J. M. Almutlaq, M. I. Saidaminov, S. Mitra, I. Gereige, A. AlSaggaf, Y. Zhu, Y. Han, I. S. Roqan, J.-L. Bredas, O. F. Mohammed and O. M. Bakr, *Chem. Mater.*, 2017, **29**, 7108–7113.

14 S. Seth and A. Samanta, *J. Phys. Chem. Lett.*, 2017, **8**, 4461–4467.

15 H. Zhang, Q. Liao, Y. Wu, J. Chen, Q. Gao and H. Fu, *Phys. Chem. Chem. Phys.*, 2017, **19**, 29092–29098.

16 X. Chen, D. Chen, J. Li, G. Fang, H. Sheng and J. Zhong, *Dalton Trans.*, 2018, **47**, 5670–5678.

17 J. Yin, H. Yang, K. Song, A. M. El-Zohry, Y. Han, O. M. Bakr, J.-L. Brédas and O. F. Mohammed, *J. Phys. Chem. Lett.*, 2018, **9**, 5490–5495.

18 X. Sun, Z. Gao, Y. Liu, Z. Wang, X. Wang, W. Zhang, B. Xu and X. Meng, *ACS Photonics*, 2019, **6**, 3290–3297.

19 L. Yang, T. Wang, X. Yang, M. Zhang, C. Pi, J. Yu, D. Zhou, X. Yu, J. Qiu and X. Xu, *Opt. Express*, 2019, **27**, 31207.

20 M. Nikl, E. Mihokova, K. Nitsch, F. Somma, C. Giampaolo, G. P. Pazzi, P. Fabeni and S. Zazubovich, *Chem. Phys. Lett.*, 1999, **306**, 280–284.

21 Z. Qin, S. Dai, V. G. Hadjiev, C. Wang, L. Xie, Y. Ni, C. Wu, G. Yang, S. Chen, L. Deng, Q. Yu, G. Feng, Z. M. Wang and J. Bao, *Chem. Mater.*, 2019, **31**, 9098–9104.

22 Z. Ma, Z. Liu, S. Lu, L. Wang, X. Feng, D. Yang, K. Wang, G. Xiao, L. Zhang, S. A. T. Redfern and B. Zou, *Nat. Commun.*, 2018, **9**, 4506.

23 H. L. Wells, *Z. Anorg. Allg. Chem.*, 1893, **3**, 195–210.

24 Y. Rakita, N. Kedem, S. Gupta, A. Sadhanala, V. Kalchenko, M. L. Böhm, M. Kulbak, R. H. Friend, D. Cahen and G. Hodes, *Cryst. Growth Des.*, 2016, **16**, 5717–5725.

25 L. Merrill and W. A. Bassett, *Rev. Sci. Instrum.*, 1974, **45**, 290–294.

26 G. J. Piermarini, S. Block, J. D. Barnett and R. A. Forman, *J. Appl. Phys.*, 1975, **46**, 2774–2780.

27 A. Katrusiak, *Z. Kristallogr. - Cryst. Mater.*, 2004, **219**, 461–467.

28 CrysAlisPro: *Data Collection and Processing Software for X-Ray Diffractometers*, Santa Clara, Agilent Technologies, Santa Clara, CA, 2010.

29 G. M. Sheldrick, *Acta Crystallogr., Sect. A: Found. Crystallogr.*, 2008, **64**, 112–122.

30 D. Staško, J. Prchal, M. Klicpera, S. Aoki and K. Murata, *High Press. Res.*, 2020, **40**, 525–536.

31 K. Murata and S. Aoki, *Rev. High Press. Sci. Technol.*, 2016, **26**, 3–7.

32 P. E. Blöchl, *Phys. Rev. B: Condens. Matter Mater. Phys.*, 1994, **50**, 17953–17979.

33 J. P. Perdew, K. Burke and M. Ernzerhof, *Phys. Rev. Lett.*, 1996, **77**, 3865–3868.

34 G. Kresse and J. Hafner, *Phys. Rev. B: Condens. Matter Mater. Phys.*, 1994, **49**, 14251–14269.

35 G. Kresse and J. Furthmüller, *Phys. Rev. B: Condens. Matter Mater. Phys.*, 1996, **54**, 11169–11186.

36 G. Kresse and D. Joubert, *Phys. Rev. B: Condens. Matter Mater. Phys.*, 1999, **59**, 1758–1775.

37 H. J. Monkhorst and J. D. Pack, *Phys. Rev. B: Solid State*, 1976, **13**, 5188–5192.

38 Y. Hinuma, G. Pizzi, Y. Kumagai, F. Oba and I. Tanaka, *Comput. Mater. Sci.*, 2017, **128**, 140–184.

39 A. Togo and I. Tanaka, *arXiv*, 2018, arXiv:1808.01590.

40 K. Heidrich, H. Künzel and J. Treusch, *Solid State Commun.*, 1978, **25**, 887–889.

41 H. Ito, H. Onuki and R. Onaka, *J. Phys. Soc. Jpn.*, 1978, **45**, 2043–2044.

42 M. Szafrański, A. Katrusiak and K. Ståhl, *J. Mater. Chem. A*, 2021, **9**, 10769–10779.

43 M. Cola, V. Massarotti, R. Riccardi and C. Sinistri, *Z. Naturforsch., A: Astrophys., Phys. Phys. Chem.*, 1971, **26**, 1328–1332.

44 G. Xiao, Y. Cao, G. Qi, L. Wang, C. Liu, Z. Ma, X. Yang, Y. Sui, W. Zheng and B. Zou, *J. Am. Chem. Soc.*, 2017, **139**, 10087–10094.

45 F. Birch, *Phys. Rev.*, 1947, **71**, 809–824.

46 V. Drushliak and M. Szafrański, *Inorg. Chem.*, 2022, **61**, 14389–14396.

47 M. J. Cliffe and A. L. Goodwin, *J. Appl. Crystallogr.*, 2012, **45**, 1321–1329.

48 I. B. Bersuker, *Chem. Rev.*, 2013, **113**, 1351–1390.

49 J. Tauc, R. Grigorovici and A. Vancu, *Phys. Status Solidi B*, 1966, **15**, 627–637.

50 Q. A. Akkerman, S. Park, E. Radicchi, F. Nunzi, E. Mosconi, F. De Angelis, R. Brescia, P. Rastogi, M. Prato and L. Manna, *Nano Lett.*, 2017, **17**, 1924–1930.

51 Z. Zhang, Y. Zhu, W. Wang, W. Zheng, R. Lin, X. Li, H. Zhang, D. Zhong and F. Huang, *Cryst. Growth Des.*, 2018, **18**, 6393–6398.

52 L. Kong, G. Liu, J. Gong, Q. Hu, R. D. Schaller, P. Dera, D. Zhang, Z. Liu, W. Yang, K. Zhu, Y. Tang, C. Wang, S.-H. Wei, T. Xu and H. Mao, *Proc. Natl. Acad. Sci. U. S. A.*, 2016, **113**, 8910–8915.

53 M. Nikl, E. Mihokova, K. Nitsch, F. Somma, C. Giampaolo, G. P. Pazzi, P. Fabeni and S. Zazubovich, *Chem. Phys. Lett.*, 1999, **306**, 280–284.

54 M. D. Smith and H. I. Karunadasa, *Acc. Chem. Res.*, 2018, **51**, 619–627.

55 E. R. Dohner, E. T. Hoke and H. I. Karunadasa, *J. Am. Chem. Soc.*, 2014, **136**, 1718–1721.

56 L. Mao, Y. Wu, C. C. Stoumpos, M. R. Wasielewski and M. G. Kanatzidis, *J. Am. Chem. Soc.*, 2017, **139**, 5210–5215.

57 Z. Yuan, C. Zhou, Y. Tian, Y. Shu, J. Messier, J. C. Wang, L. J. van de Burgt, K. Kountouriotis, Y. Xin, E. Holt, K. Schanze, R. Clark, T. Siegrist and B. Ma, *Nat. Commun.*, 2017, **8**, 14051.

58 C. Zhou, H. Lin, Y. Tian, Z. Yuan, R. Clark, B. Chen, L. J. van de Burgt, J. C. Wang, Y. Zhou, K. Hanson, Q. J. Meisner, J. Neu, T. Besara, T. Siegrist, E. Lambers, P. Djurovich and B. Ma, *Chem. Sci.*, 2018, **9**, 586–593.

Supplementary Information

White-Light Emission Triggered by Pseudo Jahn-Teller Distortion at the Pressure-Induced Phase Transition in Cs_4PbBr_6

Viktoriia Drushliak, Konrad J. Kapcia and Marek Szafrański*

Faculty of Physics, Adam Mickiewicz University, Uniwersytetu Poznańskiego 2, 61-614 Poznań, Poland

*Corresponding author e-mail: masza@amu.edu.pl

Table S1. Selected crystallographic and refinement data for the structures of Cs_4PbBr_6.

Crystal formula	Cs_4PbBr_6				
Color	colorless				
Pressure (GPa)	0.0001	1.25	2.09	2.9	3.84
Crystal system	Trigonal			Orthorhombic	Tetragonal
Space group	$R\bar{3}c$			*Cmce*	*P*4/*mnc*
Z	6			4	2
Crystal size (mm)	0.2 × 0.2 × 0.2	0.11 × 0.07 × 0.04	0.11 × 0.07 × 0.04	0.11 × 0.07 × 0.04	0.11 × 0.11 × 0.05
a (Å)	13.6949(2)	13.2866(11)	13.1280(13)	13.202(4)	8.8515(12)
b (Å)	13.6949(2)	13.2866(11)	13.1280(13)	12.76(4)	8.8515(12)
c (Å)	17.3030(3)	16.921(2)	16.780(3)	9.4879(18)	9.3867(13)
Volume (Å^3)	2810.43(9)	2587.0(5)	2504.5(6)	1598(5)	735.4(2)
ρ (g cm^{-3})	4.319	4.692	4.846	5.062	5.502
μ (mm^{-1})	29.423	31.965	33.017	34.488	37.479
No. of measured, independent and observed [$I > 2\sigma(I)$] reflections	7629, 897, 836	4172, 407, 309	3984, 393, 299	3064, 294, 156	3014, 272, 211
R_{int}	0.032	0.052	0.066	0.204	0.062
R_1 [$I > 2\sigma(I)$], $R_1(all)$	0.022, 0.024	0.036, 0.060	0.046, 0.069	0.097, 0.159	0.044, 0.060
wR_2 [$I > 2\sigma(I)$], $wR_2(all)$	0.057, 0.058	0.060, 0.069	0.088, 0.099	0.257, 0.306	0.101, 0.109
S	1.104	1.165	1.112	1.090	1.082

Table S2. Comparison of the unit cell parameters of the colourless and yellow Cs_4PbBr_6 at atmospheric pressure.

	Colorless Cs_4PbBr_6	Yellow Cs_4PbBr_6
Crystal system	Trigonal	
Space group	$R\bar{3}c$	
Z	6	
Crystal size (mm)	0.2 × 0.2 × 0.2	0.10 × 0.07 × 0.07
a (Å)	13.6949(2)	13.6776(6)
b (Å)	13.6949(2)	13.6776(6)
c (Å)	17.3030(3)	17.2585(8)
Volume (Å^3)	2810.43(9)	2796.1(3)

The thermal stability of Cs_4PbBr_6 was verified by the thermogravimetric analysis (TGA) method using a TGA Q50 apparatus (TA Instruments) and by differential scanning calorimetry (DSC) with a Q2000 calorimeter (TA Instruments). TGA was performed on powdered crystals heated with a rate of 10 K min^{-1} in a stream of gaseous nitrogen. TGA has shown that Cs_4PbBr_6 is thermally stable up to about 800 K, where the onset of a decay was detected (Fig. S1a). The DSC cooling/heating runs were measured with the same rate of temperature changes in the range 100–500 K. Under ambient pressure, the trigonal phase of the crystal is preserved in a studied temperature range (Fig. S1b).

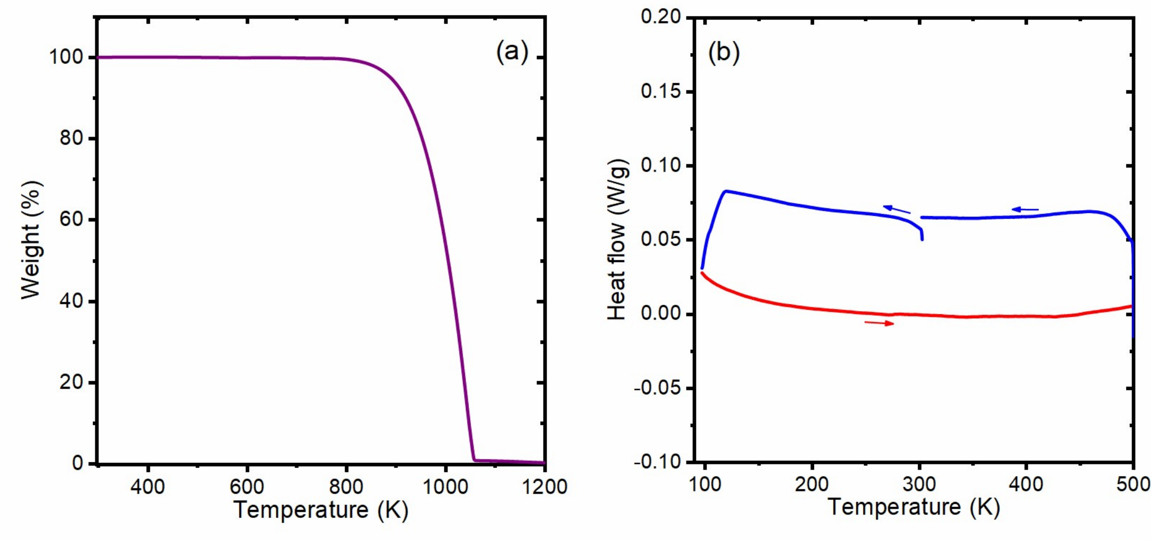

Fig. S1 TGA curve (a), and DSC runs (b) measured for powdered Cs_4PbBr_6 at a temperature rare of 10 K/min.

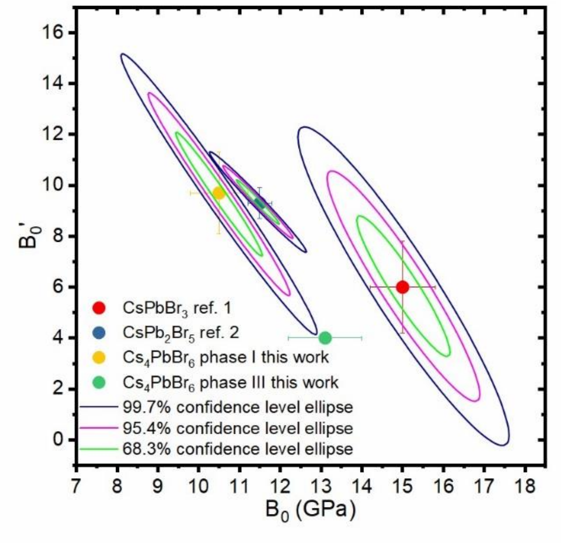

Fig. S2 Values of B_0' plotted versus B_0 for Cs_4PbBr_6, $CsPb_2Br_5$ and $CsPbBr_3$. The different confidence level ellipses are shown. For Cs_4PbBr_6 in phase III the second-order Birch–Murnaghan equation of state was used.

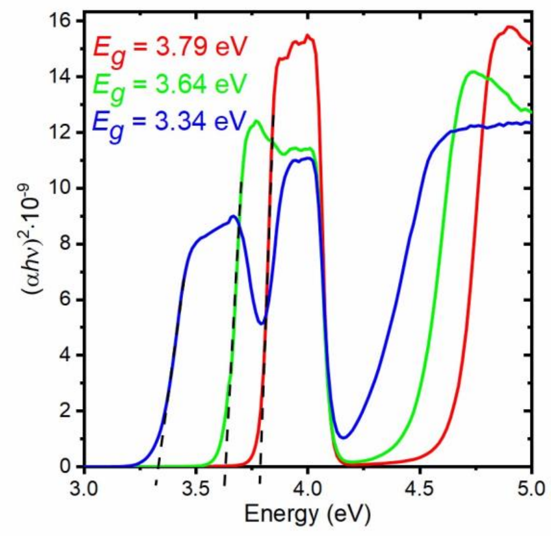

Fig. S3 Tauc plots and energy gaps determined from the absorption spectra measured for the 1.7 μm thick pure Cs_4PbBr_6 single-crystal plate.

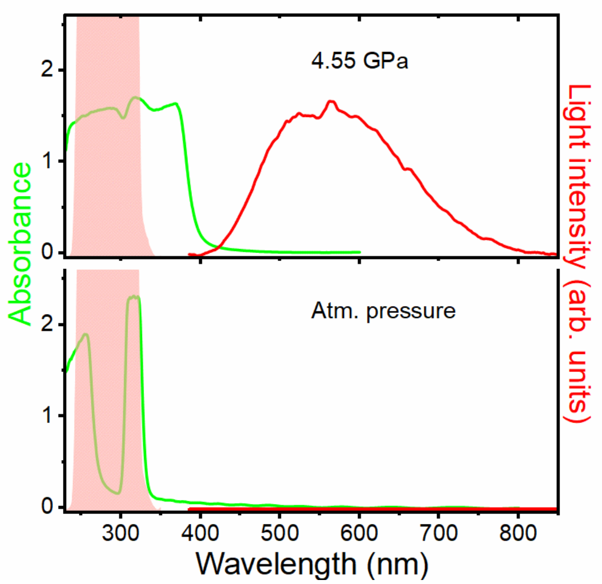

Fig. S4 Comparison of the absorption and emission spectra of pure Cs_4PbBr_6 at atmospheric pressure and 4.55 GPa. Light red colour area represents the excitation spectrum.

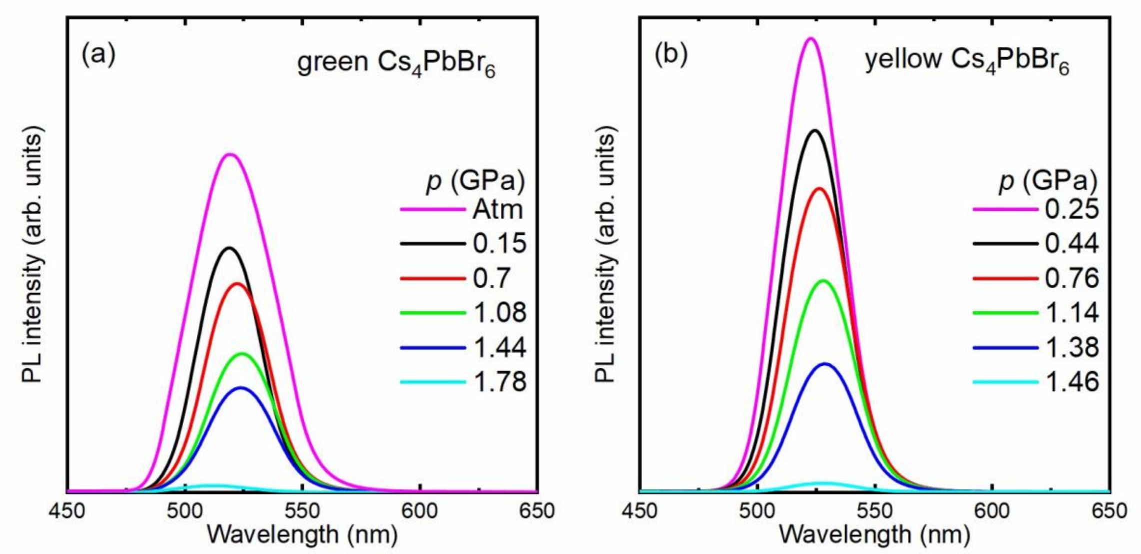

Fig. S5 Pressure dependence of the PL spectra of green (a) and yellow (b) Cs_4PbBr_6.

In Fig. S5, we show the fluorescence spectra of compressed green and yellow Cs_4PbBr_6 samples. With increasing pressure, the PL signal of both forms gradually redshifts and decreases, and finally suddenly disappears around 1.78 and 1.46 GPa, respectively, for the green and yellow crystals. This pressure where PL vanishes corresponds well to the phase transition in $CsPbBr_3$ associated with PL quenching. This indicates that the green emission of Cs_4PbBr_6 originates in $CsPbBr_3$ inclusions.

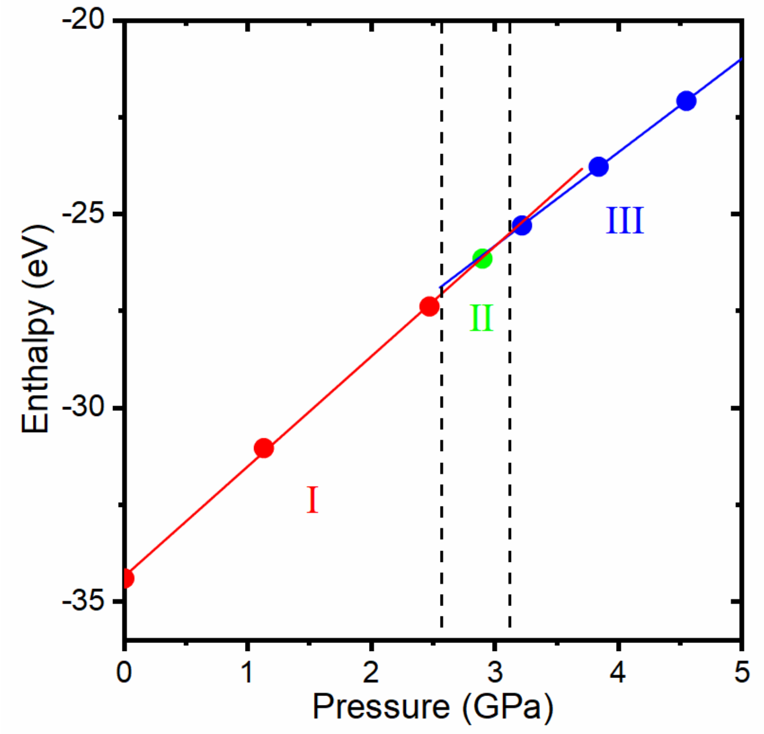

Fig. S6. Free enthalpy calculated for one formula unit as a function of pressure across the phases I, II and III. The solid lines correspond to the best linear fits of the calculated points in phase I (red) and III (blue).

References

1. M. Szafrański, A. Katrusiak and K. Ståhl, *J Mater Chem A Mater*, 2021, **9**, 10769–10779.

2. V. Drushliak and M. Szafrański, *Inorg Chem*, 2022, **61**, 14389–14396.

ChemComm

ROYAL SOCIETY OF CHEMISTRY

COMMUNICATION

View Article Online
View Journal | View Issue

Check for updates

Cite this: *Chem. Commun.*, 2025, **61**, 8019

Received 6th March 2025,
Accepted 22nd April 2025

DOI: 10.1039/d5cc01232e

rsc.li/chemcomm

Effect of pressure and temperature on the structure and optical properties of two-dimensional lead iodide perovskites†

Viktoriia Drushliak and Marek Szafrański *

Hydrostatic pressure and temperature were used to tune the structural and optical properties of layered organic–inorganic perovskites. The narrowing of the band gap in $[C(NH_2)_3]_2PbI_4$ and $CsC(NH_2)_3PbI_4$ has been achieved by both compression and temperature increase. This beneficial modification of the optical properties has been associated with structural changes induced under variable thermodynamic conditions.

Unique properties such as high optical absorption coefficients, adjustable bandgaps, high photoluminescence quantum yields, and long charge carrier lifetimes, combined with low processing costs, have attracted a great deal of attention to hybrid organic–inorganic lead halide perovskites.[1–5] The classical perovskite crystal structure $APbX_3$ (where A is an organic cation and X = Cl, Br, or I) is constructed of PbX_6 corner-sharing octahedra arranged in a three-dimensional (3D) framework, where the voids between the octahedra are occupied by organic cations. However, such 3D structures are formed only for the smallest organic cations $CH_3NH_3^+$, $CH(NH_2)_2^+$ and $CH_3NH_2NH_2^+$,[6–8] while for cations of larger size, crystallisation of perovskites with low-dimensional inorganic frameworks occurs.[9] The latter scenario is realized in the case of the guanidinium cation $C(NH_2)_3^+$ which is only slightly larger than $CH_3NH_3^+$ or $CH(NH_2)_2^+$, but as a more chemically stable unit could be an excellent alternative. Unfortunately, under ambient conditions $C(NH_2)_3PbI_3$ forms a one-dimensional (1D) framework with double chains of PbI_6 octahedra,[10–12] that is characterised by a much wider energy gap compared to its 3D counterparts. Three other lead(II) iodates containing guanidinium cations also crystallise with low-dimensional architectures of inorganic moieties.[9,12,13] In particular, $[C(NH_2)_3]_2PbI_4$ forms a layered structure where the PbI_6 octahedra are arranged into double perovskite layers in which every second octahedron is missing, and the resulting voids are occupied by guanidinium cations. Guanidinium cations also occupy space between the layers,[13] forming barriers for charge carriers (Fig. 1a).

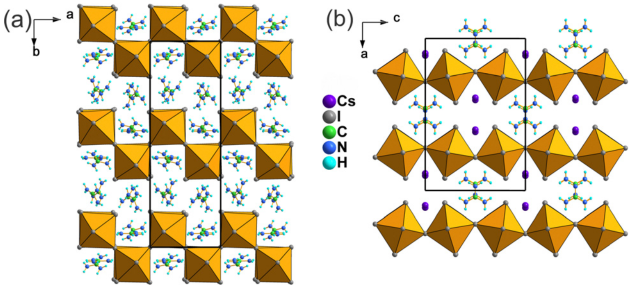

Fig. 1 Room-temperature crystal structures of (a) $[C(NH_2)_3]_2PbI_4$ and (b) $CsC(NH_2)_3PbI_4$.

The 2D perovskites of a general formula A_2PbX_4 are natural strongly confined quantum systems of tunable optoelectronic properties that can be modified primarily by changing the halogen atoms and the thickness of the inorganic layers.[4] Due to the confinement effect, the low-dimensional perovskites have narrower absorption spectra compared to their 3D counterparts, but nevertheless they are promising candidates for applications in tandem solar cells.[14] Electronic and optical properties of these 2D materials can also be modified by introducing mixed cations. In the case of $[C(NH_2)_3]_2PbI_4$ the substitution of Cs^+ in place of one of the two guanidinium cations leads to the formation of $CsC(NH_2)_3PbI_4$,[15] the structure of which contains single layers of corner-sharing PbI_6 octahedra (Fig. 1b). The change in octahedral connectivity affects the overlapping of Pb and I orbitals that results in the absorption edge modification,[9] reflected in the yellow and red colours of $[C(NH_2)_3]_2PbI_4$ and $CsC(NH_2)_3PbI_4$, respectively. The good chemical stability of these materials combined with their moderate bandgaps, narrow-band photoconductive response and luminescence activity, is relevant for photovoltaic and optoelectronic research.[15,16]

In the present work, we discuss the structural and optical properties of $[C(NH_2)_3]_2PbI_4$ and $CsC(NH_2)_3PbI_4$ under various

---

Faculty of Physics and Astronomy, Adam Mickiewicz University, Uniwersytetu Poznańskiego 2, 61-614 Poznań, Poland. E-mail: masza@amu.edu.pl

† Electronic supplementary information (ESI) available. CCDC 2428383–2428400. For ESI and crystallographic data in CIF or other electronic format see DOI: https://doi.org/10.1039/d5cc01232e

thermodynamic conditions. Previous calorimetric, X-ray diffraction (XRD), and dielectric studies have shown that under atmospheric pressure $[C(NH_2)_3]_2PbI_4$ undergoes two successive second-order phase transitions at $T_1 = 356$ K and at $T_2 = 307$ K, with the following sequence of symmetry changes starting from the high-temperature phase: *Pmna* (phase I) – *Pnnm* (phase II) – $P2_1/n$ (phase III).[10,13,16] To track the temperature evolution of the energy gap (E_g), the optical absorbance spectra were measured for a single-crystal plate in the temperature range 88–423 K (Fig. S1a, ESI†). The E_g values, determined using the Tauc method[17] (Fig. S1b, ESI†), are plotted in Fig. 2a. As seen, the $[C(NH_2)_3]_2PbI_4$ bandgap progressively narrows with increasing temperature, and two second-order structural phase transitions only slightly affect this dependence. The previously reported *p*–*T* phase diagram suggests that at room temperature $[C(NH_2)_3]_2PbI_4$ should transform to high-pressure phase IV at around 0.5 GPa. This is consistent with our present single-crystal high-pressure measurements of optical absorption and XRD performed using a diamond anvil cell (DAC) technique. The plot in Fig. 2b shows that the energy gap drops abruptly when the crystal phase III transforms to phase IV. The overall decrease in the energy gap, resulting from the crystal compression to 4.5 GPa, is quite large, about 0.2 eV. The phase transition at 0.5 GPa has a first-order character, which is also testified by the pressure dependence of the unit cell parameters and volume (Fig. 2c and d). Experimental data $V(T)$ were described by the second-order Birch–Murnaghan equation of state (EoS)[18,19] with bulk moduli (B_0) of 9.8(10) and 13.0(7) GPa, respectively, in phases III and IV. This indicates that phase IV is less compressible than phase III. In phase IV the crystal symmetry decreases to the space group $P\bar{1}$. The layered character of the structure is preserved (see Fig. S3, ESI†), but the tilting and antiphase twisting of the octahedra result in halving of the parameter *b* (Fig. 2c). Changes in the inorganic layers affect the shape of the voids and the arrangement of the guanidinium cations. The pressure-induced shortening of Pb–I bonds (Fig. S4, ESI†), mainly responsible for the bandgap narrowing, is accompanied by a reduction of the octahedral distortion (Fig. S5, ESI†). The E_g decrease at the transition point, is caused by the straitening of the Pb–I–Pb angles (Fig. S6, ESI†), which correspond to the PbI_6 octahedra tilts.

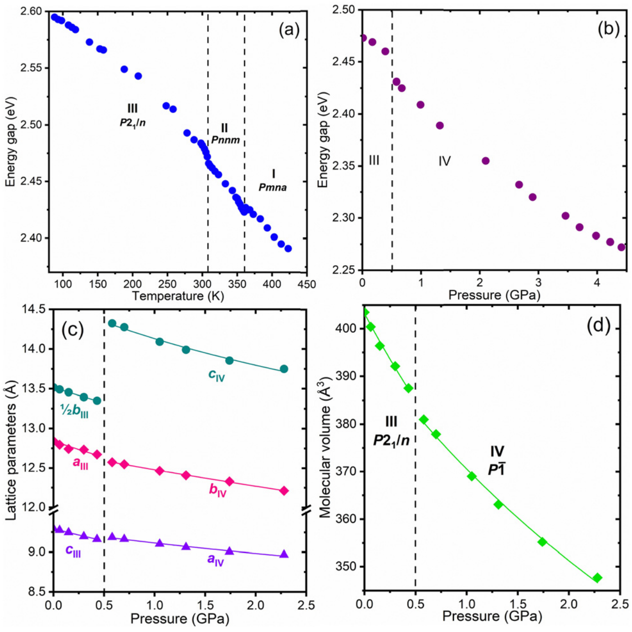

Fig. 2 Energy band gap of $[C(NH_2)_3]_2PbI_4$ measured as a function of temperature (a) and pressure (b), and pressure dependence of unit cell dimensions (c) and molecular volume (d) (α, β and γ angles are shown in Fig. S2, ESI†).

The 2D architecture of $[C(NH_2)_3]_2PbI_4$ suggests a possible anisotropy of compressibility. In fact, the axial coefficients determined for phase III, using the same EoS as for the volume data, $\beta_a = 36.9(21)$ TPa^{-1}, $\beta_b = 31.3(19)$ TPa^{-1} and $\beta_c = 36(4)$ TPa^{-1}, show that, surprisingly, in the direction perpendicular to the layers, the crystal compressibility is smaller than along the *a* and *c* axes, which are parallel to the layers.

Thermogravimetric analysis of the powdered $CsC(NH_2)_3PbI_4$ crystals confirmed thermal stability of this material to approximately 570 K (Fig. S7a, ESI†), while contrary to the previous report[15] our DSC measurements revealed a thermal anomaly that evidences a second-order phase transition at 320.8 K (Fig. 3a). The transition is accompanied by the gain in entropy $\Delta S = 2.66$ J mol^{-1} K^{-1} that was determined by integrating the anomalous part of the temperature dependence of the specific heat, $C_p(T)$ (Fig. S7b, ESI†). A comparison of this value with the relation describing the change in configurational entropy, $\Delta S = R\ln(N_1/N_2)$, shows that the ratio $N_1/N_2 = 1.38$ (*R* is a gas constant and N_1, N_2 are the numbers of configurations in phases I and II, respectively). This can be an indication of the order–disorder contribution to the transition mechanism.

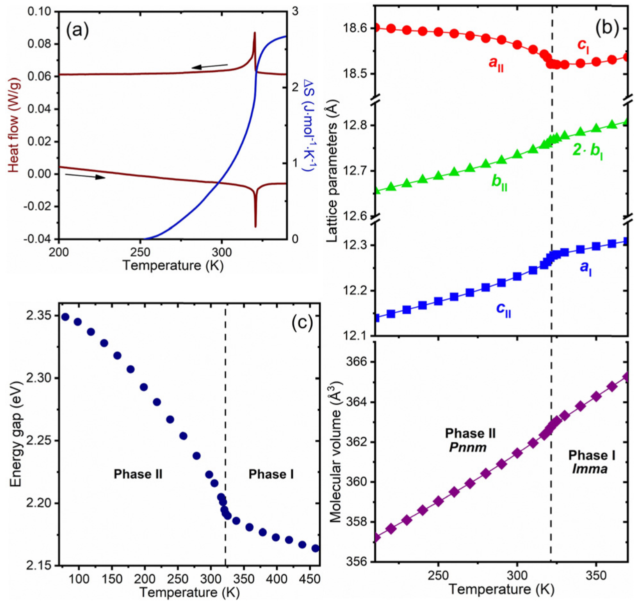

Fig. 3 (a) DSC heating and cooling runs measured for polycrystalline $CsC(NH_2)_3PbI_4$ (brown) and entropy change (blue) in the temperature range 200–380 K. (b) Unit cell dimensions and molecular volume as a function of temperature. (c) Temperature dependence of the energy band gap of $CsC(NH_2)_3PbI_4$.

Temperature-dependent single-crystal XRD measurements were used to study the thermal expansion of the crystal between 200 and 380 K. As shown in Fig. 3b, the lattice parameters and unit-cell volume exhibit anomalies around the transition point at 321 K. These changes are evidently continuous, confirming the second-order character of the transition. In phase II, the parameters *b* and *c* expand with increasing temperature, while *a* clearly shortens. The magnitude of the negative thermal expansion of the crystal along *a* is quite large and increases when approaching the transition point, where α_a takes values of the order -10^{-4} K^{-1} (see Fig. S8, ESI†). The transition to phase I results in a halving of the parameter *b*, and the negative thermal expansion of *a* changes to positive. The jump-wise change in the volume thermal expansion coefficient $\Delta\alpha_V$ = 0.179 10^{-4} K^{-1} and the change in the specific heat ΔC_p = 60 J mol^{-1} K^{-1}, at the transition point, were used to estimate the pressure dependence of the transition temperature. According to the Ehrenfest relation for continuous phase transitions $dT/dp = T_0V_0\Delta\alpha_V/\Delta C_p$ (where V_0 is the crystal volume at the transition temperature T_0), and hence dT_{I-II}/dp = 21 K GPa^{-1}. The positive pressure coefficient indicates a pressure-induced increase in the transition temperature, which precludes the possibility of examining the compressibility of phase I in experiments conducted using DAC at room temperature.

A redetermination of the room temperature crystal structure confirmed the symmetry of the *Pnnm* space group of phase II and its 2D architecture.[15] However, our model differs from that previously reported with respect to structural disorder. Refinement of the structure at 293 K showed that iodine atoms, shared by PbI_6 octahedra along the *c*-axis, exhibit only slightly elongated thermal ellipsoids in the direction perpendicular to the bonds. The splitting of the atomic positions of these iodine atoms did not result in a substantial improvement in the model. It seems that the disorder of these atoms becomes substantial only near the phase transition point. Even then, the occupation of the split sites is significantly different. At 319 K, the occupancy factors were refined to 0.27 and 0.23 for one pair of split iodine sites and 0.45 and 0.05 for the other. In phase II, the corner-linked PbI_6 octahedra are arranged into single layers perpendicular to the *a*-axis (Fig. 1b). The octahedra are slightly distorted and alternately tilted in opposite directions relative to the plane (100) and also to the plane (001), forming smaller and larger cavities occupied by the cations Cs^+ and $C(NH_2)_3^+$, respectively. The Pb–I–Pb angles corresponding to the octahedra tilts, ϕ_1 and ϕ_2, are plotted as a function of temperature in Fig. 4a. In phase II, the bridging angle φ_1 continuously increases with increasing temperature and straightens to 180° at the transition point. The disappearance of the alternating tilts of the PbI_6 octahedra relative to the (001) plane results in a halved parameter *b*, as shown in Fig. 3b (see also Fig. S9, ESI†), and in phase I above 321 K the crystal adopts the symmetry of the space group *Imma*. The refinement of the phase I structure showed that the iodine atoms bridging the octahedra along the *c*-axis occupy split two positions with equal occupancy factors. This picture of the transition mechanism is consistent with the entropy change that also suggests an order–disorder contribution.

The absorbance measurements on a single-crystal plate as a function of temperature were used to determine the temperature dependence of the energy gap of $CsC(NH_2)_3PbI_4$. As shown in Fig. 3c, in phase II the energy gap narrows nonlinearly with increasing temperature up to the phase transition. This change in E_g can be attributed to the straightening of the Pb–I–Pb angles (Fig. 4a), which leads to better overlapping of Pb and I atomic orbitals responsible for the electronic transitions near the absorption edge.[20,21] Above the transition temperature in phase I, the temperature-induced changes are smaller, and the $E_g(T)$ dependence takes a linear form. The clearly continuous changes in E_g confirm the second-order character of the transition.

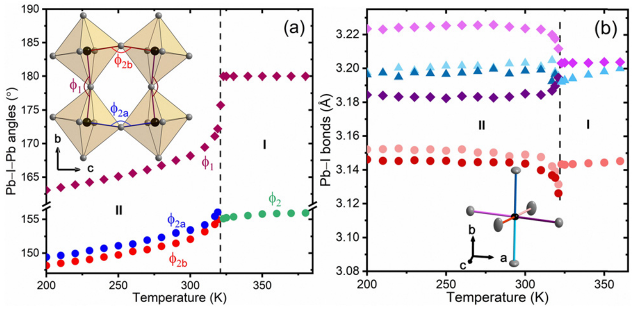

Fig. 4 Temperature dependences of structural parameters of $CsC(NH_2)_3$-PbI_4: (a) the Pb–I–Pb angles, and (c) the Pb–I distances.

The single-crystal XRD high-pressure experiments for $CsC(NH_2)_3$-PbI_4 were performed in the pressure range up to 5.24 GPa. Compression of the crystal results in a gradual contraction of the lattice parameters up to 4.5 GPa, where their jump-wise changes indicate a first-order phase transition (Fig. 5a). The structure of the high-pressure phase III was refined in the space group *Pnnm*, indicating an isostructural character of the transition that is accompanied by a sudden reduction of the octahedra distortion (Fig. S10, ESI†). The 2nd-order Birch–Murnaghan EoS fitted to the experimental $V(p)$ data obtained for phase II gave the bulk modulus B_0 = 15.4(2) GPa, which is substantially higher than the values determined for phases III and IV of $[C(NH_2)_3]_2PbI_4$. This indicates that $CsC(NH_2)_3PbI_4$ is less compressive compared to $[C(NH_2)_3]_2PbI_4$. Furthermore, the axial compressibilities β_a = 15.6(2) TPa^{-1}, β_b = 26.3(3) TPa^{-1} and β_c = 22.9(4) TPa^{-1} indicate a clear anisotropy, but also in this case, similarly as for $[C(NH_2)_3]_2PbI_4$, the direction perpendicular to the inorganic layers is the stiffest. It seems counterintuitive and different compared to other 2D hybrid perovskites where compression is primarily absorbed by organic layers, especially in the low-pressure range.[22,23] Furthermore, the wide range of stability of the ambient pressure phase II distinguishes $CsC(NH_2)_3PbI_4$ from other metal halide perovskites, which typically undergo structural phase transitions under relatively low pressure.

At the transition point, the parameter *a* shortens, while *b* and *c* elongate. These opposing changes compensate for each other, and thus the change in volume at the transition is minor. In phase III, the parameters *a* and *b* contract under increasing pressure, whereas *c* elongates, indicating a negative linear compressibility in this direction. The anomalous compressibility can result from the suppression of vibrations of iodine atoms that bridge the octahedra. Such vibrations perpendicular to the Pb–I bond reduce the average bond length, whereas a decrease in the vibration amplitude translates into bond elongation. This effect, together with the straightening of the Pb–I–Pb angles (Fig. 5b), can result in a negative compressibility along *c*.

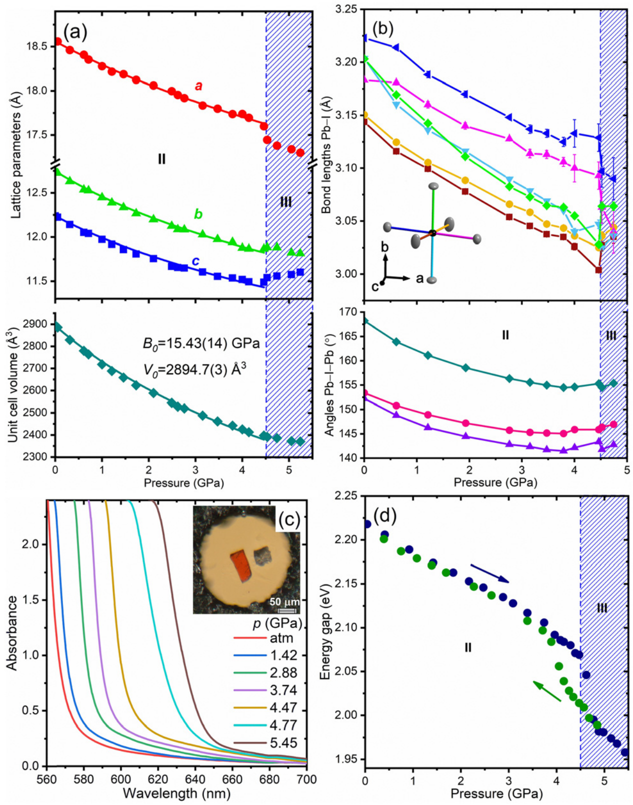

Fig. 5 (a) Pressure dependence of the unit-cell volume and lattice parameters of $CsC(NH_2)_3PbI_4$. (b) Structural parameters, Pb–I distances and Pb–I–Pb angles, plotted as a function of pressure. (c) Selected optical absorption spectra recorded under different pressures; the inset shows the single crystal loaded together with the ruby chip in the DAC. (d) Energy gap determined from absorption spectra, measured while increasing (blue) and decreasing (green) pressure.

The absorption edge of $CsC(NH_2)_3PbI_4$ was measured as a function of pressure up to 5.45 GPa (Fig. 5c). The pressure dependence of E_g (Fig. 5d) shows that the band gap narrows progressively with increasing pressure in phase II, and in phase III this effect is even stronger. The total decrease in E_g by above 12% is reflected in a visible colour change of the crystal (see Fig. S11, ESI†). Substantial pressure hysteresis between the compression and decompression cycles confirms the first-order character of the transition. In lead iodide perovskites, the top of the valence band is dominated by the Pb 6s and I 5p orbitals, while the bottom of the conduction band is primarily composed of the Pb 6p and I 5s orbitals.[20,21] Therefore, the electronic transitions near the absorption edge are very sensitive to changes in the Pb–I bonds and Pb–I–Pb angles. Shortening of the Pb–I bonds improves the overlap of the Pb 6s and I 5p orbitals, leading to a narrowing of the band gap. This effect often competes with the Pb–I–Pb angle bending, associated with the tilts of the PbI_6 octahedra, which weakens the coupling between the Pb and I orbitals and leads to a widening of the band gap. The pressure dependences of the structural parameters shown in Fig. 5b indicate that such competition of pressure effects undoubtedly takes place in phase II of $CsC(NH_2)_3PbI_4$. The band gap narrowing indicates that the contraction of the Pb–I bonds prevails over the bending effect of the Pb–I–Pb angles. The pressure trend to bend the Pb–I–Pb angles is reversed around 4 GPa and their straightening is continued in phase III. This effect is responsible for a much stronger pressure dependence of E_g in phase III.

In summary, our systematic study reveals the response of 2D perovskites $[C(NH_2)_3]_2PbI_4$ and $CsC(NH_2)_3PbI_4$ to hydrostatic pressure and temperature. The increase in temperature results in the decrease in E_g of both materials. This is in contrast to 3D hybrid lead halide perovskites for which an increase in E_g is observed with increasing temperature.[24,25] The beneficial narrowing of the band gap is also achieved by hydrostatic compression. The red shifts of the absorption edges have been correlated with structural changes involving the Pb–I bonds contraction and the rotations of the PbI_6 octahedra.

The authors are grateful for the financial support from the Polish National Science Centre, Grant Opus 16 No. 2018/31/B/ST3/02188.

Data availability

The data supporting this article have been included as part of the ESI,† and crystallographic data in CIF have been deposited with the Cambridge Crystallographic Data Centre, CCDC 2428383–2428400.

Conflicts of interest

There are no conflicts to declare.

Notes and references

1 S. De Wolf, *et al.*, *J. Phys. Chem. Lett.*, 2014, **5**, 1035–1039.
2 J. Berry, *et al.*, *Adv. Mater.*, 2015, **27**, 5102–5112.
3 S. D. Stranks and H. J. Snaith, *Nat. Nanotechnol.*, 2015, **10**, 391–402.
4 B. Saparov and D. B. Mitzi, *Chem. Rev.*, 2016, **116**, 4558–4596.
5 J. S. Manser, J. A. Christians and P. V. Kamat, *Chem. Rev.*, 2016, **116**, 12956–13008.
6 O. J. Weber, B. Charles and M. T. Weller, *J. Mater. Chem. A*, 2016, **4**, 15375–15382.
7 W. Li, *et al.*, *Nat. Rev. Mater.*, 2017, **2**, 16099.
8 M. Mączka, *et al.*, *Chem. Mater.*, 2020, **32**, 1667–1673.
9 Z. Deng, G. Kieslich, P. D. Bristowe, A. K. Cheetham and S. Sun, *APL Mater.*, 2018, **6**, 114202.
10 M. Szafrański, *Thermochim. Acta*, 1997, **307**, 177–183.
11 M. Grottel, M. Szafrański and Z. Pająk, *Z. Naturforsch. A*, 1997, **52**, 783–788.
12 M. Wilke and N. Casati, *Chem. – Eur. J.*, 2018, **24**, 17701–17711.
13 M. Szafrański and A. Katrusiak, *Phys. Rev. B: Condens. Matter Mater. Phys.*, 2000, **61**, 1026–1035.
14 N. N. Lal, *et al.*, *Adv. Energy Mater.*, 2017, **7**, 1602761.
15 O. Nazarenko, *et al.*, *Inorg. Chem.*, 2017, **56**, 11552–11564.
16 M. Daub, C. Haber and H. Hillebrecht, *Eur. J. Inorg. Chem.*, 2017, 1120–1126.
17 J. Tauc, R. Grigorovici and A. Vancu, *Phys. Status Solidi B*, 1966, **15**, 627–637.
18 F. Birch, *Phys. Rev.*, 1947, **71**, 809–824.
19 J. Gonzalez-Platas, M. Alvaro, F. Nestola and R. Angel, *J. Appl. Crystallogr.*, 2016, **49**, 1377–1382.
20 T. Umebayashi, K. Asai, T. Kondo and A. Nakao, *Phys. Rev. B: Condens. Matter Mater. Phys.*, 2003, **67**, 155405.
21 L. Kong, *et al.*, *Proc. Natl. Acad. Sci. U. S. A.*, 2016, **113**, 8910–8915.
22 M. Szafrański, *J. Mater. Chem. A*, 2024, **12**, 2391–2399.
23 L. Zhang, K. Wang and B. Zou, *J. Phys. Chem. Lett.*, 2020, **11**, 4693–4701.
24 M. A. Green, Y. Jiang, A. M. Soufiani and A. Ho-Baille, *Phys. Chem. Lett.*, 2015, **6**, 4774–4785.
25 C. Quarti, *et al.*, *Energy Environ. Sci.*, 2016, **9**, 155–166.

Electronic Supporting Information

Effect of pressure and temperature on the structure and optical properties of two-dimensional lead iodide perovskites

Viktoriia Drushliak[a] and Marek Szafrański*[a]

[a]Faculty of Physics and Astronomy, Adam Mickiewicz University, Uniwersytetu Poznańskiego 2,
61-614 Poznań, Poland

**Corresponding author: Marek Szafrański, e-mail: masza@amu.edu.pl*

Materials and Methods

Chemicals and reagents were purchased and used for syntheses without further purification: guanidinium carbonate (99%, Sigma-Aldrich), caesium carbonate (99%, Sigma-Aldrich), lead(II) iodide (99%, Acros Organics) and hydroiodic acid (57% in water, stabilised with 1.5% hypophosphorous acid, Alfa Aestar). By the reaction of carbonates with hydroiodic acid, caesium iodide and guanidinium iodide were obtained and used as the substrates for further syntheses.

$[C(NH_2)_3]_2PbI_4$ was synthesised in a non-stoichiometric solution containing an excess of $C(NH_2)_3I$. 10 mmol of $C(NH_2)_3I$ was dissolved in hot water (~80°C) acidified with HI, and then the hot solution of 3 mmol of PbI_2 dissolved in 10 ml of HI was added drop by drop with constant stirring. Slow cooling of the solution to room temperature resulted in crystallisation of yellow platelets that were harvested, washed with diethyl ether, and dried. The yield obtained, determined in relation to PbI_2, was approximately 60%.

$CsC(NH_2)_3PbI_4$ was obtained from the hot acid solution using the procedure described by Nazarenko *et al.*[1] 2 mmol of PbI_2, 2 mmol of CsI, and 8 mmol of $C(NH_2)_3I$ were dissolved in 13 ml of HI. The solution was heated and stirred until dissolution of all substrates and then slowly cooled. During several hours of cooling from ~80°C to room temperature, red crystals precipitated. Crystals were harvested, washed with diethyl ether, and dried. The yield of approximately 65% was estimated in relation to PbI_2.

Both materials obtained have been identified by single-crystal X-ray diffraction.

Thermal properties were studied by differential scanning calorimetry (DSC) with the Q2000 calorimeter (TA Instruments), and by thermogravimetric analysis (TGA) using the TGA Q50 instrument (TA Instruments). Both experiments were carried out on powdered samples with a temperature change rate of 10 K min^{-1}.

Single-crystal X-ray diffraction (SCXRD) experiments were performed as a function of temperature and pressure using a four-circle Oxford Diffraction Gemini A Ultra diffractometer operating with graphite-monochromated Mo Kα radiation ($\lambda = 0.71073$ Å). Data were collected and processed using the CrysAlisPro software.[2] Temperature-dependent measurements were carried out in the range from 200 to 380 K. The temperature of the crystals was controlled with an accuracy ± 0.1 K using a Cryostream Plus Cooler (Oxford Cryosystems).

High-pressur experiments were conducted using a modified Merrill-Bassett diamond anvil cell (DAC)[3] equipped with symmetric diamond anvils (culet diameter 0.8 mm) supported on steel discs with conical windows. A steel foil of 250 µm thickness with spark-eroded hole of an approximate diameter of 360 µm was used as a gasket. A selected single crystal with a ruby chip as the pressure calibrant and Daphne oil 7575 as the pressure transmitting medium was loaded into the pressure chamber. The pressure was calibrated before and after each measurement, using the ruby fluorescence method[4] with an accuracy of ± 0.03 GPa. The DAC was centred by the gasket-shadowing method.[5]

Structures were solved and refined using the SHELX and Olex2 software.[6,7] Crystallographic information files (CIFs) for the $[C(NH_2)_3]_2PbI_4$ structures determined under pressure (2428383–2428386) and for the $CsC(NH_2)_3PbI_4$ structures determined at different temperatures and under pressures (2428387–2428400) have been deposited with the Cambridge Crystallographic Data Centre.

Optical absorption spectra were recorded using a Jasco MSV-5100 microscopic spectrophotometer. The absorbance was measured from a small sample area with a diameter of 30 µm at a scan speed of 200 nm min^{-1} and a spectral bandwidth of 5 nm, in the range from 500 to 800 nm. Temperature measurements were made over a range between 79 K and 458 K using a Linkam THMSE600 heating and freezing stage. High-pressure measurements were conducted at room temperature using a DAC equipped with low-fluorescence type IIa diamond anvils. The pressure calibration and hydrostatic liquid were analogous as in the case of the SCXRD experiments.

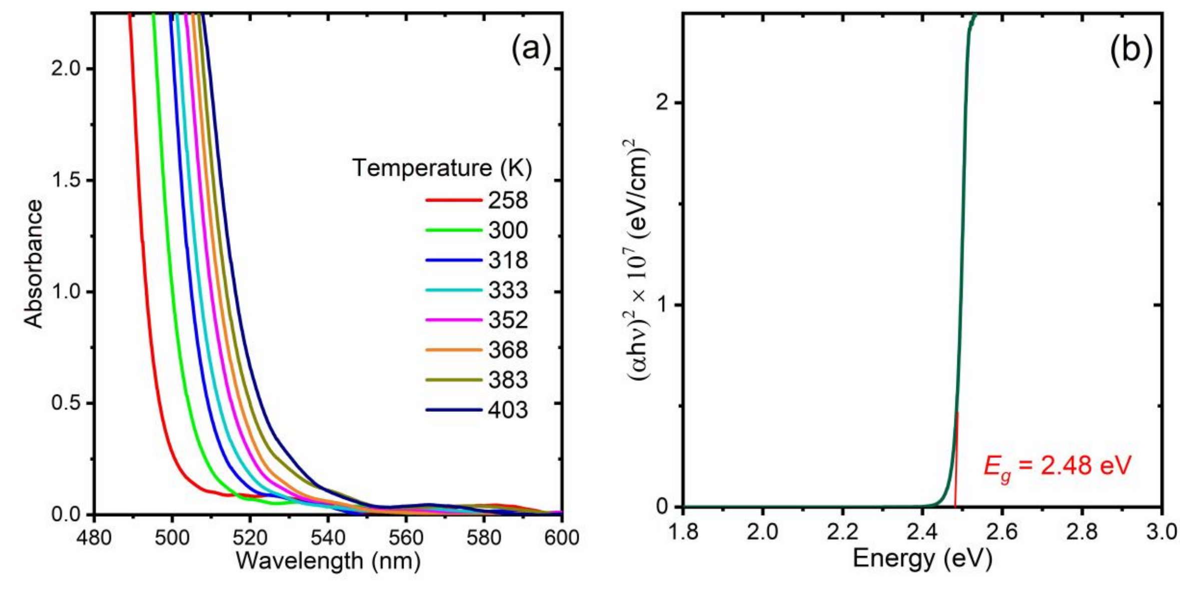

Figure S1 (a) Selected optical absorbance spectra measured for a single-crystal plate of $[C(NH_2)_3]_2PbI_4$ at different temperatures. (b) Tauc plot[8] and energy gap determined from the absorption spectrum measured at 300 K.

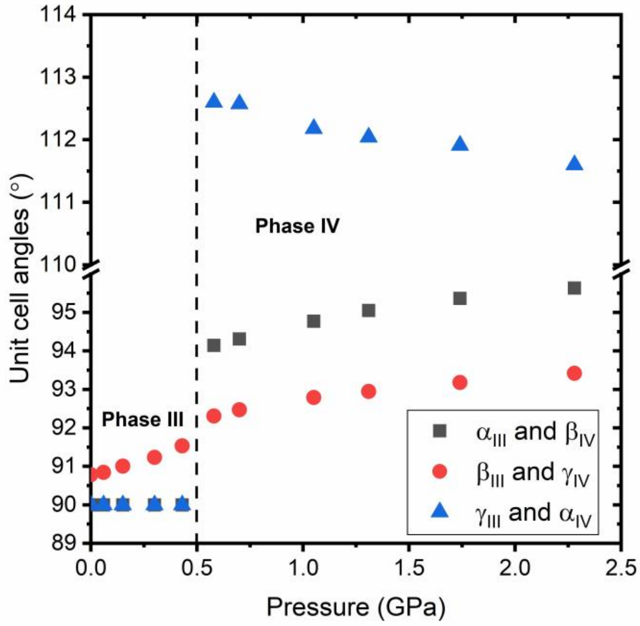

Figure S2 Pressure dependence of the unit-cell angles of $[C(NH_2)_3]_2PbI_4$.

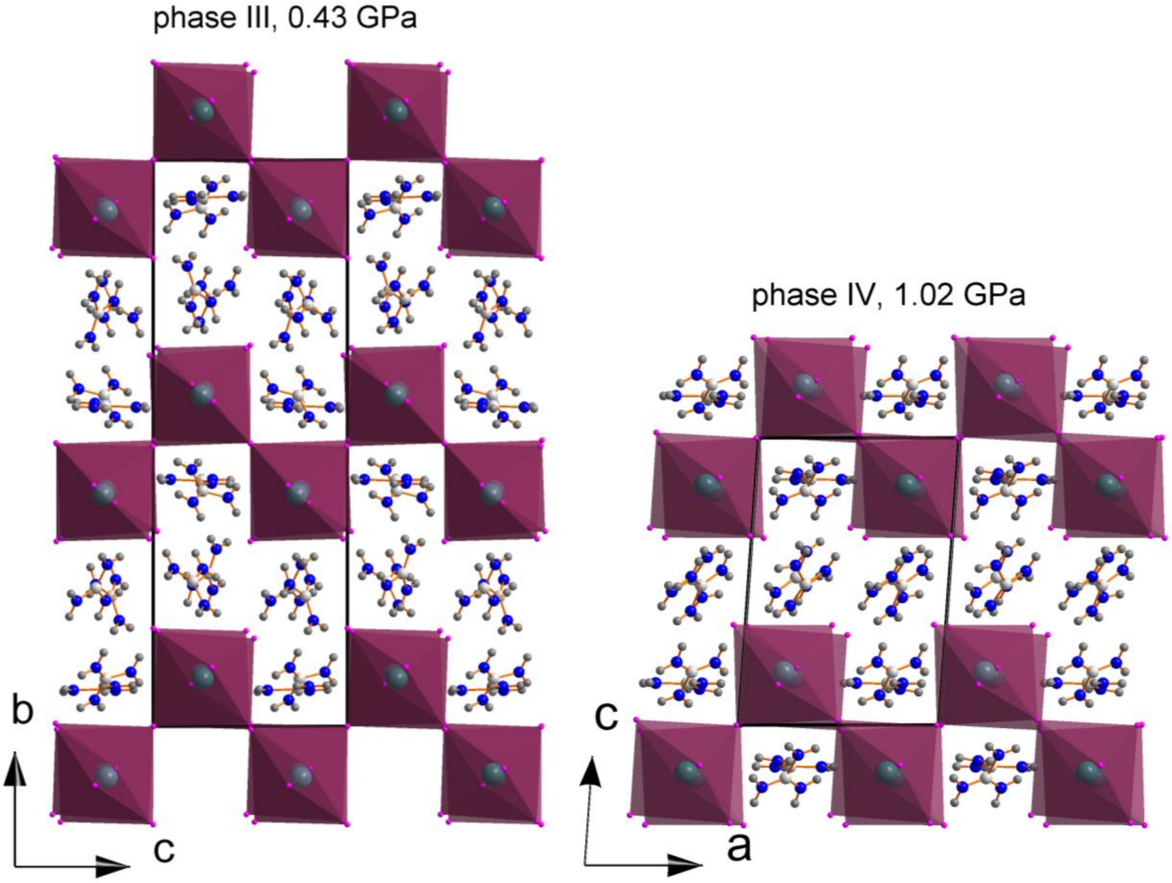

Figure S3 Crystal structure of $[C(NH_2)_3]_2PbI_4$ in phase III at 0.43 GPa and in phase IV at 1.02 GPa.

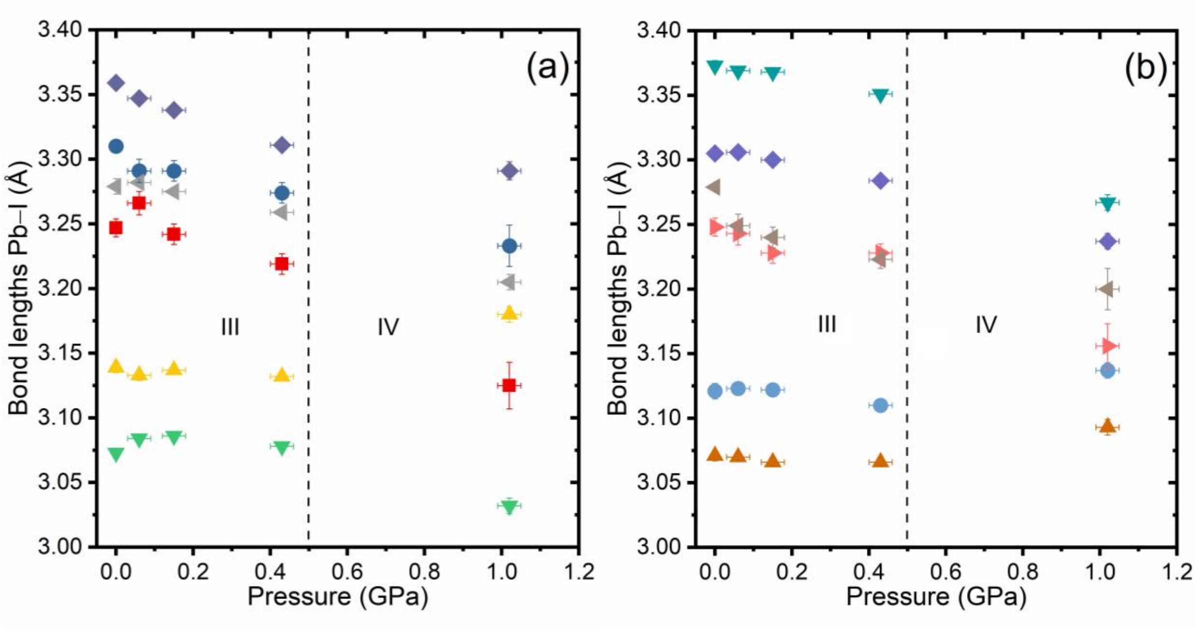

Figure S4 Pressure dependence of the Pb–I bond lengths in the two symmetry-independent PbI_6 octahedra plotted in parts (a) and (b), respectively, in phases III and IV of $[C(NH_2)_3]_2PbI_4$.

Crystal structure description and pressure-induced structural changes in $[C(NH_2)_3]_2PbI_4$

At room temperature $[C(NH_2)_3]_2PbI_4$ crystallises in phase III of the space group $P2_1/n$.[9] The structure is formed of double layers of corner-sharing PbI_6 octahedra, arranged perpendicular to *b* (Fig. S3). In these perovskite layers, every second octahedron is missing, which creates a space for guanidinium cations. Because the size of $C(NH_2)_3^+$ is somewhat incompatible with the size of the perovskite cage the adjacent PbI_6 octahedra are alternately tilted relative to the *a*-axis, to accommodate the cation. Guanidinium cations also occupy space between the layers, forming barriers for charge carriers. The cations in both sites are linked to the inorganic framework through weak N–H···I hydrogen bonds.

Under pressure, phase III of $[C(NH_2)_3]_2PbI_4$ is stable in the pressure range to 0.5 GPa, where the crystal transforms to the triclinic phase IV of the space group $P\overline{1}$. In phase IV the lattice parameter *c*, corresponding to *b* in phase III, is halved, as seen in Fig. 3. The change of symmetry from monoclinic to triclinic defines this transition as ferroelastic, which justifies the appearance of ferroelastic domains. Crystal twinning hindered the XRD experiments, but nonetheless a phase IV structural model was refined from the data collected at 1.02 GPa. In the structure of phases III and IV, there are two symmetry-independent PbI_6 octahedra, both substantially distorted from an ideal octahedral symmetry, as reflected in the Pb–I bond lengths plotted in Fig. S4. With increasing pressure in phase III these bonds progressively contract. To track the distortion of the octahedra as a function of pressure, the octahedral distortion parameter Δd was calculated using the following formula:

$$\Delta d = \frac{1}{6}\sum_{n=1}^{6}\left[\frac{d_n - d}{d}\right]^2,$$

where d is the average Pb–I distance, and d_n are the individual Pb–I distances. The results in Fig. S5 show a substantial reduction in d with increasing pressure, indicating a significant reduction in the distortion of the octahedra. This distortion is further reduced after the transition to phase IV.

Figure S6 shows the pressure dependence of the Pb–I–Pb angles which reflect the PbI_6 octahedra tilts. As seen, these tilts increase in phase III up to the transition point where the substantial changes take place. The straightening of the two smallest Pb–I–Pb angles is responsible for the abrupt narrowing of the energy gap at the transition point at 0.5 GPa.

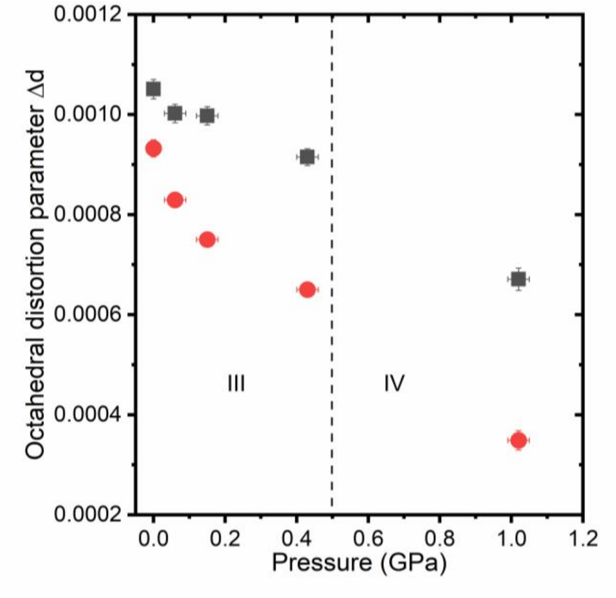

Figure S5 Octahedral distortion parameter Δd plotted as a function of pressure for two symmetry-independent PbI_6 octahedra present in the structure of phases III and IV of $[C(NH_2)_3]_2PbI_4$.

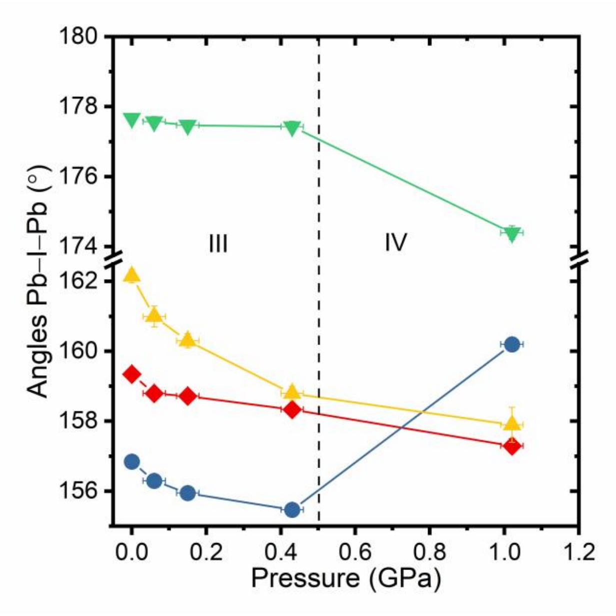

Figure S6 Pb–I–Pb angles plotted in phases III and IV of $[C(NH_2)_3]_2PbI_4$ as a function of pressure.

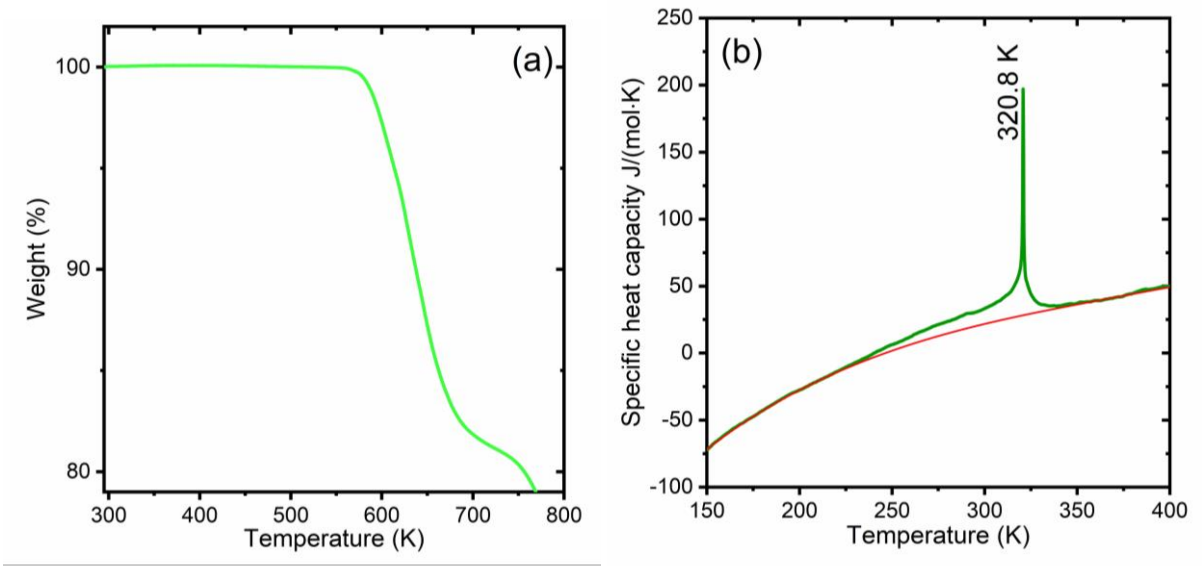

Figure S7 (a) Thermogravimetric analysis of the powdered $CsC(NH_2)_3PbI_4$ crystals and (b) temperature dependence of the specific heat capacity. The red line in (b) marks the baseline used for the entropy change calculation.

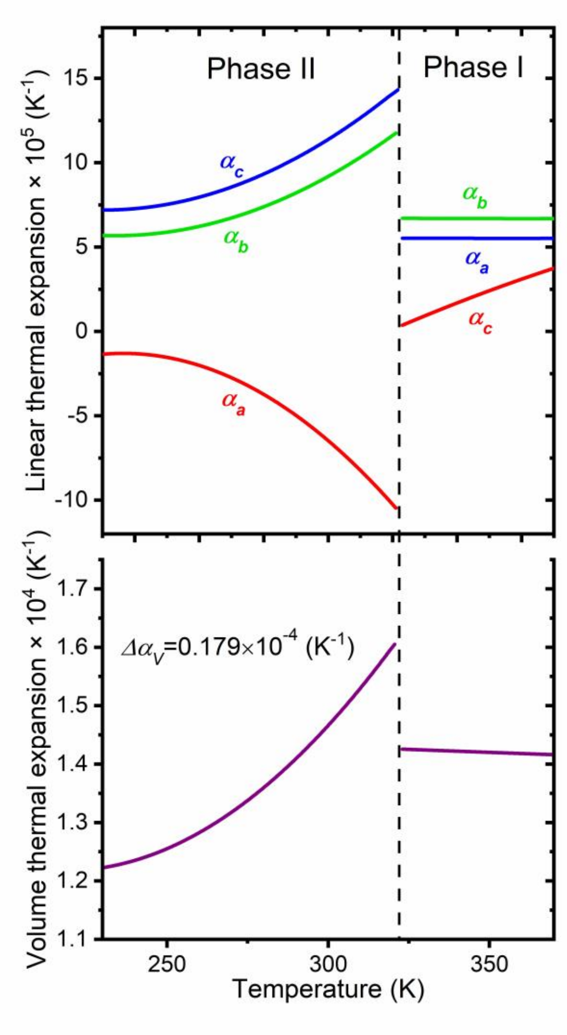

Figure S8 Temperature dependence of the linear and volumetric thermal expansion coefficients of $CsC(NH_2)_3PbI_4$.

Crystal structures in phases I and II of $CsC(NH_2)_3PbI_4$

At room temperature and under atmospheric pressure $CsC(NH_2)_3PbI_4$ crystallises in the space group *Pnnm*.[1] The corner-linked PbI_6 octahedra form single layers perpendicular to the *a*-axis (Fig. S9, left panels). The octahedra are distorted from an ideal octahedral symmetry and alternately tilted in opposite directions relative to the plane (100) and also to the plane (001). Due to the octahedra tilts, two kinds of cavities of different size are formed within the inorganic framework. The small and large cavities are occupied by the cations Cs^+ and $C(NH_2)_3^+$, respectively.

The crystal undergoes a second-order phase transition at 320.8 K to the orthorhombic phase I of the space group *Imma*. As shown in Fig. S9 (right panels) in phase I the iodine atoms, shared by PbI_6 octahedra along the *a*-axis (*a* in phase I corresponds to *c* in phase II), are disordered between two sites. Moreover, the alternating tilts of the PbI_6 octahedra relative to the plane (001) in phase II disappear in phase I, resulting in a halved lattice parameter *b*.

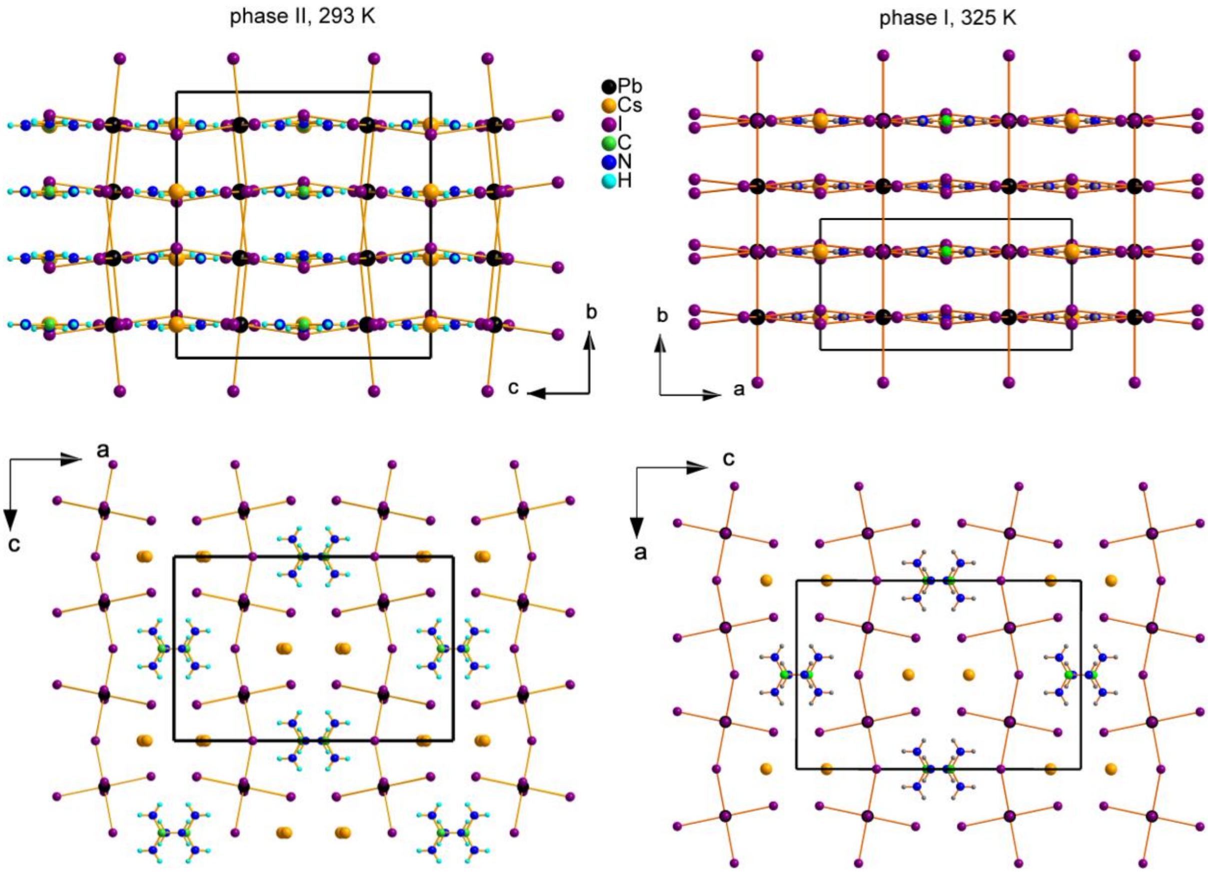

Figure S9 Crystal structures of $CsC(NH_2)_3PbI_4$ in phases II (left) and I (right) viewed along the equivalent directions.

Pressure-induced isostructural phase transition in $CsC(NH_2)_3PbI_4$ at 4.5 GPa

Under pressure at 4.5 GPa, $CsC(NH_2)_3PbI_4$ undergoes a structural phase transition, but in the high-pressure phase III the crystal retains the same symmetry of the space group *Pnnm* as in phase II. The transition is associated with jumpwise changes in the lattice parameters and it also significantly affects the Pb–I bond lengths and Pb–I–Pb angles. The pressure dependence of the octahedral distortion parameter *Δd* is shown in Fig. S10. In phase II, with increasing pressure, the distortion of the PbI_6 octahedron initially changes only slightly but increases significantly as the transition approaches. A jumpwise decrease in *Δd* at the transition point indicates that under pressure in phase III the octahedra become more symmetric.

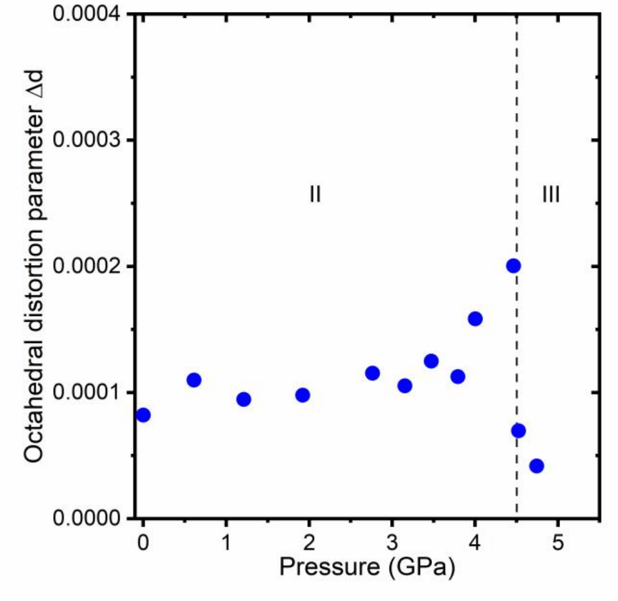

Figure S10 Octahedral distortion parameter Δd derived from the structural models of $CsC(NH_2)_3PbI_4$ obtained at various pressures.

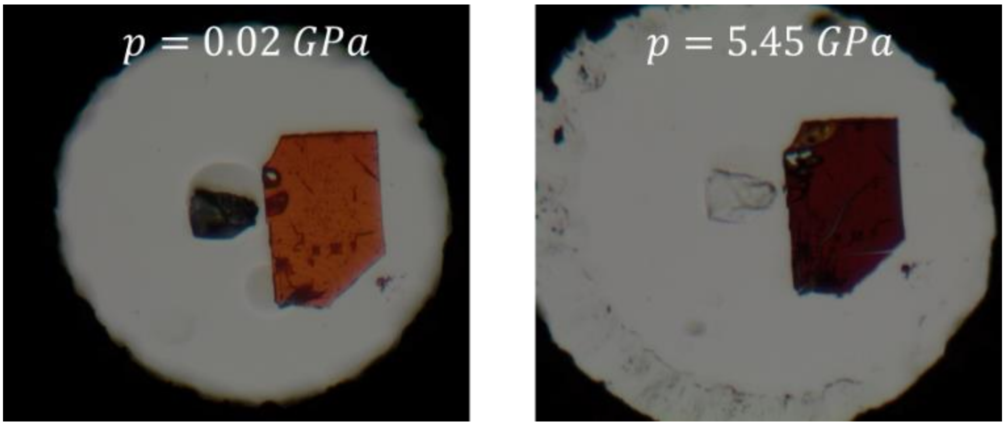

Figure S11 Photos of $CsC[(NH_2)_3]PbI_4$ showing the color change of the crystal under pressure.

Table S1. Selected crystallographic and refinement data for the structures of $[C(NH_2)_3]_2PbI_4$.

Crystal formula	$[C(NH_2)_3]_2PbI_4$		
Color	yellow		
Pressure (GPa)	0.15	0.43	1.02
Crystal system Space group Z	Monoclinic $P2_1/n$ 8		Triclinic $P\overline{1}$ 4
Crystal size (mm)	0.12 × 0.06 × 0.03		
a (Å) *b* (Å) *c* (Å)	12.742(6) 26.9140(17) 9.2472(4)	12.673(4) 26.7036(12) 9.1630(3)	9.1051(7) 12.466(4) 14.0938(16)
α (°) *β (°)* *γ (°)*	90 88.992(11) 90	90 88.468(8) 90	67.82(2) 85.226(7) 87.169(14)
Volume ($Å^3$)	3170.9(14)	3099.7(10)	1475.9(6)
ρ (g cm^{-3})	3.498	3.578	3.758
μ (mm^{-1})	18.410	18.832	19.776
No. of measured, independent and observed [$I > 2\sigma(I)$] refl.	14294, 1864, 1094	13873, 1836, 1137	1668, 1668, 890
R_{int}	0.0927	0.0821	0.0945
R_1 [$I > 2\sigma(I)$], $R_1(all)$	0.061, 0.131	0.057, 0.124	0.062, 0.127
wR_2 [$I > 2\sigma(I)$], $wR_2(all)$	0.111, 0.132	0.115, 0.143	0.159, 0.175
GOF	1.099	1.086	1.097

Table S2. Selected crystallographic and refinement data for the structures of $CsC(NH_2)_3PbI_4$.

Crystal formula	$CsC(NH_2)_3PbI_4$		
Color	red		
Pressure (GPa)	0.0001	2.76	4.52
Crystal system	Orthorhombic		
Space group	$Pnnm$		
Z	8		
Crystal size (mm)	0.18 × 0.05 × 0.02	0.18 × 0.14 × 0.04	
a (Å)	18.5595(4)	17.914(8)	17.475(19)
b (Å)	12.7464(3)	12.0823(4)	11.8768(5)
c (Å)	12.2365(3)	11.6499(4)	11.5309(4)
Volume (Å^3)	2894.76(12)	2521.5(11)	2393(3)
ρ (g cm^{-3})	4.166	4.783	5.039
μ (mm^{-1})	22.627	25.976	27.369
No. of measured, independent and observed [$I > 2\sigma(I)$] reflections	15731, 3543, 2039	10382, 971, 613	9315, 613, 406
R_{int}	0.0489	0.0681	0.0899
R_1 [$I > 2\sigma(I)$], $R_1(all)$	0.046, 0.083	0.04, 0.07	0.077, 0.106
wR_2 [$I > 2\sigma(I)$], $wR_2(all)$	0.121, 0.156	0.099, 0.116	0.178, 0.197
GOF	1.105	1.194	1.056

References

1 O. Nazarenko, M. R. Kotyrba, M. Wörle, E. Cuervo-Reyes, S. Yakunin, M. Kovalenko, *Inorg. Chem*. 2017, **56**, 11552–11564.

2 Agilent Technologies. CrysAlisPro: Data Collection and Processing Software for X-Ray Diffractometers, Santa Clara, CA, 2010.

3 L. Merrill and W. A. Bassett, *Rev. Sci. Instrum*., 1974, **45**, 290–294.

4 R. A. Forman, G. J. Piermarini, J. D. Barnett and S. Block, *Science* 1972, **176**, 284–285.

5 A. Katrusiak, *Z. Kristallogr. Cryst. Mater*., 2004, **219**, 461–467.

6 Sheldrick G.M., *Acta Crystallogr. A*, 2008, *64*, 112–122.

7 O. V. Dolomanov, L. J. Bourhis, R. J. Gildea, J. A. K. Howard and H. Puschmann, J. *Appl. Crystallogr.*, 2009, **42**, 339–341.

8 J. Tauc, R. Grigorovici and A. Vancu, *Phys. Status Solidi B*, 1966, **15**, 627–637.

9 M. Szafrański and A. Katrusiak, *Phys. Rev. B*, 2000, **61**, 1026–1035.

Opis rozprawy doktorskiej:

Imię i nazwisko autora pracy	Viktoriia Drushliak
Adres e-mail, telefon autora pracy	vikdru@amu.edu.pl / vika.drushliak@gmail.com +16729996897
Imię i nazwisko promotora lub promotorów pracy	prof. dr hab. Marek Szafrański
Wydział	Fizyki i Astronomii
Instytut/Zakład	Fizyki/ Zakład Fizyki Doświadczalnej Fazy Skondensowanej
Tytuł pracy w jęz. polskim	Badania strukturalne i optyczne niskowymiarowych materiałów perowskitowych pod wysokim ciśnieniem
Tytuł pracy w jęz. angielskim	Structural and optical studies of low-dimensional perovskite materials under high pressure
Język pracy	angielski
Słowa kluczowe w jęz. polskim (max 5)	Perowskity niskowymiarowe, CsPb2Br5, Cs4PbBr6, [C(NH2)3]2PbI4, CsC(NH2)3PbI4
Słowa kluczowe w jęz. angielskim (max 5)	Low-dimensional perovskites, CsPb2Br5, Cs4PbBr6, [C(NH2)3]2PbI4, CsC(NH2)3PbI4
Streszczenie pracy w jęz. polskim (max 1400 znaków)	Badania wysokociśnieniowe pozwalają zmieniać oddziaływania międzyatomowe bez modyfikacji chemicznej. Niniejsza rozprawa podsumowuje trzy publikacje dotyczące strukturalnych i optycznych reakcji czterech niskowymiarowych materiałów (CsPb2Br5, Cs4PbBr6, [C(NH2)3]2PbI4, CsC(NH2)3PbI4) na zmienne ciśnienie i temperaturę. Ciśnienie i temperatura wywołują deformacje oktaedrów, przejścia fazowe i modyfikacje pasm, często zawężając przerwę energetyczną i aktywując emisję fotoluminescencyjną. CsPb2Br5 zachowuje warstwową strukturę do ≥6 GPa; krawędź absorpcji (~350 nm) przesuwa się ku dłuższym falom, a widoczna PL pochodzi z domieszek CsPbBr3. Cs4PbBr6 przechodzi dwa pierwszorzędowe przejścia przy 2,6 i 3,2 GPa prowadzące do skokowego zmniejszenia przerwy; pseudo-Jahn–Teller powoduje ekspansję oktaedrów i szerokopasmową emisję białego światła. W guanidyniowych 2D perowskitach kompresja i ogrzewanie zawężają gap przez skracanie wiązań Pb–I i prostowanie kątów; obserwowano silną anizotropię

	mechaniczną oraz ujemną kompresję liniową w fazie wysokociśnieniowej CsC(NH2)3PbI4.
Streszczenie pracy w jęz. angielskim (max 1400 znaków)	High-pressure studies probe structure–property links in perovskites by tuning interatomic interactions. This thesis summarizes three papers on the structural and optical responses of four low-dimensional materials—2D $CsPb_2Br_5$, 0D Cs_4PbBr_6, and guanidinium 2D iodides $[C(NH_2)_3]_2PbI_4$ and $CsC(NH_2)_3PbI_4$—under variable pressure and temperature. External stimuli induce octahedral distortions, phase transitions and band-structure changes that often narrow band gaps and can activate or enhance photoluminescence. $CsPb_2Br_5$ retains its layered framework to ≥6 GPa; its UV absorption edge (~350 nm) red-shifts with pressure, and reported visible PL/absorption were traced to 3D $CsPbBr_3$ impurities. Cs_4PbBr_6 exhibits two first-order transitions at 2.6 and 3.2 GPa causing jumpwise band-gap reductions; a pseudo-Jahn–Teller distortion expands $PbBr_6$ octahedra in the tetragonal phase, producing broad white-light emission. In the guanidinium 2D iodides, compression and heating narrow the gap via Pb–I bond contraction and angle straightening; they show highly anisotropic mechanics, and $CsC(NH_2)_3PbI_4$ displays negative linear compressibility in a high-pressure phase linked to suppressed iodine vibrations.
liczba stron	103

Viktoriia Drushliak

Streszczenie

Halogenkowe perowskity metaliczne w ostatniej dekadzie uległy szybkiemu rozwojowi, a ich zróżnicowane składy, wymiarowość i morfologie umożliwiły zastosowania w wysokowydajnych urządzeniach fotowoltaicznych i optoelektronicznych. Pomimo tego postępu nadal istnieją wyzwania związane z ich stabilnością oraz dokładnym zrozumieniem zależności pomiędzy strukturą a właściwościami. Badania wysokociśnieniowe, wykorzystujące techniki takie jak komórki diamentowe (DAC) w połączeniu z dyfrakcją rentgenowską na pojedynczych kryształach (SCXRD) oraz uzupełniającymi metodami optycznymi, stanowią potężne narzędzie do badania tych zależności poprzez zmianę oddziaływań międzyatomowych bez modyfikacji chemicznej.

Niniejsza rozprawa koncentruje się na kluczowych wynikach trzech publikacji, w szczególności na strukturalnych i optycznych odpowiedziach wybranych niskowymiarowych perowskitów pod zmiennym ciśnieniem i temperaturą. Czynniki zewnętrzne, takie jak ciśnienie i temperatura, wywołują deformacje oktaedrów, przejścia fazowe oraz modyfikacje struktury pasm elektronowych, a tym samym bezpośrednio wpływają na zachowanie optyczne. Ciśnienie może nawet aktywować lub wzmacniać fotoluminescencję w materiałach, które w warunkach otoczenia wykazują słabą emisję. Zbadano cztery materiały: dwuwymiarowy (2D) perowskitopodobny $CsPb_2Br_5$, zerowymiarowy (0D) Cs_4PbBr_6 oraz 2D warstwowe perowskity guanidyniowe $[C(NH_2)_3]_2PbI_4$ i $CsC(NH_2)_3PbI_4$.

W przypadku $CsPb_2Br_5$ wykazano, że warstwowy szkielet pozostaje stabilny co najmniej do 6 GPa. Jego krawędź absorpcji w ultrafiolecie, zlokalizowana przy około 350 nm, ulega ciągłemu przesunięciu w stronę dłuższych fal wraz ze wzrostem ciśnienia, co odpowiada zwężaniu przerwy energetycznej. Praca ta wykazała również, że wcześniej raportowana fotoluminescencja i absorpcja w zakresie widzialnym nie są właściwościami intrinsicznymi czystego materiału, lecz pochodzą z obecności domieszek trójwymiarowego $CsPbBr_3$, co podkreśla kluczowe znaczenie czystości próbki. W badaniu nad Cs_4PbBr_6 ujawniono sekwencję dwóch pierwszorzędowych przejść fazowych indukowanych ciśnieniem przy 2.6 i 3.2 GPa. Przejściom tym towarzyszy skokowe zmniejszenie przerwy energetycznej. Unikalne zniekształcenie typu pseudo-Jahna–Tellera prowadzi do anormalnej ekspansji oktaedrów $PbBr_6$ w fazie tetragonalnej, co bezpośrednio odpowiada za ciśnieniowo indukowaną szerokopasmową emisję białego światła. W perowskitach guanidyniowych 2D zarówno kompresja, jak i ogrzewanie powodują zawężenie przerwy energetycznej, wynikające ze skracania wiązań Pb–I oraz prostowania kątów Pb–I–Pb. Zaobserwowano wysoce anizotropową odpowiedź mechaniczną, przy czym kierunek prostopadły do warstw nieorganicznych jest zaskakująco sztywniejszy niż kierunki w płaszczyźnie. Ponadto w fazie wysokociśnieniowej $CsC(NH_2)_3PbI_4$ zidentyfikowano rzadkie zjawisko ujemnej kompresji liniowej wzdłuż jednej osi, przypisane tłumieniu drgań atomów jodu.

Summary

Metal halide perovskites have rapidly advanced over the past decade, with diverse compositions, dimensionalities, and morphologies enabling high-performance photovoltaic and optoelectronic applications. Despite the progress, challenges concerning their stability and the precise understanding of structure–property relationships persist. High-pressure research, using techniques such as diamond anvil cells (DACs) combined with single-crystal X-ray diffraction (SCXRD) and complementary optical methods, provides a powerful means to investigate these relationships by changing interatomic interactions without chemical modification.

This thesis focuses on core findings from three publications, in particular, on the structural and optical responses of selected low-dimensional perovskites under variable pressure and temperature conditions. External stimuli such as pressure and temperature induce octahedral distortions, phase transitions, and electronic band structure modifications, thereby directly influencing optical behaviour. Pressure can even activate or enhance photoluminescence in materials that are weakly emissive under ambient conditions. Four materials were examined: two-dimensional (2D) perovskite-like $CsPb_2Br_5$, zero-dimensional (0D) Cs_4PbBr_6, and 2D layered guanidinium lead iodides, $[C(NH_2)_3]_2PbI_4$ and $CsC(NH_2)_3PbI_4$.

For $CsPb_2Br_5$, the layered framework remains stable up to at least 6 GPa. Its ultraviolet absorption edge at approximately 350 nm continuously red-shifts with increasing pressure, which corresponds to a narrowing of the band gap. This work also clarifies that previously reported visible-range photoluminescence and absorption are not intrinsic properties of the pure material but rather originate from the presence of three-dimensional (3D) $CsPbBr_3$ impurities, underscoring the critical importance of sample purity. In the study on Cs_4PbBr_6, a sequence of two first-order pressure-induced phase transitions at 2.6 and 3.2 GPa was revealed. These phase transitions drive a jumpwise band-gap reduction. A unique pseudo-Jahn–Teller distortion leads to an anomalous expansion of $PbBr_6$ octahedra in the tetragonal phase, directly responsible for pressure-induced broad band white-light emission. In guanidinium-based 2D perovskites, both compression and heating narrow the bandgap, through Pb–I bond contraction and Pb–I–Pb angle straightening. A highly anisotropic mechanical response is observed, with the direction perpendicular to the inorganic layers being surprisingly stiffer than the in-plane directions. Furthermore, a rare phenomenon of negative linear compressibility along one axis is identified in the high-pressure phase of $CsC(NH_2)_3PbI_4$, attributed to the suppression of iodine atom vibrations.